Charles University in Prague
Faculty of Mathematics and Physics

DOCTORAL THESIS

Milan Klicpera

Electron properties of the substituted cerium compounds

Department of Condensed Matter Physics

Supervisor of the doctoral thesis:	Pavel Javorský
Study programme:	Physics
Specialization:	F3

Prague 2015

Dedication

I would like to express my great gratitude to the supervisor of my Ph.D. thesis - Pavel Javorský. His support during my studies and knowledge of the field were truly invaluable. He taught me how to prepare sample and measure the physical properties on it, including the neutron diffraction experiments, as well as to interpret the results of such the measurements and publish them in peer reviewed journals. He was always willing to help me with any problem I faced and always with the enthusiasm and readiness.

I would also like to acknowledge the support and assistance given me by my colleagues on the Department of Condensed Matter Physics during my studies on this department. The regular meetings to improve the knowledge of the field of interest and to solve any difficulty as well as the promptness of my colleagues to help were very inspiring.

I acknowledge the help of Jiří Pospíšil and Michal Vališka with the preparation of the single crystals and their characterization. Great thanks belong also to Marie Kratochvílová for her introducing me to the problematic of electron microscopy and EDX technique as well as for her cooperation during our studies. I highly appreciate my colleagues, Jiří Kaštil, Jan Fikaček and Petr Čermák, for their assistance with everyday problems, measurements and for comfortable atmosphere in our office. The special thanks belong to Petr Doležal for the collaboration on many tasks and all kind of work he did in Prague during last year of my Ph.D. studies.

I am very grateful to Martin Boehm, supervisor of my work in Institut Laue-Langevin, Grenoble, France, for his guidance while commissioning the ThALES instrument as well as for the introduction to the triple-axis-spectroscopy problematic. He made my stay in ILL as comfortable as possible, always willing to help me.

I want to thank also my colleagues in ILL, especially, Jiří Kulda, Paul Steffens, Simon Holbain, Karin Schmalzl, Andrea Piovano and many others for their help with my integration into the TAS group as well as into the ILL everyday life.

I would like to thank also instrument scientists who helped me not only with the neutron experiments realization, but often also with the data treatment: Devashibhai T. Adroja (MARI and IRIS, ISIS, Didcot), Michael Marek Koza (IN6, ILL, Grenoble), Bachir Ouladdiaf (D10, CYCLOPS and Orient Express, ILL, Grenoble), Andreas Hoser (E6, HZB, Berlin), Inés Puente Orench (D1B, ILL, Grenoble), Astrid Schneidewind and Petr Čermák (PANDA, MLZ, Garching), Stéphane Rols (IN4c, ILL, Grenoble) and Martin Boehm and Paul Steffens (ThALES, ILL, Grenoble).

This thesis is dedicated to my parents, Světlana and Milan, for their love, endless support and encouragement during my studies.

I declare that I carried out this doctoral thesis independently, and only with the cited sources, literature and other professional sources.

I understand that my work relates to the rights and obligations under the Act No. 121/2000 Coll., the Copyright Act, as amended, in particular the fact that the Charles University in Prague has the right to conclude a license agreement on the use of this work as a school work pursuant to Section 60 paragraph 1 of the Copyright Act.

In .... date .... signature of the author

Název práce: Elektronové vlastnosti substituovaných cérových sloučenin

Autor: Milan Klicpera

Katedra: Katedra fyziky kondenzovaných látek

Vedoucí disertační práce: doc. Mgr. Pavel Javorský Dr.

Abstrakt: Předmětem této práce je studium vibronových stavů v tetragonálních sloučeninách $CeCuAl_3$ a $CePd_2Al_2$ a jejich vývoj se substitucí jednotlivých prvků. Příprava monokrystalických a polykrystalických vzorků byla následována jejich chemickou a strukturní charakterizací. Na vzorcích byly pozorovány strukturní, magnetické a supravodivé fázové přechody; a následně důkladně studovány. Zásadní experimenty byly provedeny s využitím pružného a nepružného neutronového rozptylu. Získaná data umožnila určit magnetické struktury sloučenin $CeCuAl_3$, $CePd_2Al_2$ a $CePd_2Ga_2$. Energetická spektra substituovaných sloučenin ze sérií $Ce(Cu,Al)_4$ a $CePd_2(Al,Ga)_2$ umožnila přímo pozorovat vývoj krystalového pole a jeho interakce s fonony ve studovaných sloučeninách.

Klíčová slova: intermetalické sloučeniny ceru, vibronové stavy, elektronové vlastnosti, neutronový rozptyl

Title: Electron properties of the substituted cerium compounds

Author: Milan Klicpera

Department: Department of Condensed Matter Physics

Supervisor: doc. Mgr. Pavel Javorský Dr.

Abstract: The subject of this work is the study of vibron states in tetragonal $CeCuAl_3$ and $CePd_2Al_2$ compounds and their development with the substitution of constituent elements. After the preparation of single crystals and polycrystalline samples, the careful chemical and structural characterization was done. The structural, magnetic and superconducting phase transitions in samples were observed and thoroughly investigated. The crucial experiments were performed using the elastic and inelastic neutron scattering techniques leading to the refinement of magnetic structures in $CeCuAl_3$, $CePd_2Al_2$ and $CePd_2Ga_2$. The energy spectra of substituted $Ce(Cu,Al)_4$ and $CePd_2(Al,Ga)_2$ compounds were studied as well allowing to determine the crystal field excitations and their interaction with phonons (vibron states) in these materials.

Keywords: Ce-internetallic compounds, vibron states, electronic properties, neutron scattering

Contents

Introduction

The Ce-based intermetallic compounds stay in the foreground of interest already several decades for their often uncommon and surprising behavior, especially in low-temperature region. The only one $4f$ electron shielded by $5d$ and $6s$ electron orbitals together with the influence of crystal electric field (CEF) stay behind the physical properties as magnetic ordering at very low temperatures, valence fluctuations, heavy-fermion behavior or unconventional superconductivity. Another highly interesting phenomenon was found in several Ce-based materials: the inelastic neutron scattering energy spectra display an additional peak which cannot be described in terms of pure crystal field splitting. The first observation of such a peak was done on cubic $CeAl_2$ compound and the physical model was introduced to describe it soon after [1]. The Thalmaier-Fulde model is based on a strong CEF exciton-phonons coupling in the compound, which results in a new quantum quasi-bound state, so called vibron state, revealing itself as an additional peak in the energy spectra of a compound [1].

A strong magneto-elastic coupling of the $4f$ electrons resulting in a formation of vibron state was observed only in a very few intermetallic compounds, e.g. $PrNi_2$ [2], $CePd_2Al_2$ [3] or $CeCuAl_3$ [4]. The vibron state in latter two materials was observed quite recently and, in contrast with previous compounds, $CePd_2Al_2$ and $CeCuAl_3$ crystallize in the tetragonal crystal structure. The broad study of these two compounds and their substitutions by means of magnetic, transport and mainly neutron scattering experiments forms the content of this thesis.

The main idea of the study is to follow the development of vibron states with the substitution of constituent elements in $CeCuAl_3$ and $CePd_2Al_2$ compounds and to find out the relation between the presence/development/absence of vibron states and another microscopic and also macroscopic properties of these materials. In the same time, we investigate the crystal and magnetic structure of studied compounds and their development with temperature variation. A broad field of experimental methods was used and their descriptions are included in the thesis together with a comprehensive comparison of results with another representatives of tetragonal Ce-based compounds.

The first chapter contains a brief introduction to the problematic of cerium atom and Ce-based intermetallic compounds. The description of experimental methods used during the study follows in chapter 2. Most of the methods are commonly known and frequently used in condensed matter physic research. Therefore, we focus on techniques allowing the preparation of studied compounds as well as their structure and chemical characterization. At the end of chapter 2, we describe the neutron scattering theory and experiments in more details as these experiments were essential for our understanding of properties of studied compounds.

Chapter 3 consists of previous results on the Ce-based compounds belonging to the same family as $CeCuAl_3$ and $CePd_2Al_2$. This chapter also gives the description of vibron states in $CeAl_2$ and $CeCuAl_3$ compounds. The following chapter 4 then contains the main part of the thesis. It comprises every phase of the study on investigated compounds starting from the sample preparation, through the structure and chemical characterization, the measurement of basic bulk properties and culminates with the neutron scattering experiments. The chapter 4 is moreover divided into two parts, where first of them contains the outcome concerning $CeCuAl_3$ compound and its substitutions and second one then consists of the results obtained on $CePd_2Al_2$ single crystal and Al-Ga substituted compounds. The appropriate discussion is given for each part of the thesis. The short conclusive chapter then summarizes main results of the study.

The thesis does not contain the results on several substituted compounds investigated in course of Ph.D. studies of the author. The investigations of structural and bulk magnetic properties of $Ce(Cu,Au)Al_3$ and $CeCu(Al,Ga)_3$ series, superconductivity of $LaPd_2(Al,Ga)_2$ compounds or pressure experiments on $CePd_2(Al,Ga)_2$ compounds are not included in the thesis to increase its readability and clarity. These results are summarized in our papers listed within the thesis and summarized at the end of thesis.

1. Theoretical background

1.1 Materials with $4f$ electrons

The chemical elements with partially filled $4f$ shell attract an attention already several decades. $4f$ metals belong between elements with natural magnetic order, together with transition d-metals and $5f$ elements. They are often called rare-earth metals or lanthanides, although e.g. La does not contain any f-electron. On the other hand, we can consider the lanthanum, to some extent, for the $4f$ element with empty $4f$ shell. It could be very convenient in cases, where the non-magnetic analogue of $4f$ element-based metal is needed for the estimation of physical properties bounded with the crystal lattice.

The magnetic properties of $4f$ elements are strongly influenced by the number of electrons in $4f$ shell. The same applies for the ionic radius of these elements: so called lanthanide contraction takes place in these materials. The ionic radius decreases with increasing atomic number (number of electrons in $4f$ shell). Nevertheless, lanthanides exhibit very similar chemical properties externally. A reason behind such a behavior is found in the electronic structure of these elements. Compared to the transition d-metal, where d-electrons form the last electron shell (where the nuclei is in the center of atom), in the case of rare-earth elements, $4f$ shell is shielded by outermost $5s$ and $5p$ orbitals. Such an electronic structure stays behind above mentioned properties of $4f$ elements and has a great impact on their magnetic properties. Well shielded $4f$ electrons localized relatively close to the nuclei interact with other atoms indirectly, only. Ruderman-Kittel-Kasuya-Yosida interaction (RKKY) considering the hybridization of $4f$ states with spins of conduction electrons is generally responsible for the magnetic ordering in rare-earth based materials. Nevertheless, one should take into account also other indirect interactions as superexchange interaction in oxides and fluorides or exchange interaction between $5d$ states of rare-earth element and other element d-states.

The magnetism in the materials based on rare earth ions is theoretically well described by Hund's rules. As we use the effective magnetic moment, μ_{eff}, quite often in the thesis, we remind to the reader its definition:

$$\mu_{\mathrm{eff}} = g_{\mathrm{J}}\sqrt{J(J-1)}\mu_{\mathrm{B}}. \tag{1.1}$$

g_{J} is Landé factor reflecting mutual orientation of total angular momentum J, orbital momentum L and spin momentum S in real space (see Figure 1.1) defined as:

$$g_{\mathrm{J}} = 1 + \frac{J(J+1)+S(S+1)-L(L+1)}{2J(J+1)}. \tag{1.2}$$

$J = |L-S|$ for $4f$ shell filled from less than one half, $J = L+S$ for more than half-filled $4f$ shell. μ_{B} is then the electron magnetic dipole moment usually called Bohr magneton. Such a definition of μ_{eff} is valid for the material in the paramagnetic state and in non-zero external magnetic field. The randomly oriented magnetic moments are influenced by applied field leading to the non-zero magnetic moment of the material. μ_{eff} for Ce^{3+} free ion is equal to 2.54 μ_{B}.

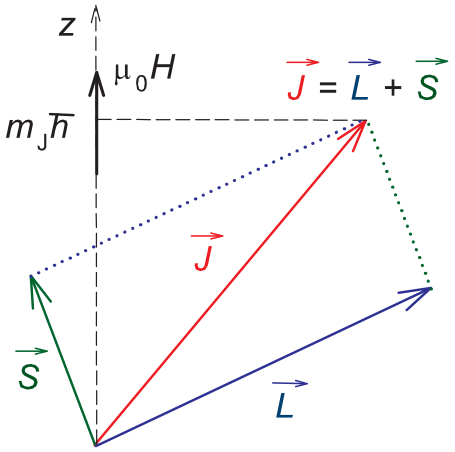

Figure 1.1: The mutual orientation of total angular momentum J, orbital momentum L and spin momentum S in external magnetic field $\mu_0 H$.

Another physical quantity, which could be calculated, is the ordered magnetic moment $\mu_{\rm ord}$:

$$\mu_{\rm ord} = g_{\rm J} J \mu_{\rm B}. \tag{1.3}$$

Compared to the effective magnetic moment, $\mu_{\rm ord}$ is calculated for magnetic ion in ordered state and represents the upper limit of magnetic moment possibly obtained for magnetic material. $\mu_{\rm ord} = 2.14\ \mu_{\rm B}$ in the case of Ce^{3+} free ion.

1.2 Crystalline electric field

The crystal electric field is generally described by the CEF Hamiltonian and can be calculated from first principles. We give here the basic description as the formalism will be used in following chapters. CEF Hamiltonian consists of the sum of multiple CEF parameters, B_m^n, and Stevens' operators, $\widehat{O}_m^n$, (representing $4f$ shell):

$$\widehat{H}_{\rm CEF} = \sum_{mn} B_m^n \widehat{O}_m^n. \tag{1.4}$$

B_m^n are real numbers and the Stevens' operators are operators acting on the electron states. The number of independent CEF parameters differs with the symmetry of crystal structure: the higher symmetry means less CEF parameters. In the case of tetragonal and orthorhombic point symmetry (the case of compounds studies in this thesis), the equation 1.4 is simplified to:

$$\widehat{H}_{\rm CEF}^{\rm tetragonal} = B_2^0 \widehat{O}_2^0 + B_4^0 \widehat{O}_4^0 + B_4^4 \widehat{O}_4^4 + B_6^0 \widehat{O}_6^0 + B_6^6 \widehat{O}_6^6. \tag{1.5}$$

$$\widehat{H}_{\rm CEF}^{\rm orthorhombic} = B_2^0 \widehat{O}_2^0 + B_2^2 \widehat{O}_2^2 + B_4^0 \widehat{O}_4^0 + B_4^2 \widehat{O}_4^2 + B_4^4 \widehat{O}_4^4 + B_6^0 \widehat{O}_6^0 + B_6^2 \widehat{O}_6^2 + B_6^4 \widehat{O}_6^4 + B_6^6 \widehat{O}_6^6. \tag{1.6}$$

For Ce-based compounds the previous formulas are even more simplified:

$$\widehat{H}_{\mathrm{CEF}}^{\mathrm{tetragonal-Ce}} = B_2^0\widehat{O}_2^0 + B_4^0\widehat{O}_4^0 + B_4^4\widehat{O}_4^4, \tag{1.7}$$

$$\widehat{H}_{\mathrm{CEF}}^{\mathrm{orthorhombic-Ce}} = B_2^0\widehat{O}_2^0 + B_2^2\widehat{O}_2^2 + B_4^0\widehat{O}_4^0 + B_4^2\widehat{O}_4^2 + B_4^4\widehat{O}_4^4, \tag{1.8}$$

as the Stevens operators $\widehat{O}_6$ are zero.

Localized character of $4f$ electrons stays behind a very similar physical properties of the free ion and the compound which includes the $4f$ element, including the energy levels or effective magnetic moment. Crystal electric field gives a rise to a strong magnetic anisotropy observed in rare-earth metals and removes the degeneracy of energy multiplets of the $4f$ ions. The symmetry of the crystal structure plays a crucial role here as the CEF has the same point symmetry. Note, that the symmetry of crystal structure in $4f$ element-based compound is not necessarily the symmetry of CEF as the $4f$ atoms in the compound could occupy lattice sites with lower symmetry. The crystal electric field then removes a directional degeneracy of energy multiplets in $4f$ atoms according to CEF symmetry. See Figure 1.2 with the Ce^{3+} ion as an example. Free ion remains $2J+1$ times degenerated. This degeneracy is removed by crystal electric field in the compound. The energies of CEF splitting in $4f$ based materials are counted generally in units or tens of meV (milielectronvolt). Such energies correspond to tens or hundreds of K (Kelvin), $E(\mathrm{meV}) = 11.604\ E(\mathrm{K})$. The CEF splitting is thus possible to consider as a perturbation, which is frequently used in theoretical calculations.

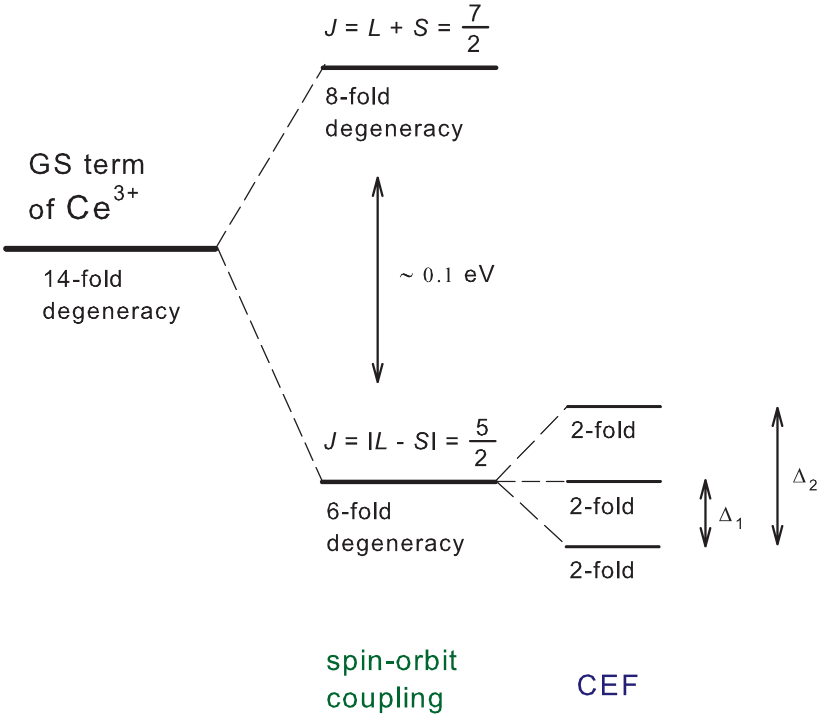

Figure 1.2: The schema of energy levels splitting in Ce^{3+} ion. Spin-orbit coupling and influence of crystal electric field (CEF) on ground state multiplet are depicted.

Ce-based compounds exhibit always the splitting into maximum three energy levels, see Figure 1.2. (The splitting into doublet and quartet is realized only for the cubic structure.) The reason for such a splitting is found in quantum mechanics. Kramer's theorem of degeneracy says, that all energy levels in time-reversal invariant systems have to be double degenerated, i.e. if eigenstate of the Hamiltonian with energy E exists, there must be another state with the same energy E. Kramer's theorem is valid for all systems with an odd total number of fermions (it includes free ion or a system with odd number of electrons). The external magnetic field removes the degeneracy of energy levels.

The CEF parameters, B_m^n, and corresponding energy levels splitting are quite routinely calculated from point charge model and known crystal structure of compound. CEF parameters determined from the measurement (e.g. inelastic neutron scattering or magnetic susceptibility) are the same as theoretical ones in ideal case. In real materials, we observe small differences due to non-ideal distribution of elements and other defects in the crystal. The great importance has the valence state of the $4f$ element. Cerium ion exhibits usually valence number 3+, but it can loose one electron and become Ce^{4+}. The same applies e.g. for $\mathrm{Yb}^{2+} \rightarrow \mathrm{Yb}^{3+}$. The valence state is generally not the same for all ions (of the same element) in the compound leading to the non-integer value, which could be easily sample dependent.

1.3 Magnetic structure of material

Mutual magnetic interactions between ions with not-fully filled electron shell may lead to their regular arrangement. The magnetic order can, however, occur only at sufficiently low temperatures where magnetic interactions outweigh the thermal fluctuations in the material. Above the magnetic ordering temperature the compounds behave as paramagnets, below ordering temperature several magnetic orders could be realized: ferromagnetic, antiferromagnetic and ferrimagnetic (i.e. uncompensated antiferromagnetic) order. The temperature of the transition from paramagnetic to ordered state is called Curie Temperature, T_{C}, for ferromagnet and Néel temperature, T_{N}, for antiferromagnet. The magnetic dipoles are identically oriented in ferromagnet, whereas more complicated magnetic moment arrangements can be found in antiferromagnetically ordered material. The magnetic dipoles in antiferromagnet could be reoriented by external magnetic field (typically quite strong) which leads to the metamagnetic transition to the ferromagnetic state.

The arrangement of magnetic moments in the compound (at temperatures lower than T_{C} or T_{N}) is periodic and forms its magnetic structure. The magnetic structure can be easily related to the crystal structure of the compound. The crystallographic unit cell is the smallest possible unit cell of magnetic structure. For the ferromagnetic material, the crystallographic and magnetic unit cell coincide as all the magnetic moments are oriented to the identical direction in space. The different directions of magnetic moments in the antiferromagnet then often lead to larger magnetic unit cell. One can introduce the ratio between crystallographic and magnetic unit cell, so called propagation vector of magnetic structure $\vec{k}$. The components of propagation vector are determined as the ratio between the size of crystallographic and magnetic unit cell in appropriate direction. When both unit cells are identical, propagation vector $\vec{k} = (0, 0, 0)$.

The introduction of propagation vector is of great importance as $\vec{k}$ is the vector of reciprocal space and can be used in scattering theory formalism. The magnetic moment on j^{th} atom in the unit cell is described as:

$$\mu_j = \sum_{\{\vec{k}\}} \vec{m}_{j,\vec{k}} e^{-i\vec{k}.\vec{T}}, \tag{1.9}$$

where $\vec{m}_{j,\vec{k}}$ is a complex basis vector directly determined from propagation vector and position of the j^{th} atom in the unit cell. $\vec{T}$ is the lattice translation vector associated with the position of the magnetic moment. Summation is done over all sets of $\vec{k}$-vectors as the magnetic structure could be described by more than one propagation vector. Generally, the magnetic structure could be very complex, including incommensurate (the magnetic structure is not commensurate with the crystallographic one) or modulated structures described by propagation vectors with irrational components.

The equation 1.9 is significantly simplified in case when the $\vec{m}_{j,\vec{k}}$ is real. Magnetic moment μ_j have to be real as it is the physical quantity. Therefore the imaginary part of exponential must (i) equal to zero or (ii) cancel each other with imaginary part of exponential corresponding to the propagation vector $-\vec{k}$. The first scenario is realized for simple magnetic structures and implies the commensurate magnetic structure, the second one then assumes two propagation vectors: $\vec{k}$ and $-\vec{k}$ and leads to amplitude modulated magnetic structure.

The detailed description of magnetic structure formalism as well as the determination of magnetic structures using the neutron diffraction techniques could be found e.g. in Ref. [5].

1.4 Cerium and Ce-based compounds

The cerium atom with electron configuration [Xe] $4f^1 5d^1 6s^2$ represents very special case among the rare-earth elements. Only one $4f$ electron screened by outermost $5s$ and $5p$ orbitals stays behind unique and often exotic physical properties of Ce and Ce-based compounds. Although the $4f$ electron is shielded by outermost electron levels, the influence of magnetic field, temperature, pressure and/or chemical pressure on compound could lead to the transition of $4f$ electron from its localized state to the conduction band. The valence number of the ion is then changed from Ce^{3+} to Ce^{4+} and cerium becomes non-magnetic. Together with the loss of magnetic moment, also the crystal electric field is changed. Moreover, the real sample is not ideal as it contains defects and stoichiometry variations. Also the crystal structure itself (its symmetry) may cause the occupation of some atomic positions preferentially with Ce^{3+} and other positions with Ce^{4+}. Such electron configuration in the compound is called mixed-valence state and could be effectively detected by microscopic measurements, e.g. neutron scattering techniques allow to distinguish between atomic sites with different values of magnetic moments. The cases, when the both configurations have non-zero probability and ions are varying between them, are referred to as a valence-fluctuating state. The average life time of each configuration is so short that most experiments cannot distinguish between them. The compound then reveals a non-integer valence state.

The consequences of valence state instability of Ce lead to significant changes in physical properties among Ce-based compounds. Often, the compounds exhibit a mixture of Ce^{3+} and Ce^{4+} ions. If the content of 4+ valence ions reaches certain value, the magnetic ordering is lost and the compound stays non-magnetic even at very low temperatures. The situation, when the total valence of cerium ions in the compound subtle differs from 3+, happens quite often: the compound orders magnetically, usually at low temperature, and exhibits properties often quite different from these expected for purely magnetic compound.

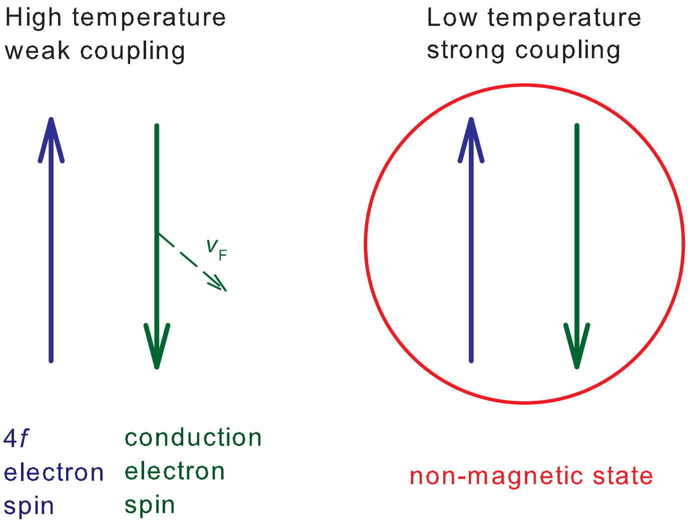

Figure 1.3: The schema of Kondo singlet. A weak coupling at high temperature, and a strong coupling at low temperature are demonstrated.

The two mechanisms compete in Ce-based compounds frequently: (i) the interaction leading to the magnetic order, generally of RKKY type, and (ii) so called Kondo interaction (see Refs. [6] and [7] for detailed description). The conduction electrons scatter on the localized magnetic moments in the metal, which leads to the formation of electron singlets (see Figure 1.3). The Kondo singlet consists from one $4f$ electron and one conduction electron with oppositely oriented spin, the magnetic moment of whole singlet is equal to zero. However, the coupling between electrons is only weak at high temperature (the conduction electrons pass by magnetic electron with the Fermi velocity v_{F}) and becomes stronger with decreasing temperature, see Figure 1.3. A typical behavior bounded with Kondo singlet creation in the compound can be traced: the logarithmic temperature dependence of the electrical resistivity, reduced sizes of the magnetic moments in the magnetically ordered and paramagnetic state or strongly enhanced Pauli paramagnetic susceptibility and electronic coefficient of the specific heat.

The competition between RKKY and Kondo interaction in the compound can be tentatively described by Doniach's diagram [8], see Figure 1.4. The strength of interactions is marked as T_{RKKY} and T_{K}, respectively, where the energy for each interaction could be expressed as:

$$k_{\mathrm{B}}T_{\mathrm{RKKY}} \approx J_{\mathrm{ex}}^{2}n(E_{\mathrm{F}}), \tag{1.10}$$

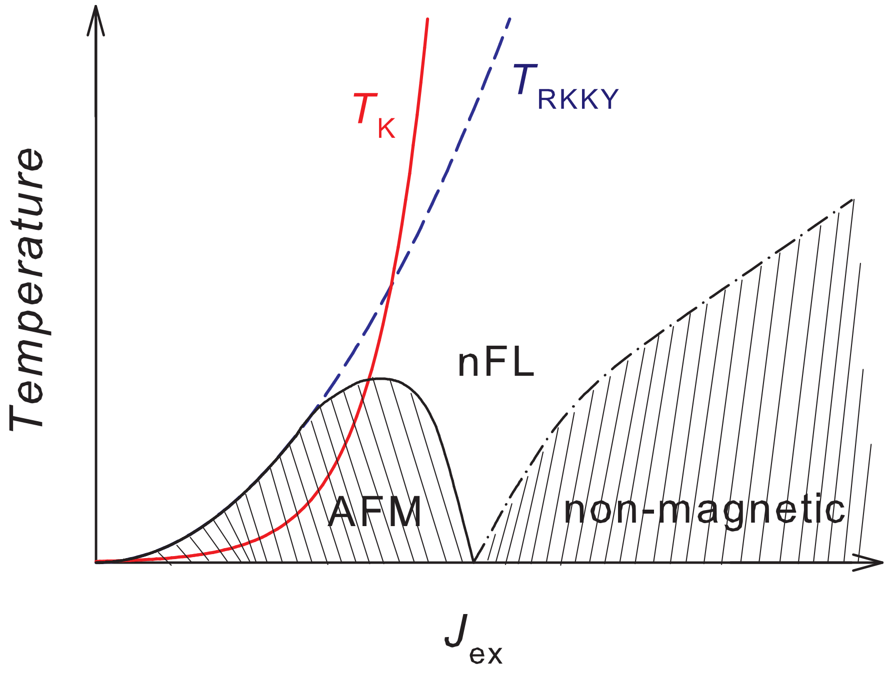

Figure 1.4: Doniach's diagram. J_{ex} is the exchange constant. The strength of RKKY and Kondo interaction is marked as T_{RKKY} and T_{K}, respectively. AFM is the antiferromagnetic state, nFL stays for non-Fermi-liquid state. See text for further details.

$$k_{\mathrm{B}}T_{\mathrm{K}} \approx exp(-\frac{1}{2J_{\mathrm{ex}}n(E_{\mathrm{F}})}). \tag{1.11}$$

k_{B} is Boltzmann constant, the exchange constant J_{ex} then represents the interaction between $4f$ states and conduction electrons in the compound and $n(E_{\mathrm{F}})$ is the density of states at Fermi level. A weak interaction between $4f$ electrons and conduction electrons leads to small J_{ex} and the compound orders magnetically. The Kondo interaction prevails for sufficiently high values of J_{ex}, leading to the non-magnetic state. On the border between magnetic and non-magnetic state, the strength of RKKY and Kondo interactions is comparable and wide range of physical phenomena arise. Non-Fermi-liquid state (nFL) and quantum criticality are most prominent of them. Moreover, the exchange constant J_{ex} can be influenced by chemical and/or external pressure which allows us to pass from the magnetically ordered regime to nFL state and further to the non-magnetic region.

2. Experimental techniques

The experimental techniques described in this chapter were used during our study of $CeCuAl_3$, $CePd_2Al_2$ and their substitutions. We prepared and characterized all the samples by ourself on the ground of Department of Condensed Matter Physics. The basic magnetization and transport measurements were performed in Magnetism and Low Temperatures Laboratories, MLTL (http://mltl.eu/), which are supported within the program of Czech Research Infrastructures (project no. LM2011025). The experiments with the usage of neutron scattering were done on instruments in neutron facilities as stated below.

2.1 Sample preparation

The studied poly- and single- crystalline samples were prepared from high purity elements, see Table 2.1, in relatively large amount (tens and units of grams, respectively) mainly because of needs of neutron scattering experiments. The pollycrystals were prepared by arc-melting of pure elements in appropriate stoichiometry. In the case of compounds with gallium, 0.5% of Ga was added to account for its higher evaporation. The melting process took place under protection of an argon atmosphere. The water-cooled tungsten electrode and copper crucible were used. All the samples (maximal weight of 2 g) were four times flipped and remelted to ensure good homogeneity. All the single crystals were prepared from the polycrystalline precursors; typical weight of precursor was ≈ 8 g.

Table 2.1: The purity of elements used for the preparation of studied compounds. The purity is written in the N-form: 4N5 $\equiv$ 99.995% metals basis, Alfa Aesar.

element	La	Ce	Cu	Au	Pd	Al	Ga
purity	3N	2N8	6N	5N	4N5	6N	7N

The Czochralski pulling method belongs to the relatively commonly used methods for single crystal growth. We prepared most of the studied single crystals by this method in the modified tri-arc furnace installed in Department of Condensed Matter Physics. The polycrystalline precursor of appropriate stoichiometry is melted up by three tungsten electrodes and levitates on water-cooled copper crucible. First, the melted material is heated for certain amount of time, in our case always ≈ 0.5 hour, to ensure homogeneity of the melt. The crucible, and with it also the melt, are rotated in addition. Secondly, the water-cooled seed is introduced to the melt - the tungsten seed could be used in the first step, in further step a part of prepared ingot serves as seed. In the third step, the seed (and ingot) is pulled out of the melt with constant speed, in our case the speed was 6 - 8 mm per hour. In the same time, the ingot rotates (typically 4 rotations per minute) in the opposite sense than the crucible. The speeds of pulling and rotation and mainly their stability during the whole growing process are of great importance. Another important parameter is the temperature of the melt, which has similar or rather more significant effect. The speeds and mainly the temperature must be regulated in order to allow the formation of an interface between the melt and ingot at which the crystallization process takes place. After successful connection of the melt and solid ingot, several millimeters of crystal are grown. The critical phase in the growing process is the formation of so called 'neck', which follows. The diameter of the ingot is tuned by the temperature of melt in order to get rid of all single crystal grains but one. Afterwards, the diameter is enlarged again to maximally 5 mm (for larger diameter we need to use another furnace). If possible, the second neck is managed and we grow the ingot as long as possible. The last critical part is the ending of the ingot. The diameter of the ingot should be narrowed very slowly and it should be very narrow when it is separated from the melt. The temperature transfer from the melt to the ingot should be as low as possible to prevent a formation of defects as twinning or inclusion of the foreign phase by fast-cooling. The pictures of initial phase of preparation of $CeCuAl_3$ single crystal and prepared ingot are shown in Figure 2.1.

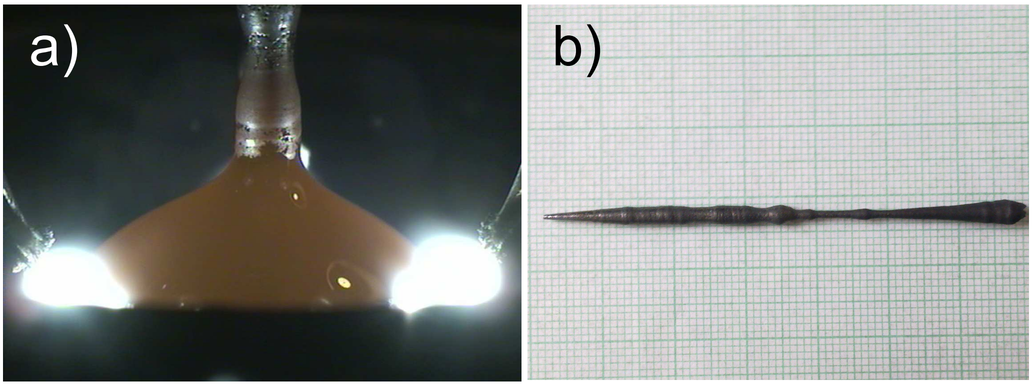

Figure 2.1: The photos of a) initial phase of preparation by Czochralski pulling method and b) prepared ingot of $CeCuAl_3$.

Another type of preparation of our single crystals was the floating zone method. We needed large amount of $CeCuAl_3$ for powder neutron diffraction experiment. To ensure the homogeneity of the sample, whole amount of material was prepared as one large single crystal by floating zone method. The precursor in the shape of a rod of 5 mm diameter and $\approx$ 18 g weight was used for the preparation by the optical floating zone furnace (model: FZ-T-4000-VI-VPM-PC). The growing process took place under 6N Ar protective atmosphere with 125 kPa pressure and the flow rate of 0.5 liter per minute. In contrast with the Czochralski method, in the case of floating zone method the sample is heated up only locally, which leads to lower evaporation of constituent elements, contamination by residual gas and better stability of the growth itself. The pulling rates and rotation speed were the same as used in the case of preparation by Czochralski pulling method.

2.2 Structure and chemical characterization

The sample prepared by methods described above may exhibit many defects. A different crystal structure and a wrong stoichiometry are the most important of them. Another problem could be a stoichiometry variation in the sample, inclusions of foreign phases and a presence of oxides of constituent elements. Moreover, one should take into account also the occupation of lattice sites of one element by other element with similar ionic radius, especially in substituted compounds. In the case of single crystal, one has to verify first, that prepared ingot consists of only one grain. The opposite case leads to the sample with certain anisotropy given by similar orientation of all grains or even to the polycrystal.

All prepared samples were investigated by means of energy dispersive X-ray diffraction (EDX) and powder X-ray diffraction measurements. The single crystals were checked by Laue X-ray and neutron diffraction, in addition.

2.2.1 Energy dispersive X-ray analysis

One of the ways how to effectively investigate the stoichiometry of prepared sample is the energy dispersive X-ray analysis. This method is based on the characteristic energies of inter-orbital transitions of electrons in the atom. These energies are different for each chemical element and thus could serve for its identification.

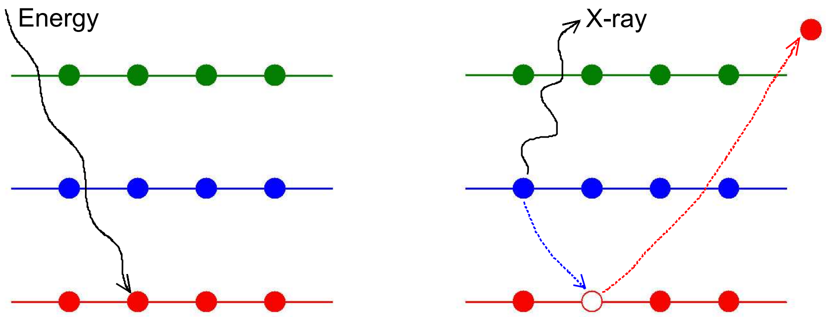

Figure 2.2: The schema of electron inter-orbital transition. The introduction of an appropriate energy to the electron leads to its excitation. Excited electron leaves the atom and its place is filled up by an electron from higher energy level, which is followed by an emission of characteristic X-ray radiation.

The sample is irradiated by the beam of high-energy electrons in the first step. If the energy transmitted to the electron on certain energy level (in certain atomic orbital) is high enough, the electron leaves the atom. The hole after excited electron is filled by the electron from other level (orbital) in order to minimize the energy of whole atom. The transition of electron from the higher energy level to level with lower energy is accompanied by emission of X-ray radiation with characteristic energy, which is equal to difference between appropriate energy levels. For illustration see Figure 2.2. For detailed description see for instance Ref. [9, 10]. By the irradiation of a certain part of the sample, one obtains the X-ray spectrum containing the spectra from all constituent elements. A careful analysis of this spectrum leads to the finding of sample stoichiometry. The accuracy of EDX analysis is quite high, the error is up to a few percent. On the other hand, one should take into account the limits of EDX technique. The most important one is the penetration depth of electrons, which makes from EDX the surface technique. An increased attention should be then dedicated to the shape and size of the studied sample. The overlap of peaks from different elements spectra forms another difficulty.

The EDX technique is quite well implemented into the practice nowadays and it is used routinely. The EDX measurement on our samples was performed on the scanning electron microscope Mira (Tescan) equipped with secondary electrons detector, back-scattered electrons (BSE) detector and with EDX analyzer by Bruker Axs. The incident electron beam energy was ranging from 0 to 30 keV. The EDX analysis confirmed the correct stoichiometry and phase purity of all further used samples. The error of the analysis was up to 3% in all cases (precision of the method). The BSE picture of the sample surface (note the scratches from the polishing of the sample) and EDX maps of distribution of constituent elements in $CeCuAl_3$ are presented in Figure 2.3 as an example.

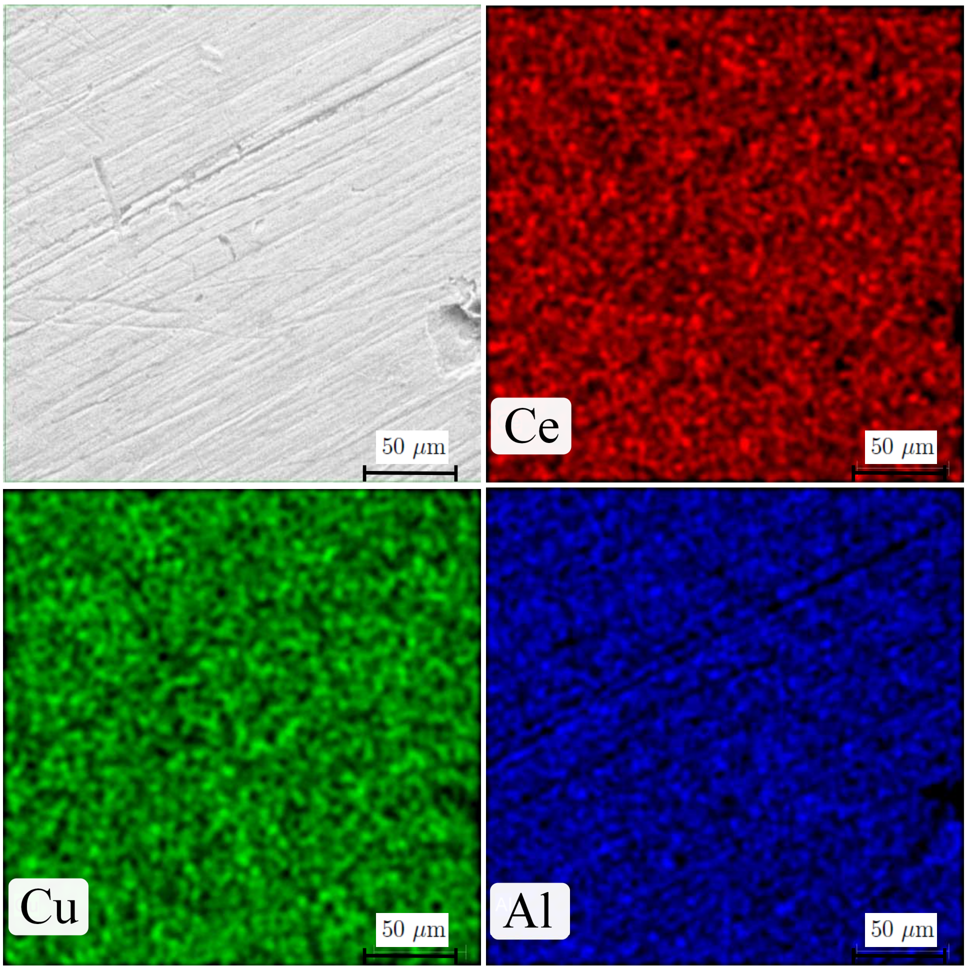

Figure 2.3: The BSE picture of the sample surface and the maps of distribution of constituent elements in $CeCuAl_3$ single crystal.

2.2.2 Diffraction techniques

The crystal structure of all prepared samples was studied by means of X-ray diffraction. The diffraction process of X-ray radiation on the periodic lattice is well known already more than 100 years, Max von Laue obtained the Nobel Prize in Physics already in 1914, William Henry Bragg and William Lawrence Bragg then one year later. For this reason, we do not describe the method in detail and remind here only the obligatory Bragg's law:

$$n\lambda = 2d.sin\theta. \qquad (2.1)$$

n is positive integer number. λ is the wavelength of used radiation. d stays for distance between crystallographic planes and θ is the angle between incident radiation and the sample surface.

The investigation of our powder samples was performed on Bruker D8 Advance diffractometer equipped with the Cu $K\alpha_{1,2}$ X-ray source (the initial wavelengths 1.54056 Å and 1.54439 Å, respectively). The Bragg-Brentano $\theta - 2\theta$ geometry was implemented. The obtained diffraction patterns were consequently refined using the Rietveld analysis employing the Fullprof software [11].

High temperature powder X-ray diffraction measurements were performed on powdered $CeCuAl_3$ single crystal and on polycrystalline $LaCuAl_3$ using the PANanalytical MPD diffractometer with MRI high-temperature chamber in conventional BB symmetric θ-2θ scan. Tantalum strip heater and platinum radiation heater were used as a heating elements, the heating rate was 5°C per minute. The sample was directly put to tantalum strip heater in order to have a good thermal contact. The pressure in heating chamber was of the order 10^{-2} Pa to protect the tantalum strip from corrosion and to ensure the same conditions for measurements at each temperature. The measurement was done at temperatures from 32 to 500°C.

To characterize the single crystals, two methods were used. First, Laue diffraction method. The X-ray or neutron radiation does not need to be adjusted in any way as we need a broad spectra of wavelengths. The Bragg's condition is satisfied for each set of crystallographic planes and appropriate wavelengths resulting in the array of spots on so called Lauegram. The spots on Lauegram form the hyperboles, where each hyperbola belongs to the one set of crystallographic planes. The symmetry of crystallographic planes in the single crystal leads to the symmetry of diffraction patterns in Lauegram. The transmission and back-reflection modifications of Laue diffraction method are commonly used, leading to the same results.

Besides the orientation of single crystal, the Laue technique is used to investigate its perfection. The quality of single crystal is mirroring in the size and shape of the diffraction spots. The distorted or smeared spots could be a result of bended or twisted crystal. The sample containing more than one grain or the twinning can be also easily identified.

The quality and orientation of our single crystals were verified by both Laue X-ray diffraction and Laue neutron diffraction techniques. The usage of X-ray diffraction in conventional laboratory is limited and therefore it becomes the surface technique for bulk samples. Scans over all the crystal including the places rotated exactly by 180° with respect to previous ones should be the matter of course. However, the sample might still contain more than one grain. The neutrons have a large penetration depth and whole sample volume could be investigated in the same time. The Laue neutron diffraction experiments were performed on Orient Express and CYCLOPS (CYlindrical Ccd Laue Octagonal Photo Scintillator) instruments [12] at Institute Laue-Langevin (ILL), Grenoble, France. The example of Lauegram taken by Orient Express diffractometer on $CeCuAl_3$ single crystal

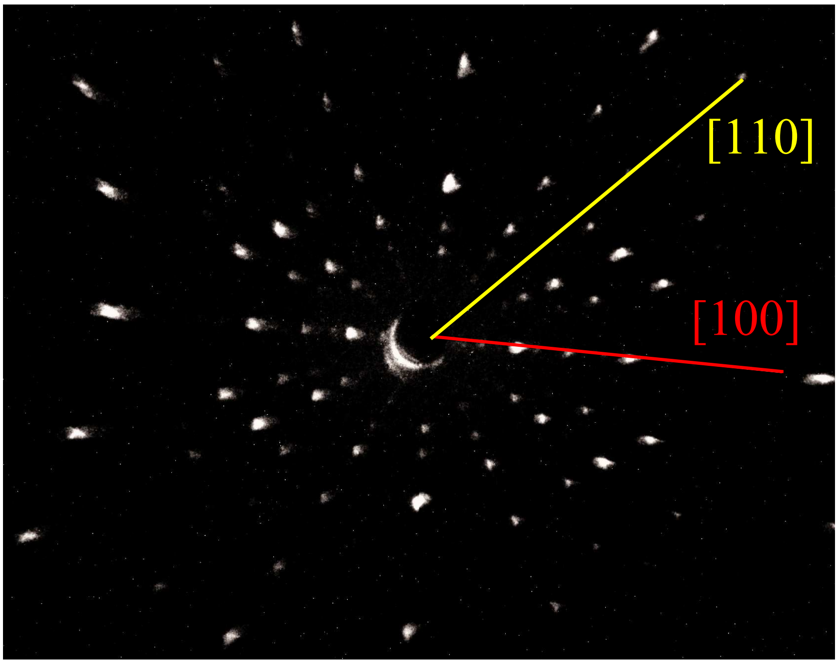

Figure 2.4: Lauegram taken by Orient Express diffractometer on $CeCuAl_3$ single crystal.

is presented in Figure 2.4.

The Laue neutron diffraction could be also used for the investigation of magnetic structures in the single crystals as the neutrons carry the magnetic moment (see section 2.6). The Lauegram contains besides the crystal structure spots also the spots corresponding to the magnetic structure. These spots could be described by the propagation vector of magnetic structure. CYCLOPS instrument equipped with the orange cryostat was used for such a magnetic study on our samples (see Figure 4.15).

The second approach how to investigate the crystal and magnetic structures of single crystal is usage of the 4-circle goniometer. The experimental setup allows to rotate the crystal in order to reach almost any wanted structural or magnetic reflection. More sophisticated software is needed for the instrument manipulation and also for the evaluation of diffraction patterns. The crystal structure of $CeCuAl_3$ single crystal was determined using the Bruker APEXII CCD diffractometer equipped with Mo X-ray tube. Structure factors have been extracted from single crystal diffraction patterns and the structure was identified using SHELXS-97 (Sheldrick, 2008). The single crystal of prism-shape with (0.080 x 0.100 x 0.140 mm) dimension was used for the measurements at temperatures 296 and 150 K. To investigate the magnetic structure of $CeCuAl_3$, we used D10 diffractometer with four-circle goniometer at ILL, Grenoble.

2.2.3 Differential scanning calorimetry

Differential scanning calorimetry (DSC) is a thermo-analytical technique based on the measurement of the amount of heat required to increase the sample temperature. The reference sample with a well-defined heat capacity needs to be prepared beforehand. The sample measurement itself is tightly bound to the measurement of reference: both the sample and reference are maintained at nearly the same temperature throughout the experiment, which allows together with previous calibration to obtain heat-temperature dependence of the sample. The complementary technique is called differential thermal analysis (DTA). While DSC measures the energy required to keep both the reference and the sample at the same temperature, DTA measures the difference in temperature between the sample and the reference when they are receiving the same amount of heat.

DSC allows to observe the differences in the heat flow between the sample and calibrated reference, while keeping both at the same temperature. These differences correspond to the absorption and emission of the heat by the sample, while undergoing the phase transition. The process of the phase transition could be endothermic or exothermic, which is detected also by DSC. Endothermic process is bounded with 'negative' peak in the temperature dependence of heat flow as the heat is absorbed during the phase transition. The solid-liquid transition represents such a process. Exothermic process is then exactly opposite and is accompanied by the 'positive' peak in temperature-heat transfer development. Thus, not only the temperatures of the phase transitions in the sample, but also its type could be determined by DSC measurement.

Differential scanning calorimetry was carried out on $\mathrm{CeCuAl_3}$ single crystal as well as on $\mathrm{LaCuAl_3}$ polycrystalline sample in order to obtain melting temperatures and to find any sign of presence of other transition as well as to verify the phase purity of the sample. Measurements were performed under protection of He atmosphere on SETSYS Evolution 24 instrument (SETARAM Instrumentation Company) and data were processed using SETARAM software. Heating and cooling scans were taken with the rate of 10°C per minute in temperature range from 28 to 1400°C.

2.3 Magnetization measurements

The magnetization measurement techniques are well known and standardly used in condensed matter research. We do not describe them here and kindly ask reader to see a large number of publications, e.g. Refs. [13, 14], for details. Instead, we focus on the description of magnetization in the sample in paramagnetic and ordered state.

The total magnetic moment of the sample in the paramagnetic state is equal to zero. The individual magnetic moments on magnetic ions compensate each another due to their random orientation in the material. Nevertheless, the application of external magnetic field could overcome the thermal fluctuations of magnetic moments and the material exhibits a non-zero magnetization M. The response of the sample in the paramagnetic state to the applied magnetic field, so called magnetic susceptibility χ, is generally described by modified Curie-Weiss law:

$$\chi \approx \frac{M}{H} = \frac{N_\mathrm{A}\mu_\mathrm{B}^2\mu_\mathrm{eff}^2}{3k_\mathrm{B}(T-\theta_\mathrm{p})} + \chi_0, \tag{2.2}$$

where N_A is the Avogadro constant, θ_p is paramagnetic Curie temperature and χ_0 stays for the Pauli and Van Vleck paramagnetic susceptibility. We note, that the susceptibility is not the scalar quantity, in general. Both the magnetization and magnetic field are vectors, thus the susceptibility is the tensor of 3x3 dimension. The simplified relation could be used, to some extent, in the cases, when the magnetization vector has the same direction as the magnetic field, i.e. the significant crystallographic direction of the sample crystal structure is oriented along the applied field. The effective magnetic moment obtained by fitting the experimental data to the Curie-Weiss law is generally comparable with theoretically predicted μ_{eff} from equation 1.1.

The magnetization and alternate current (ac-) susceptibility measurements were performed using the Physical Property Measurement System (PPMS) and Magnetic Property Measurement System (MPMS), Quantum Design, installed in the Magnetism and Low Temperatures Laboratories, MLTL (http://mltl.eu/). The magnetic field ranges from 0 to 14 T and to 7 T for PPMS and MPMS instruments, respectively. Polycrystalline samples used for the measurement were crushed into fine powder and afterwards fixed in a random orientation by glue (Canagon) in a plastic capsule. Typical weight of the sample was $\approx$ 60 mg. The single crystals were measured in the prism-shaped form with the long edge cut along significant crystallographic directions oriented along magnetic field direction. Such experimental arrangement allows us to neglect the difficulty due to the demagnetizing factor [15].

2.4 Specific heat

The measurement of the specific heat belongs among the standard techniques implemented during the investigation of physical properties of the material. The specific heat namely reflects the microscopic properties and their changes in the sample, which makes it very important quantity for condensed matter physics. The total specific heat of the sample is considered to consist of electronic, C_{el}, phonon, C_{ph}, and magnetic, C_{mag}, contributions:

$$C_{\mathrm{p}} = C_{\mathrm{el}} + C_{\mathrm{ph}} + C_{\mathrm{mag}}. \tag{2.3}$$

General problem with the specific heat data treatment originates in a difficult separation of individual components from total specific heat.

The electronic contribution of specific heat originates in the presence of conduction electrons near the Fermi level in all metallic materials and could be expressed as:

$$C_{\mathrm{el}} = \frac{1}{3}\pi^2 n(E_{\mathrm{F}}) k_{\mathrm{B}}^2 T \equiv \gamma_{\mathrm{el}} T. \tag{2.4}$$

$n(E_{\mathrm{F}})$ stays for the density of states on the Fermi level, γ_{el} is then the Sommerfeld coefficient of electronic specific heat.

The lattice vibrations (quantized as phonons) are tightly bound with a thermal energy given to matter and form significant contribution to its specific heat. $3n$ branches (n is number of atoms in an elementary unit cell) of the phonon spectrum is divided into 3 acoustic and $3n$-3 optic branches and are described by the Debye and Einstein models, respectively. The wavevector of acoustic phonons is linearly dependent on the frequency, while the optic phonons exhibit non-zero frequency also in the center of Brillouin zone. The phonon contribution to the specific heat in the compounds with lattice periodicity could be then described by relation:

$$C_{\mathrm{ph}} = C_{\mathrm{ph_D}} + C_{\mathrm{ph_E}} = 9k_{\mathrm{B}}N_{\mathrm{A}}(\frac{T}{\theta_{\mathrm{D}}})^3 \int_0^{\frac{\theta_{\mathrm{D}}}{T}} \frac{x^4 e^x}{(e^x-1)^2}dx + k_{\mathrm{B}}N_{\mathrm{A}} \sum_{i=1}^{3n-3} (\frac{\theta_{\mathrm{E_i}}}{T})^2 \frac{e^{\frac{\theta_{\mathrm{E_i}}}{T}}}{(e^{\frac{\theta_{\mathrm{E_i}}}{T}}-1)^2}, \tag{2.5}$$

where θ_{D} and θ_{E} stay for the Debye and Einstein temperatures, respectively. When describing the phonons in the material, one should take into account also the effect of anharmonicity, which is not included in previous formula [16]. The high temperature limit of equation 2.5 is equal to $3R$ per one mole of the material, while C_{ph} at low temperatures reveals a cubic dependence on the temperature. The specific heat for the non-magnetic compound in the low temperature region could be thus written as:

$$C_{\mathrm{p}} = C_{\mathrm{el}} + C_{\mathrm{ph}} = \gamma_{\mathrm{el}}T + \beta T^3 = \gamma_{\mathrm{el}}T + \frac{12\pi^4 R}{5\theta_{\mathrm{D}}^3}T^3 \tag{2.6}$$

The magnetic contribution to the specific heat consists in non-zero total magnetic moment of atoms in matter. The crystal electric field in the material influences the electronic properties of such atoms (splits degeneration of the multiplet ground state, see subsection 1.2), which leads to the rise of the entropy and thus also the specific heat. The CEF contribution to C_{mag} is often called Schottky contribution:

$$C_{\mathrm{Schottky}} = k_{\mathrm{B}}N_{\mathrm{A}}(\frac{\sum_{i=1}^{n}(\frac{E_i}{k_{\mathrm{B}}T})^2 e^{-\frac{E_i}{k_{\mathrm{B}}T}}}{\sum_{i=1}^{n} e^{-\frac{E_i}{k_{\mathrm{B}}T}}} - (\frac{\sum_{i=1}^{n}\frac{E_i}{k_{\mathrm{B}}T} e^{-\frac{E_i}{k_{\mathrm{B}}T}}}{\sum_{i=1}^{n} e^{-\frac{E_i}{k_{\mathrm{B}}T}}})^2). \tag{2.7}$$

Any change of the electronic properties of atoms in the material leads to the change of the entropy and thus also to the change of specific heat. The formation of magnetic ordering, transition to the superconducting (SC) state or structural transitions reveal themselves as anomalies in the temperature evolution of specific heat.

The determination of individual contributions to the specific heat of general compound represents quite difficult task. Nevertheless, in the special cases, the magnetic contribution could be, to some extent, estimated after the subtraction of the electronic and phonon contributions of the non-magnetic analogue from total specific heat of investigated compound. Such an approach is frequently used in the specific heat data treatment of rare-earth based compounds, where La, Y and Lu analogues could be employed.

The magnetic entropy of the material could be easily calculated from C_{mag}:

$$S_{\mathrm{mag}}(T') = \int_0^{T'} \frac{C_{\mathrm{mag}}}{T}dT. \tag{2.8}$$

A comparison of S_{mag} to the theoretical value:

$$S_{\mathrm{mag}} = R\ln(2J+1) \tag{2.9}$$

could be than easily done revealing inter alia the strength of Kondo interaction in Ce-based compound or even the presence of short-range magnetic correlations. The theoretic value of S_{mag} for Ce^{3+} ion is equal to $R\ln(6) = 14.9$ J.K^{-1}.mol^{-1}.

The specific heat measurement on studied samples was performed using the time-relaxation method on PPMS instrument, see e.g. Ref. [17]. The thermal contact between sample and sample holder was provided by the apiezon N grease, which served for the attachment of the sample to holder in the same time. All the sample measurements were forestalled by the measurement of the sample holder with appropriate amount of grease to determine the contribution of apiezon to measured specific heat precisely. The contributions of the sample holder and apiezon were subtracted afterwards. The measurements at temperatures from interval $(0.4 - 5)$ K were provided on ≈ 2 g samples, the samples with ≈ 20 g weigh were used for the measurement at temperatures between 1.8 and 300 K. The larger sample allows us to get a good accuracy with respect to the increase of sample holder contribution to measured specific heat at higher temperatures.

2.5 Electrical resistivity

The electrical resistivity of the non-magnetic compound generally consists from only two contributions: residual resistivity, R_0, and electron-phonon part, R_{ph}. The total electrical resistivity is then described by the Matthiessen's rule, where R_{ph} could be described by the Bloch-Grüneisen formula:

$$R(T) = R_0 + R_{\mathrm{ph}}(T) = R_0 + A(\frac{T}{\theta_D^R})^n \int_0^{\frac{\theta_D^R}{T}} \frac{x^n}{(e^x - 1)(1 - e^{-x})} dx. \tag{2.10}$$

A is a constant depending on the velocity of electrons at the Fermi surface, the Debye radius and the number density of electrons in the metal. $\theta_{\mathrm{D}}^{\mathrm{R}}$ stays for the Debye temperature determined from resistivity measurement. In the case of one atom in an elementary unit cell, $\theta_{\mathrm{D}}^{\mathrm{R}}$ should reach a value obtained from specific heat measurement via equation 2.5. In the case of more than one atom per unit cell, the equation 2.5 needs to be corrected. Integer number n depends on the type of interaction in the material: $n = 2$ points out to the electron-electron interaction, $n = 3$ is typical for the transition metals with strong $s - d$ electrons scattering and $n = 5$ implies electron-phonon scattering in the material.

The electrical resistivity of compound containing magnetic ions can be described by Mattheissen's rule as:

$$R(T) = R_0 + R_{\mathrm{ph}}(T) + R_{\mathrm{el}}(T), \tag{2.11}$$

where the R_{el} represents the contribution from the electron-electron scattering. The determination of individual contribution to the electrical resistivity is problematic, similarly as in the case of specific heat. Another difficulty represents the type of magnetic order: in the case of antiferromagnet, the equation 2.11 must be corrected by truncation factor for a different periodicity of the magnetic lattice. In special cases, we can assume the same R_{ph} contribution for magnetic and non-magnetic analogues and estimate R_{el}. This contribution is for Fermi-liquid-like system proportional to the square of temperature:

$$R_{\mathrm{el}}(T) = DT^2. \tag{2.12}$$

In condensed matter, we observe several mechanisms, which influence the electrical resistivity development. Superconductivity leads to the zero electrical resistivity below critical temperature and critical magnetic field. A logarithmic increase of resistivity with decreasing temperature due to the screening of magnetic moments by conduction electrons represents another case, when the system cannot be described purely on the basis of above mentioned relations. For further reading see e.g. Refs. [18, 19].

The electrical resistivity was measured using a classical four-point schema with transversal current-field mode on PPMS instrument. The prism-shaped samples with (≈ 20 x 4 x 4 mm^3) dimensions were connected to the electrical circuit by Cu wires and colloidal silver paste. Single crystalline samples cut along significant crystallographic directions (mostly the same samples as used for magnetization measurements) were connected to the electrical circuit with the electrical current, j, aligned along the long sample edge.

The double layered cylindrical pressure cell [20] and pressure exchange medium Daphne 7373 oil [21] were used for the measurement up to 3 GPa in temperature range 2 - 300 K. The manganin wire was used as the sensor to determine the pressure at room temperature. The uncertainty of pressure determination of 0.05 GPa originates in the electrical resistivity measurement of the manganin wire. Above 2.2 GPa, additional error of 0.2 GPa should be considered because of solidification of Daphne 7373 oil at room temperature [21]. Another asymmetric experimental error (≈ 0.2 GPa) occurs in low pressure region ($p < 1$ GPa) at low temperatures as the pressure decreases by cooling.

2.6 Neutron scattering

The neutron scattering techniques belong to the most powerful tools for the condensed matter investigation. Neutron consists of quarks u-d-d leading to the zero electric charge (or strictly speaking, charge lower than experimental error) and non-zero magnetic moment. Such properties allow the neutron non-destructively penetrate the matter to depth of several centimeters. It interacts with the nuclei via the strong interaction (there is no Coulomb barrier to overcome) and with magnetic moments of unpaired electrons via dipole-dipole interaction. It brings out the information not only about the crystal (nuclear) structure, but also about the magnetic structure of the material. The important properties of the neutron are its wavelength or energy and momentum. The wavelengths of the order of 10^{-10} m (= Angstroems) make the neutron an ideal probe for atomic and molecular structure investigation. Moreover, the size of nuclei is typically several femto-meters (10^{-13} m), the interaction between the neutron and nucleus is thus nearly point-like. The energy $\approx$ meV is then in the same range as diffusive motion, phonons, magnons, vibration modes of molecules etc. The random sensitivity to individual chemical elements and also individual isotopes represents another highly convenient property of neutron, which is frequently used not only in condensed matter research, but also for the investigation of chemical and biological materials.

The production of neutrons by fission and spallation processes requires large facilities. Such a drawback is common for both neutron scattering and complementary synchrotron X-ray radiation scattering techniques. Comparing both techniques, the X-ray scattering works with radiation energy in order of keV, has a smaller penetration depth and mainly, the radiation is scattered by electron density and thus the heavy elements contribute to the diffraction patterns stronger than the light ones. On the other hand, great advantages of synchrotron radiation are broad spectrum of wavelengths, high flux, brilliance and high stability of source.

The thesis is not aiming to describe the X-ray and neutron scattering techniques in detail, for further reading e.g. Refs. [22, 23, 24] are recommended. We give here only several basic relations and basic description of used instruments, which is necessary for a good understanding of the data aquirement and treatment within the thesis. The neutron scattering could be generally divided into two types, elastic and inelastic, based on the way neutron interacts with the matter. The main difference between these types of scattering lies in the kinetic energy conservation. While, the elastic scattering (also called diffraction) contains the processes, in which the total kinetic energy of the neutron and target does not change during the experiment, the inelastic scattering deals with the processes, where the total kinetic energy before and after scattering process differs (part of the kinetic energy is converted to other type of energy, e.g. deformation or excitation energy). The neutron is elementary particle with no excitable internal degrees of freedom and the target is typically very massive, therefore elastic scattering implies the energy conservation of the target.

2.6.1 Neutron diffraction

The measured intensity of scattered beam represents an overall output of general X-ray or neutron scattering experiment. The relation between the intensity, I, and microscopic properties of the sample is not always straightforward as several factors reflecting the sample and instrument features take place. Moreover, the microscopic properties of the sample are included in so called structure factor, F, which appears in the following formula only as a square:

$$I = L_{\mathrm{f}} A E_x P |F|^2. \tag{2.13}$$

As the structure factor is generally a complex number, the phase of F is lost and sophisticated approach has to be used to restore it. Lorentz factor, L_{f}, is reflecting a different speed of different reciprocal lattice points as they are passing through the Ewald sphere during the measurement. We restrict ourselves only to easy formulas which applies to our measurements on powder diffractometers D1B (ILL, Grenoble) and E6 (HZB, Berlin) and on triple axis spectrometer D10 (ILL, Grenoble) in 'elastic mode':

$$L_{\mathrm{powder}} = \frac{1}{\sin 2\theta \sin\theta}, L_{\mathrm{single\ crystal}} = \frac{1}{\sin\theta}. \tag{2.14}$$

Lorentz factors for various types of measurements can be found e.g. in Ref. [25]. The absorption of the material, A, plays an important role in the scattering experiment as it influences the measured intensity depending on the sample composition (elemental and isotopic), size and shape of the sample and on wavelength of neutron radiation. The extinction, E_x, represents another important factor in the kinematic theory of diffraction. The extinction is strongly dependent on the size and mosaicity of domains in the sample and could be thus determined mostly only by fitting the experimental data. We restrict ourself to mention only phenomenological Zachariasen formula, which is implemented in the Fullprof package [11] and which was used during the refinement of our single crystal data. For further reading, see e.g. Ref. [26]. Preferential orientation factor, P, then corrects a non-random orientation of grains in the powder sample and could be described by e.g. March function [11]:

$$P_{hkl} = \int (f_{\mathrm{cor}}^2 \cos^2\alpha + \frac{\sin^2\alpha}{f_{\mathrm{cor}}})^{-\frac{3}{2}}, \tag{2.15}$$

where the correlation factor, f_{cor}, expresses the degree of preferential orientation. The preferential orientation does not occur in the sample when $f_{\mathrm{cor}} = 1$, takes the plate-shape form for $f_{\mathrm{cor}} < 1$ and needle-shape for $f_{\mathrm{cor}} > 1$ [11].

Before we move to the structure factor formalism, it is useful to introduce the scattering vector $\vec{Q}$. The neutron radiation from source is typically coming to the sample as the plane wave described by the wave vector $\vec{k}_1$. The scattering process leads to the scattered spherical wave, which could be approximated by plane wave with $\vec{k}_2$; it is generally valid by the detector position. The scattering vector $\vec{Q}$ is then characterized as the difference between wave vectors $\vec{k}_1$ and $\vec{k}_2$. The absolute values of $\vec{k}_1$ and $\vec{k}_2$ are identical in the case of elastic scattering ($|\vec{k}_1| \neq |\vec{k}_2|$ for inelastic scattering). The whole scattering process is schematically drawn in Figure 2.5.

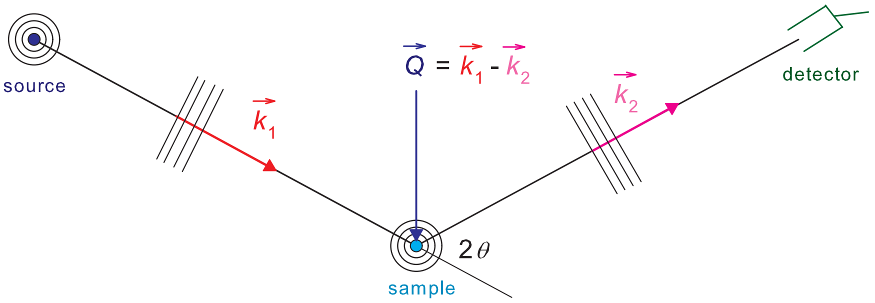

Figure 2.5: The diffraction process on the sample. The radiation in the form of plane waves and purely elastic scattering are considered for simplicity. 2θ stays for scattering angle and $\vec{Q}$ is the scattering vector.

The structure factor, F, in equation 2.13 stays for both types of scattering, scattering of neutrons on nuclei - F_{N} - and neutron magnetic moment scattering on moments of unpaired electrons in material - F_{M}. Both types of scattering contribute to the measured diffraction patterns with similar intensity, however, only in low 2θ region. F_{M} is strongly $\vec{Q}$-dependent for the same reason as structure factor in X-ray scattering, i.e. it depends on the Fourier transform of the spatial distribution of unpaired electrons around the nucleus. The magnetic form factor, $f_j(\vec{Q})$, differs from the X-ray form factor though: the neutron magnetic scattering takes place only on the outer (unpaired) electrons, whereas X-ray scattering is heavily weighted also by the core electrons. F_{N}, on the contrary, depends on the scattering length (or scattering amplitude), b, which is $\vec{Q}$-independent: the wavelength of neutrons used for the scattering experiments (Angstroem, Å) is typically 4-5 orders of magnitude larger than the dimension of the nucleus (fm). The nucleus can be thus treated as the point target, i.e. delta function in space. The Fourier transform of delta function is a unity and therefore b is element and isotope dependent constant. The value of b for individual isotope cannot be calculated theoretically, experimentally determined values are tabulated. The nuclear and magnetic structure factors could be written in the following forms:

$$F_{\mathrm{N}}(\vec{Q}) = \sum_{j} b_j e^{i\vec{Q}\vec{R}_j} e^{-W_j}, \tag{2.16}$$

$$F_{\mathrm{M}}(\vec{Q}) = \sum_{j} f_j(\vec{Q}) \mu_{j\perp} e^{i\vec{Q}\vec{R}_j} e^{-W_j}, \tag{2.17}$$

where first exponential describes the relation between the direct and reciprocal space and second one stays for the temperature Debye-Waller factor. $\mu_{\perp}$ represents the component of magnetic moment perpendicular to the scattering vector $\vec{Q}$. Neutron diffraction sees only this perpendicular component of magnetic moment due to the dipole-dipole interaction.

The summation of nuclear and magnetic scattering contributions to total intensity differs for individual experimental setups: $F^2 = F_{\mathrm{N}}^2 + F_{\mathrm{M}}^2$ for experiment employing unpolarized neutron beam, whereas $F^2 = (F_{\mathrm{N}} + F_{\mathrm{M}})^2$ for polarized radiation, for example. For further reading see e.g. Refs. [22, 23, 24].

2.6.2 Inelastic neutron scattering

The second type of interaction of neutron with the matter, inelastic neutron scattering, deals with the scattering processes, in which the energy and momentum of the incoming and scattered neutrons differ; $\left|\vec{k}_1\right| \neq \left|\vec{k}_2\right|$ ($\left|\vec{k}_1\right| \equiv k_1$). Compared to the elastic case, the scattered intensity is significantly different and the measurement itself requires more sophisticated experimental setup. In general, two types of inelastic neutron scattering instruments are employed: time of flight spectrometer (ToF) and triple-axis spectrometer (TAS). The former instrument is usually used for the measurement on polycrystalline samples and other chemical or even biological materials, while the later one is dedicated to the measurement on single crystals. For the measurement of large Q-range on the single crystal could be used the ToF spectrometer. We will describe these two types of instruments as well as the inelastic scattering in more details in present thesis as a significant part of it consists of the results from our neutron scattering experiments using the ToF spectrometers IN4 (ILL, Grenoble), IN6 (ILL, Grenoble), MARI (ISIS, Didcot) and IRIS (ISIS, Didcot) and TAS instruments D10 (in elastic mode, only; ILL, Grenoble), ThALES (ILL, Grenoble), IN20 (ILL, Grenoble) and PANDA (MLZ, Garching). The instruments are usually constructed depending on the requested energy range and resolution for the experiment; generally, we can divide them to the 'cold' instruments (IN6, IRIS, ThALES, PANDA) and 'thermal' instruments (IN4, MARI, IN20).

ToF and TAS instruments

The measurement with time of flight spectrometer begins with the monochromatization of white neutron beam. Two approaches are used, in general. First, the neutron beam is partially monochromatized by the two counter-rotating discs choppers and afterwards diffracted by the monochromator crystal leading to the specific wavelength of neutrons. In the next step, the neutron beam is pulsed into very short bursts by Fermi chopper (one can imagine the rotating set of parallel slits, which transmits the beam only when the neutron path is parallel to the slits). This is the case of e.g. IN4 instrument. Second approach consists in usage of a set of chopper discs, used e.g. for IN5 instrument at ILL, Grenoble. A first pair of choppers creates the polychromatic neutron bursts (the same process as in the former approach). Another chopper removes harmonics due to the large bandwidth of wavelengths. Further chopper avoids overlapping of scattered neutrons from successive bursts after sample by suppressing some of the produced pulses. Finally, a pair of monochromator counter-rotating discs chops a single wavelength (a narrow band of nearly monochromatic neutrons). The preparation of neutron beam for the experiment is significantly easier in the case of spallation source as the neutron bursts are produced directly by the source. Well defined monochromatic bursts of neutrons interact with the sample and the scattered neutrons are counted by area detectors covering relatively large part of space around the sample. The energy which is exchanged between the neutron and the sample can be then calculated from the difference in arrival time of neutrons to the detector (with respect to elastically scattered neutrons at the detector position), i.e. from the speed of individual neutrons.

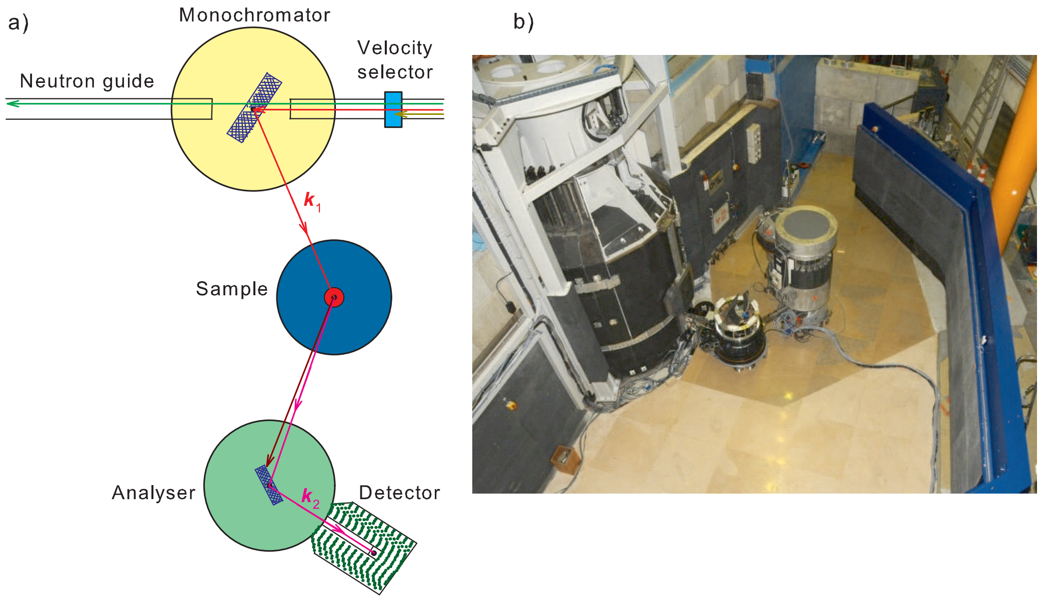

Figure 2.6: The 2D scheme of triple axis spectrometer and photo of ThALES instrument, ILL, Grenoble.

Triple axis spectrometer consists of monochromator, sample table, analyser and detector. See Figure 2.6 for the illustration. In the first step, the neutrons of selected wavelength(s) are diffracted by the monochromator crystals. Velocity selector (one can imagine chopper) could be used for the primary selection of neutron energy or wavelength; especially, the higher harmonics of wavelength could be effectively sorted out by incorporation of velocity selector in front of the monochromator. The second scattering process takes place at the sample position, while we have a control on the incoming neutron properties ($\vec{k}_1$). Neutrons scattered by the sample could be registered by (two-dimensional) detector, which is the case of our measurement on D10 instrument in 'elastic mode', or are analyzed by the analyzer (the third scattering process). The analyzer crystals diffract only the neutrons of specific $\vec{k}_2$, which are counted by a tube detector in the final step of the measurement. The whole experiment takes place within so called scattering plane, usually; nevertheless, the special type of analyzer-detector setup (e.g. FlatCone, ILL, Grenoble) allowing also the measurement out of the plane could be employed. During the typical experiment on TAS, one holds wave vector $\vec{k}_1$ or $\vec{k}_2$ constant while varying the other. Detailed description of TAS as well as all optical components can reader find in many publications, we recommend e.g. Ref. [24].

Scattering triangle

Let us describe the inelastic neutron scattering process on sample in detail: the incoming neutron of specific wavelength (energy) and momentum interacts with the sample both elastically (see previous subsection) and inelastically. The later process leads to the change of energy or/and momentum of neutron. The detection and analysis of scattered neutron properties then give the information about the microscopic nature of studied material. The whole scattering process is frequently described in the following way (compare with elastic case and Figure 2.6). The scattering vector $\vec{Q}$ could be still characterized as the difference between wave vectors $\vec{k}_1$ and $\vec{k}_2$ as in the case of elastic scattering:

$$\vec{Q} = \vec{k}_1 - \vec{k}_2. \tag{2.18}$$

However, the vectors of incoming and scattered waves do not have the same size in the inelastic case, thus $\vec{Q}$ is generally not the vector of reciprocal lattice ($\vec{Q} \neq \vec{G}$, where $\vec{G}$ is reciprocal lattice vector). It is convenient to relate the momentum transfer to the nearest reciprocal lattice vector, i.e. $\vec{Q} = \vec{G} + \vec{q}$, where $\hbar\vec{q}$ is so called relative momentum. The three vectors $\vec{Q}$, $\vec{k}_1$ and $\vec{k}_2$ form so called scattering triangle, which is depicted in Figure 2.7.

Here, one should make a connection between the expression 2.18 and Figure 2.7 by looking on the size of scattering vector:

$$Q^2 = k_1^2 + k_2^2 - 2k_1k_2\cos 2\theta, \tag{2.19}$$

where 2θ stays for the angle between incoming and scattered wave vectors, i.e. scattering angle. Except the momentum $\hbar\vec{Q}$ (or relative momentum $\hbar\vec{q}$), the so called energy transfer needs to be introduced to describe the inelastic scattering processes:

$$\hbar\omega = E_1 - E_2 = \frac{\hbar^2}{2m}(k_1^2 - k_2^2), \tag{2.20}$$

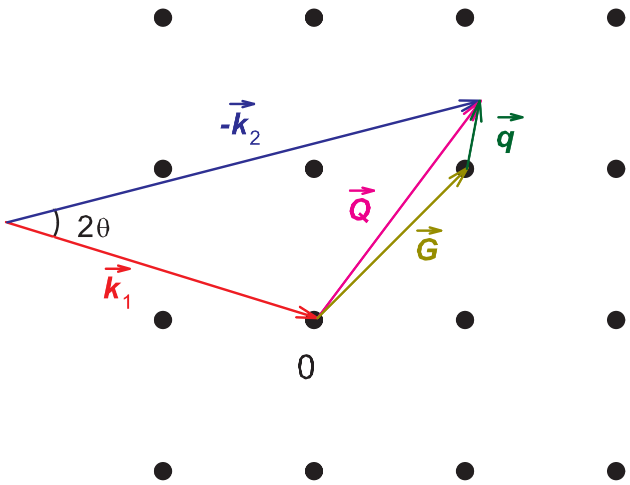

Figure 2.7: The scattering triangle of inelastic neutron scattering on reciprocal lattice.

where the kinetic energy of neutron is described by non-relativistic formula as the speed of neutron is of order of km per second, i.e. 5 orders of magnitude lower than speed of light. m stays for the neutron mass. Now, we can introduce a scattering function $S(\vec{Q},\omega)$, which is defined in reciprocal $(\vec{Q},\omega)$ space. But first, we turn to the practical experimental usage of above listed formulas. Any $(\vec{Q},\omega)$ point of reciprocal lattice can be reached by an infinite number of combination of $(\vec{k}_1,\ \vec{k}_2)$, however, the experimental arrangement (see Figure 2.6) as well as the constrains of the neutron beam (technical and physical) reduce significantly our options. During the experiment, one holds wave vector $\vec{k}_1$ fixed (i.e. the direction and energy of incoming neutrons are fixed), while the chosen $(\vec{Q},\omega)$ point is reached by detection of the final energy (energy of scattered neutron given by $\vec{k}_2$)

$$E_2 = \frac{\hbar^2}{2m}k_2^2 = E_1 - \hbar\omega = \frac{\hbar^2}{2m}k_1^2 - \hbar\omega \tag{2.21}$$

at a scattering angle 2θ:

$$\mathrm{cos}2\theta = \frac{k_1^2 + k_2^2 - Q^2}{2k_1k_2}. \tag{2.22}$$

The analogical measurement can be done (and usually it is done) in the configuration with $\vec{k}_2$ fixed. The measurement limits are given in formulas 2.21 and 2.22. Let us look at the elastic case ($k_1 = k_2$, $\hbar\omega = 0$) for example. The largest value of $Q = 2k_1 = 2k_2$ can be reached for $2\theta = 180^{\circ}$, i.e. for backscattering. Thus the neutron can transfer twice its initial momentum, in maximum.

Frequently, the inelastic scattering measurement is performed, while $\vec{Q}$ fixed. Two regimes depending on the mutual size of $\vec{k}_1$ and $\vec{k}_2$ could be distinguished:
- $k_1 > k_2$, according to relation 2.21 energy transfer $\hbar\omega > 0$, energy is transferred

from the incident neutron to the sample and an excitation in the sample is created, while the neutron gets de-excited.
• $k_1 < k_2$ and thus $\hbar\omega < 0$, the sample gives a quantum of energy to the neutron - an excitation in sample is annihilated and neutron gets excited. The energy gain/loss processes lead us to the proper introduction of scattering function $S(\vec{Q}, \omega)$.

Scattering function

The present thesis does not intend to describe the scattering process in detail, we restrict ourself to the main results of scattering theory, only, and recommend e.g. Refs. [23, 24] for further reading. The scattering process in general can be described by the so called differential cross section. This quantity express the probability of the neutron being scattered by the scattering center, or in other worlds, probability of a neutron passing from the state $\vec{k_1}$ to the state $\vec{k_2}$ while exchanging the energy $\hbar\omega$ with the sample, and for nuclear scattering is usually written as:

$$\frac{d^2\sigma_{\vec{k}_1\to\vec{k}_2}}{d\Omega dE_2} = \frac{k_2}{k_1}\frac{1}{2\pi\hbar}\sum_{\lambda_i} p(\lambda_i)\sum_{j,j'}^{N} b_j b_{j'}^* \int_{-\infty}^{\infty} dt \left\langle \lambda_i | e^{-i\vec{Q}.\vec{R_{j'}^0}} e^{i\vec{Q}.\vec{R_j}(t)} | \lambda_i \right\rangle e^{-i\omega t}. \quad (2.23)$$

Here, one can define the scattering function $S(\vec{Q}, \omega)$ as:

$$\frac{d^2\sigma_{\vec{k}_1\to\vec{k}_2}}{d\Omega dE_2} \equiv \frac{k_2}{k_1} S(\vec{Q}, \omega). \quad (2.24)$$

The formula for differential cross section (and thus also for scattering function) describes all scattering processes, i.e. both coherent and incoherent processes. The scattering function and its $\vec{Q}$ and ω dependencies can be directly measured by scattering experiment. The equation 2.23 (and thus also equation 2.24) could be further separated as the coherent scattering depends on the average scattering length of a scatterer: $b_j b_{j'}^* \to \langle b_j \rangle \left\langle b_{j'}^* \right\rangle$, while incoherent scattering is determined by the deviation from the scattering length average: $b_j b_{j'}^* \to (\left\langle b_j^2 \right\rangle - \langle b_j \rangle^2)$. The coherent scattering gives us the information about the correlations that exist between all the scatterers. The information about the cooperative effects among different atoms, such as elastic Bragg scattering or inelastic scattering by phonons or magnons is given just by coherent neutron scattering. Whereas, the incoherent scattering brings the information about the correlation of a particle with itself in time and describes thus the dynamics in the sample.

The formula 2.23 is significantly simplified in the case of elastic scattering and we can get back to the neutron diffraction description used in previous subsection. If we subtract the elastic contributions from differential cross section, then $S(\vec{Q}, \omega)$ corresponds to fluctuations in the sample, as a function of momentum and energy. An important property of the scattering function is the principle of detailed balance:

$$S(-\vec{Q}, -\omega) = e^{-\frac{\hbar\omega}{k_{\mathrm{B}}T}} S(\vec{Q}, \omega). \quad (2.25)$$

The detailed balance expresses the fact, that the probability of a transition in the sample depends on the statistical weight factor for the initial state. The probability is lower for annihilation of excitation than for excitation creation as it is asymmetric in ω. Therefore the negative branch of $S(\vec{Q}, \omega)$ will always be inferior to the positive branch. As seen from equation 2.25, the temperature plays crucial role: at very low (zero) temperature, the sample is in ground state. The sample cannot give any energy to the neutron as there is no excited state. Therefore $S(\vec{Q}, \omega) = 0$ for $\omega < 0$. At high temperature ($k_{\mathrm{B}}T >> \hbar\omega$), the factor $e^{-\frac{\hbar\omega}{k_{\mathrm{B}}T}} \approx 1$ and thus the scattering function becomes more and more symmetric with the increasing temperature.

The whole scattering function formalism can be used also for the definition of scattering of neutron on magnetic spins in material. However, we mention here only the relation between magnetic scattering function (obeying detailed balance principle) and the imaginary part of dynamical susceptibility:

$$S_{\mathrm{mag}}(\vec{Q}, \omega) = \frac{\chi''(\vec{Q}, \omega)}{1 - e^{-\frac{\hbar\omega}{k_{\mathrm{B}}T}}}. \tag{2.26}$$

The commonly known fluctuation-dissipation theorem relates the measured scattering function to dissipative part of a linear response function, i.e. it quantifies the relation between the fluctuations in a system at thermal equilibrium and the response of the system to applied perturbations. For further reading, we recommend e.g. Ref. [27].

Collective excitations

Finally, we turn to a brief description of physical properties of the sample measured by inelastic neutron scattering techniques. Above, we have shown, that neutron scattering techniques bring the information about crystal (nuclear) structure and magnetic structure of the material. Moreover, the fluctuations in the sample could be investigated as function of the momentum and energy. Now, we focus on the collective excitations in the matter, phonons and magnons in particular, which can be effectively studied by inelastic neutron scattering measurements.

The lattice vibrations in the material are quantized as phonons and could be observer indirectly by macroscopic methods as e.g. specific heat or electrical resistivity. The neutron scattering allows us to directly study the phonon spectrum of the material. The emission (absorption) of phonons corresponds directly to energy loss (gain) of probing neutron. On the basis of such a measurement, one can construct so called dispersion relations, $\omega_j(\vec{q})$, for a given material. Every j defines one out of $3n$ phonon branches, where n is number of atoms in an elementary unit cell. If $n > 2$ and there are different atoms in unit cell, three acoustic branches are present: one longitudinal (the displacement of the atoms takes place along the wave propagation) and two transversal branches (perpendicular movement of atoms to the energy transfer direction is observed). Acoustic phonons are just coherent movements of atoms (of the lattice) out of their equilibrium positions. Acoustic phonons exhibit a linear relationship between frequency and phonon wavevector for long wavelengths (low value of q) and for $q \to 0$ the energy transfer also tends to zero. The rest of phonon branches ($3n - 3$) represent out-of-phase movement of the atoms in the lattice (one atom moves to the given direction, while neighboring atom to opposite direction - it is caused by different mass or charge of individual atoms in the lattice) and are called optical modes. The optical phonons exhibit non-zero frequency also in the center of the Brillouin zone as positive and negative ions at adjacent lattice sites move against each other, creating a time-varying electrical dipole moment.

The magnons (= quanta of spin waves) in the magnetic material could be described in a very similar way as phonons, taking the magnetic lattice instead of crystal lattice. Thermal energy and quantum zero-point fluctuations cause the fluctuation of individual magnetic moments in an ordered structure. The spins in the material are coupled to one another by exchange interactions leading to the collective excitations. One can again directly measure the dispersion relations $\omega_j(\vec{q})$ of spin waves in the material by neutron scattering techniques. In general, the dispersion relations for ferromagnet and antiferromagnet differs significantly as the spin wave intensity for antiferromagnet is strong near an antiferromagnetic superlattice peak and weak near a Bragg peak of the nuclear lattice. The dispersion relations for Heisenberg ferromagnet and antiferromagnet with only nearest-neighbor interactions at small q are quadratically and linearly dependent on q: $\omega_j(\vec{q}) \propto q^2$ and $\omega_j(\vec{q}) \propto q$, respectively. One should define the scattering function for each type of material separately. Moreover, the multiple magnon scattering or magnetic domains in the material have to be taken into account.

One can continue with the neutron scattering theory and with description of neutron scattering techniques in detail. We did not mention a large amount of important aspects and properties of scattering on matter, e.g. diffuse scattering, usage of polarized neutrons, spin echo technique or very important resolution function. Nevertheless, given introduction should be sufficient for good understanding to the present thesis. We finish the theoretical part here and recommend e.g. Refs. [23, 28, 24] for further reading.

3. Vibron states

The electron–phonon (e–p) interaction is often neglected in many materials because only subtle effects of this interaction are observed. Nevertheless, there are many materials in which the e–p interaction has to be taken into account, for example the BCS superconductors. Another interesting feature, the strong interaction between crystal field excitations and phonon modes has been described in a few cases. This type of interaction leads to the formation of a vibron quasi-bound state, which has been directly observed as an additional peak in the energy spectra of several Ce-based intermetallic compounds, e.g. $CeAl_2$ [29, 30], $CePt_2$ [31, 32], $CePd_2Al_2$ [3] or recently $CeCuAl_3$ [4], and also in $PrNi_2$ [2]. An additional peak in energy spectra of mentioned compounds could be described within Thalmeier–Fulde model [1], which was generalized also for compounds crystallizing in tetragonal structure [3, 4]. Vibron states are featured by a strong magneto-elastic coupling between orbital and lattice degrees of freedom. Such a coupling results in the changes of macroscopic properties as well as in a new type of (hybrid) magneto-phonon mode [1, 4].

3.1 Vibron states in $CeAl_2$

The most prominent (and probably first) compound, where the vibron state was observed is cubic $CeAl_2$. First inelastic neutron study by Steglich et al. [29] was published in 1979. Already three years later, Thalmeier and Fulde developed a theory behind the observation of an additional peak in the crystal electric spectrum of $CeAl_2$ [1].

$CeAl_2$ crystallizes in cubic face-centered Cu_2Mg-type structure (cubic Lave phase, C15, space group 227). Such a crystal structure is common also to $CePt_2$ [31, 32] and $PrNi_2$ [2]. Ce atoms in this structure form a diamond lattice, while Al atoms occupy tetrahedral positions [33]. $CeAl_2$ is the Kondo compound which orders antiferromagnetically below Néel temperature of 3.8 K. Although the antiferromagnetic ordering was ascertained [34], the magnetic structure was not completely solved for more than 30 years (despite the efforts). Finally, Schweizer et al. [35] determined the magnetic structure as incommensurate double-$\vec{k}$ structure with magnetic moments on two Ce sites described by two elliptical helices of opposed chiralities lying in the $(1\bar{1}0)$ plane.

The inelastic neutron scattering study of crystal field excitations in $CeAl_2$ [29] led to the observation of two CF-like peaks in energy spectrum. According to the Kramer's theorem (see section 1.2), Ce^{3+} ions in the $4f^1$ electronic configuration ($J = \frac{5}{2}$) exhibit always the splitting into maximum three energy levels, see Figure 1.2. In the case of cubic structure, the splitting into doublet and quartet is realized, only. Therefore, one expects only one peak in the energy spectrum of $CeAl_2$ bounded with only one CF excitation from doublet ground state Γ_7 to excited quartet Γ_8. The explanation of two peaks in $CeAl_2$ spectrum given by Thalmeier and Fulde [1] leads to Figure 3.1. Instead of expected excited quartet Γ_8, two crystal field levels are observed. The interaction of CF exciton with high phonon density of states ($\hbar\omega_0 = 12$ meV) results in a new bound state [1] (panel b) in Figure 3.1) and two CF-like peaks in energy spectrum at 8.9 and 15.7 meV

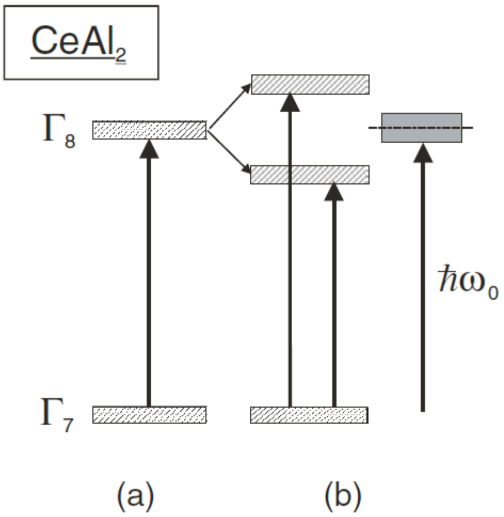

Figure 3.1: The schema of energy levels splitting in CeAl$_2$ taken from Refs. [1, 30]. Panel a) shows the expected line splitting, while panel b) represents observed splitting. The grey region (right) corresponds to energies with high phonon density of states.

are observed [29].

Both theoretical description [36] and investigation of phonon branches in CeAl$_2$ [30, 33] have supported former Thalmeier-Fulde theory [1]. The energy spectrum thus cannot be described only by pure CF hamiltonian. Another term describing the CF exciton-phonons interaction has to be taken into account [1]:

$$\widehat{H}_{\mathrm{tot}} = \widehat{H}_{\mathrm{CF}} + \widehat{H}_{\mathrm{int}} = \sum_{mn} B_m^n \widehat{O}_m^n - g_0 \sum_{\mu} (a_\mu + a_\mu^+) \widehat{O}_\mu . \tag{3.1}$$

The large value of magneto-elastic constant, $g_0 = 0.54$ meV, compared to other RAl$_2$, was supported by the pronounced softening of the c_{44} elastic mode. And it was claimed that the origin of large value of magneto-elastic constant lies in the hybridisation of Ce $4f$ electron with conduction electrons [36]. Also the experimental observation of low-temperature inelastic linewidths much larger than the width of elastic line [37] was satisfactorily explained by dynamic crystal field theory [38]. Despite both the theory and the experimental investigation of vibron states have brought a significant piece of knowledge about this phenomenon, especially in the case of CeAl$_2$, the research on this subject is still not finished. The vibron states in tetragonal compounds CePd$_2$Al$_2$ [3] and CeCuAl$_3$ [4] remain still not sufficiently explained and form the content of this thesis.

3.2 Tetragonal CeTX_3 compounds and vibron state in CeCuAl$_3$

The tetragonal CeTX_3 or more generally CeT_xX_{4-x} compounds, where T is a transition element d-metal and X is a p-metal, exhibit various ground states and phenomena depending on the actual chemical composition and/or applied external pressure. Most of these compounds, for example CeRhGe$_3$ [39], CeAuAl$_3$ [40]

or $CeCoGe_3$ [41], order antiferromagnetically at low temperatures. Several other compounds exhibit ferromagnetic order, e.g. $CeAgAl_3$ [42] or $CeCuGa_3$ [43], or paramagnetic ground state with signs of valence fluctuations like $CeRuSi_3$ [44]. Spin-glass order was observed in $CePtAl_3$ [45]. The electronic properties of these compounds seem to be rather sensitive to details of the crystal structure. The relation between crystal structure type and magnetic order was discussed in the case of $CeCuGa_3$ [43], where the antiferromagnetic ground state with incommensurate propagation vector is observed for compound crystallizing in $BaNiSn_3$-type structure [46, 47], whereas the ferromagnetic order is revealed for $CeCuGa_3$ adopting the $BaAl_4$-type of tetragonal structure [43]. The observation of the pressure induced superconductivity in the non-centrosymmetric $BaNiSn_3$-type of crystal structure of antiferromagnetically ordered $CeRhSi_3$ and $CeIrSi_3$ [48, 49] is particularly remarkable. The recent inelastic neutron scattering study of $CeCuAl_3$ revealed another highly interesting feature: crystal field exciton-phonon interaction leading to the formation of a vibron quasi-bound state [4].

The magnetic behavior of $CeCuAl_3$ is generally discussed as a result of the interplay between the magnetic RKKY and Kondo interactions [50, 51, 45, 52, 4]. The magnetic properties are also influenced by the low lying first excited CF state, splitting between the ground state and first excited state amounts ≈ 1.3 meV as found by neutron scattering experiment [4]. The enhanced electronic specific heat at low temperatures characterized by a large γ_{el} coefficient is often considered as a sign of the heavy-fermion state in $CeCuAl_3$ [50, 51]. However, more detailed analysis which considers the small CF splitting leads to a much smaller γ_{el} value, almost comparable with normal metals [53]. $CeCuAl_3$ orders antiferromagneticaly with slightly sample dependent Néel temperature $T_{\text{N}} \cong 2.5-2.9$ K [50, 51, 45, 52]. The antiferromagnetic ground state nature was concluded mainly on the basis of occurrence of a maximum in the $M(T)$ dependencies [50, 51, 45]. On the other hand, the magnetization curves do not show any clear signs of behavior that would point to the antiferromagnetic order [54]. The unambiguous microscopic evidence of the magnetic ground state nature is still missing, although some preliminary results of neutron diffraction led to the observation of magnetic peak described by the $(\frac{1}{2}\ \frac{1}{2}\ 0)$ propagation vector [55].

Despite numerous studies on $CeCuAl_3$, some of its basic properties remain unclear, including still some ambiguity concerning its crystal structure, which is a fundamental point when discussing some of its electronic properties. The stoichiometric $CeTX_3$ compounds with $X=$ Si or Ge crystallize in the $BaNiSn_3$-type structure which is the ordered non-centrosymmetric variant of the $BaAl_4$ tetragonal structure. However, for compounds with $X=$ Ga or Al also the disordered variants $BaAl_4$ or $ThCr_2Si_2$ structures are often considered. $CeCuAl_3$ was first reported to crystallize in the $ThCr_2Si_2$-type structure [56] with Cu and one-third of the Al atoms randomly distributed over the 2(a)-positions of this structure. This conclusion was adopted and confirmed by several later studies [53, 51], some papers mentioned also the $BaAl_4$ structure without deeper analysis [50]. Contrary to these earlier studies, the ordered $BaNiSn_3$-type structure was concluded from the powder neutron diffraction data [57]. This is rather reliable result as the neutron scattering length for Ce is much smaller than for Cu (and comparable with Al) atoms, which allows for a more accurate Cu/Al site occupation assignment compared to powder X-ray diffraction, where the Ce contribution dominates.

Subsequently many further papers adopted the $BaNiSn_3$ structure [45, 52, 4]. On the other hand, some recent studies stated again the $BaAl_4$ structure [58]. All the previous structural studies were based on polycrystalline data.

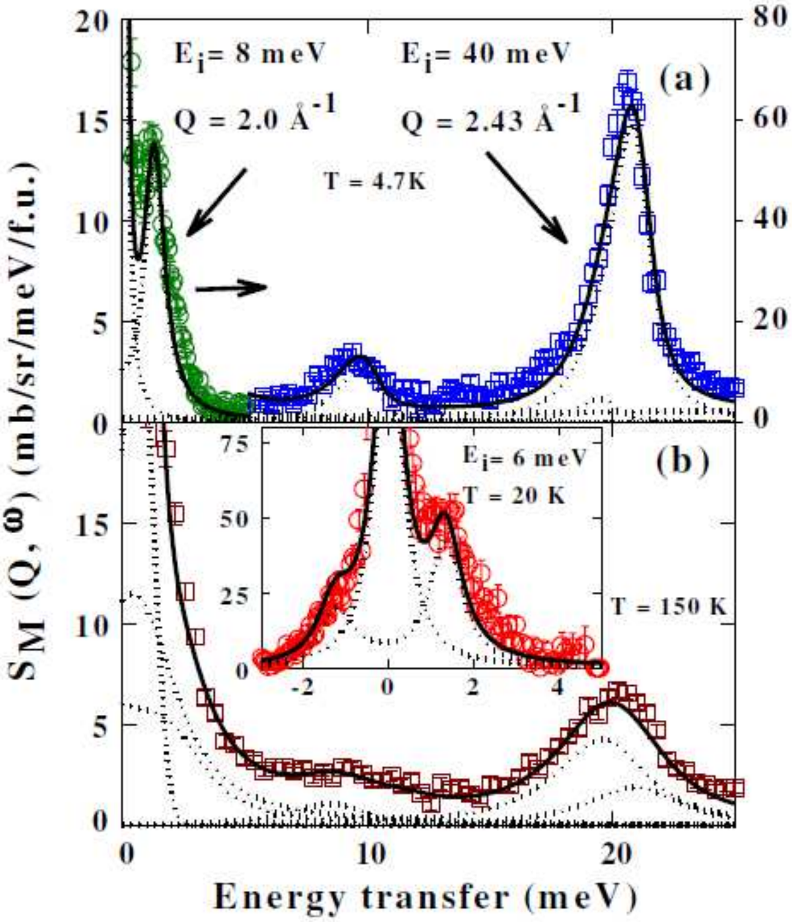

Figure 3.2: The 'magnetic' energy spectrum of $CeCuAl_3$ as measured by Adroja et al. [4]. The CF-like peaks are clearly observed. Panel a) contains the measurements at 4.7 K (low-energy data (green circles) are scaled along right vertical axis, whereas higher energy data (blue squares) belong to left vertical axis), panel b) contains the measurement at 150 K and the inset the data measured at 20 K.

Similarly to the case of $CeAl_2$ [29], CF exciton-phonons interaction leads to the formation of new quasi-bound states in $CeCuAl_3$. One would expect to observe two CF peaks corresponding to energies of transitions from doublet ground state to first and second excited doublets. Instead, three peaks at 1.3, 9.8 and 20.5 meV are clearly observed, see Figure 3.2. The presence of the additional peak could be understood as the strong CF exciton-phonons coupling takes place in the compound. The schematic energy levels splitting is presented in Figure 3.3 (compare with Figure 1.2). On the contrary to cubic $CeAl_2$, where the excited quartet was splitted by phonons into (very roughly speaking) two doublets, in tetragonal $CeCuAl_3$, Kramer's doublets are expected already due to pure CF effect. One might suppose, that the high energy doublet splits into two singlets because of the influence of lattice vibrations. On the other hand, it is believed, that the effective degeneracy of all excited states is still 2-folded [4, 59], as there

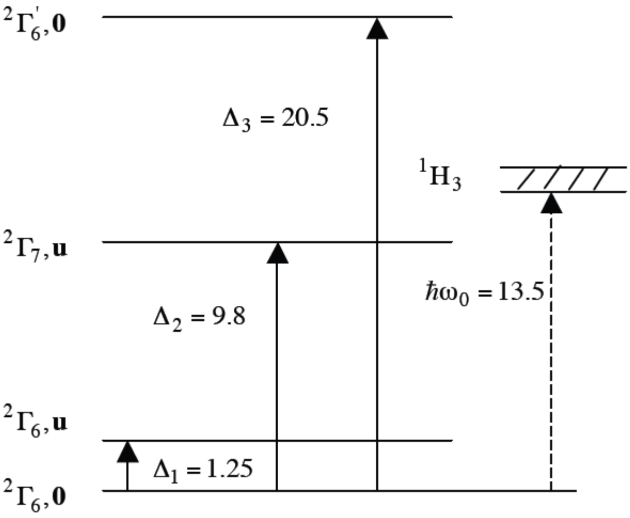

Figure 3.3: The schema of energy levels splitting in $CeCuAl_3$ [4, 59]. The energies are listed in units of meV. Compare with Figures 1.2 and 3.1.

is no reason to break time-reversal symmetry of the system.

The measured spectrum of $CeCuAl_3$ was described by Hamiltonian containing not only pure CF part (see formula 1.7), but also phonon part and CF exciton-phonons interaction term [4]:

$$\widehat{H}_{\text{tot}} = \sum_{mn} B_m^n \widehat{O}_m^n + \hbar\omega_0(a_\mu^+ a_\mu + \frac{1}{2}) - g_0 \sum_\mu (a_\mu + a_\mu^+)\widehat{O}_\mu. \tag{3.2}$$

A proper data analysis led to the following parameters [4]: $B_2^0 = 0.611(17)$ meV, $B_4^0 =$ -0.015(1) meV, $|B_4^4| = 0.317(4)$ meV, $\hbar\omega_0 = 11.3(5)$ meV and magneto-elastic parameter $g_0 = 0.40(3)$ meV/Ce^{3+}.

Here, we should also mention the results of inelastic neutron scattering measurement and subsequent analysis on $CePd_2Al_2$ compound done by Chapon et al. [3]. $CePd_2Al_2$ belongs among Ce-based compounds crystallizing in tetragonal $CaBe_2Ge_2$-type structure [3], another derivative of parent $BaAl_4$ (similarly as $BaNiSn_3$-type structure for $CeCuAl_3$, see discussion in next chapter and Figure 4.1). The structural phase transition from tetragonal to orthorhombic structure at around 13.5 K was observed. The last information, which is known about $CePd_2Al_2$, is the energy spectrum at 20 K containing three CF-like peaks instead of two expected [3]. The analysis of energy spectrum was done in the similar way as for $CeCuAl_3$, nevertheless, the description of whole data treatment is given in rather short manner (despite the fact, that the study of $CePd_2Al_2$ preceded to the one of $CeCuAl_3$ [4]) [3]. The following parameters were obtained from Hamiltonian 3.2 [3]: $B_2^0 = 0.60(2)$ meV, $B_4^0 = 0.0302(3)$ meV, $|B_4^4| = 0.027(2)$ meV and $g_0 = 1.41(3)$ meV/Ce^{3+}.

The study of energy spectra and vibron states in $CeCuAl_3$ and $CePd_2Al_2$ and the relation between microscopic and macroscopic properties of these compounds represent the main goal of the thesis. We investigated the crystal structures, electronic properties and magnetic structures of these compounds using a variety of experimental techniques including the neutron scattering experiments.

Together with a detailed investigation of a $CeCuAl_3$ single crystal, we studied also several substituted systems to obtain a broader picture of the microscopic nature of $CeCuAl_3$ and its changes with the doping. The isostructural $Ce(Cu,Al)_4$, $Ce(Cu,Au)Al_3$ and $CeCu(Al,Ga)_3$ series were investigated in course of Ph.D. work. The results of structural and bulk magnetic properties of the latter two series are summarized in our papers [60, 61] and are not included in the text of the thesis to keep its reasonable length. Here we focus on the $Ce(Cu,Al)_4$ series, in which the crystal field excitations and possible vibron states were investigated by inelastic neutron scattering.

$CePd_2Al_2$ single crystal and whole $CePd_2(Al,Ga)_2$ series were also closely studied. Most of the results of bulk measurements and X-ray diffraction on single crystal as well as the pressure experiments on studied compounds are described in details in master thesis of Petr Doležal, who collaborated in this subject [62], and our papers [63, 64]. During our systematic investigation of $CePd_2Al_{2-x}Ga_x$ and $LaPd_2Al_{2-x}Ga_x$ compounds, the superconductivity of lanthanum compounds was found in the whole series. The superconductivity in this series cannot be discussed purely in terms of BCS theory as there is a significant deviation from the expected behavior. The details on the superconductivity in $LaPd_2(Al,Ga)_2$ are given in our paper [65]. Again, the above mentioned subjects are not included in the text of this thesis to keep its reasonable length and not to overlap with other student theses. Here we focus on the crystal field and vibron state development in $CePd_2(Al,Ga)_2$ and a possible connection to the structural phase transition in these compounds.

4. Results and discussion

4.1 CeCuAl$_3$ and CeTX_3 compounds

The Ce-based intermetallic CeTX_3 compounds, where T is a transition element d-metal and X is a p-metal, have been intensively investigated in last years for their exotic properties, especially at low temperatures. The electronic properties of CeTX_3 compounds are strongly dependent on competition between long-range RKKY interaction and Kondo interaction. The influence of crystal electric field plays also an important role. The ground states and phenomena in these compounds are strongly influenced by chemical composition and/or external pressure, see previous section 3.2. The magnetic structure was determined for only several CeTX_3 compounds so far, due to often small magnetic moment and low ordering temperature. Also the investigation of crystal structure is not always straightforward as Ce contribution to diffraction patterns dominates, while T and X elements contribute with a similar strength (at least in the case of powder X-ray diffraction).

4.1.1 Crystal structure in CeTX_3 compounds

CeTX_3, or more generally Ce$(T,X)_4$, compounds crystallize frequently in the tetragonal structure of BaAl$_4$-type and its derivates. Table 4.1 summarizes the crystal structure parameters of previously investigated CeTX_3 compounds. Several compounds from CeTX_3 family adopt a cubic structure, e.g. CeRuSn$_3$ [66] or CeRhSn$_3$ [67]. CeRuGe$_3$ [68], CeNiGe$_3$ [69] and CeAgAl$_3$ [70] crystallize in orthorhombic structure. The orthorhombic structure was reported also for CePdGa$_3$ [71] and CePtGa$_3$ [72], however this Fmm2 structure is very similar to parent BaAl$_4$ structure: the lattice parameters a_{orth} and b_{orth} differ subtle only, while a-axis is identical with the diagonal of BaAl$_4$-type structure, i.e. $a_{\mathrm{tetr}} = \frac{a_{\mathrm{orth}}}{\sqrt{2}} \approx 4.31$ Å for these compounds (see Table 4.1). We stress out the case of CeTAl$_3$ compounds with T = Cu, Ag and Au. The isoelectronic substitution of d-metal element (i.e. the change of lattice parameters) causes inter alia the change of crystal structure from tetragonal for CeCuAl$_3$ to orthorhombic for CeAgAl$_3$ [70] and back to tetragonal for CeAuAl$_3$ [73]. Also the magnetic structure in CeAgAl$_3$ was reported to be ferromagnetic [42], whereas other two compounds exhibit antiferromagnetic ground state [51, 40]. Such an observation documents an important role of chemical composition on the physical properties in CeTX_3 compounds.

The tetragonal centrosymmetric BaAl$_4$-type structure (I4/mmm, 139) and its derivates, centrosymmetric ThCr$_2$Si$_2$ (I4/mmm, 139), ordered primitive CaBe$_2$Ge$_2$ (P4/nmm, 129) and ordered non-centrosymmetric BaNiSn$_3$ (I4mm, 107) structures, differ from each other by different stacking of d- and p-metal element planes (of CeTX_3 compounds) along the tetragonal c-axis, while the Ce atomic positions remain the same. All mentioned structure types are shown in Figure 4.1. In BaAl$_4$-type, T and X atoms are randomly distributed over the 2(a) and 4(b) sites, leading to centrosymmetric structure. In the ThCr$_2$Si$_2$-type, the random distribution remains on the 2(a) positions, whereas the 4(b) sites are occupied

Table 4.1: The crystal structure types and lattice parameters of previously studied CeTX_3 compounds. The c/a ratio and volume of fundamental unit cell, V, are listed as well. The lattice parameters of $\mathrm{CeCuAl_3}$ (*) were determined during our recent investigation of single crystal (see following section and Ref. [74]).

Compound	Structure type	a (Å)	b (Å)	c (Å)	c/a	V (Å^3)	Ref.
$\mathrm{CeFeGe_3}$	$\mathrm{BaNiSn_3}$	4.3320		9.9550	2.2980	186.8178	[75]
$\mathrm{CeRuSi_3}$	$\mathrm{BaNiSn_3}$	4.2070		9.9260	2.3594	175.6788	[76]
$\mathrm{CeRuGe_3}$	Cmmm	21.850	4.234	4.285		396.4178	[68]
$\mathrm{CeRuSn_3}$	Pm$\bar{3}$n	9.726				920.03	[66]
$\mathrm{CeRhSn_3}$	Pm$\bar{3}$n	9.7115				915.92	[67]
$\mathrm{CeCoSi_3}$	$\mathrm{BaNiSn_3}$	4.1350		9.5670	2.3137	163.5787	[77]
$\mathrm{CeCoGe_3}$	$\mathrm{BaNiSn_3}$	4.3204		9.8348	2.2764	183.5750	[41]
$\mathrm{CeRhSi_3}$	$\mathrm{BaNiSn_3}$	4.2690		9.7380	2.2811	177.4688	[78]
$\mathrm{CeRhGe_3}$	$\mathrm{BaNiSn_3}$	4.3960		10.0224	2.2799	193.6810	[39]
$\mathrm{CeIrSi_3}$	$\mathrm{BaNiSn_3}$	4.2520		9.7150	2.2848	175.6424	[79]
$\mathrm{CeIrGe_3}$	$\mathrm{BaNiSn_3}$	4.4010		10.0240	2.2777	194.1529	[80]
$\mathrm{CeNiGa_3}$	$\mathrm{ThCr_2Si_2}$	4.25		10.24	2.4094	184.96	[81]
$\mathrm{CeNiGe_3}$	Cmma	4.1391	21.828	4.1723		376.9601	[69]
$\mathrm{CePdAl_3}$	$\mathrm{BaNiSn_3}$	4.3435		10.9536	2.5218	206.6486	[70]
$\mathrm{CePdGa_3}$	Fmm2	6.1036	6.1624	10.3971		419.6212	[71]
$\mathrm{CePdSi_3}$	$\mathrm{BaNiSn_3}$	4.3300		9.6310	2.2242	180.5707	[82]
$\mathrm{CePdSb_3}$	$\mathrm{CaBe_2Ge_2}$	4.482		9.860	2.1999	198.0709	[81]
$\mathrm{CePtAl_3}$	$\mathrm{BaNiSn_3}$	4.3239		10.6670	2.4670	199.4314	[70]
$\mathrm{CePtAl_3}$	$\mathrm{BaAl_4}$	4.311		10.668	2.4746	198.2618	[45]
$\mathrm{CePtGa_3}$	Fmm2	6.100	6.113	10.512		391.99	[72]
$\mathrm{CePtSi_3}$	$\mathrm{BaNiSn_3}$	4.3215		9.6075	2.2232	179.4235	[83]
$\mathrm{CeCuAl_3}$	$\mathrm{BaNiSn_3}$	4.2620		10.6806	2.5060	194.0093	[74]*
$\mathrm{CeCuGa_3}$	$\mathrm{BaNiSn_3}$	4.2450		10.4200	2.4547	187.7687	[46]
$\mathrm{CeCuGa_3}$	$\mathrm{BaAl_4}$	4.2729		10.4359	2.4423	190.5353	[43]
$\mathrm{CeAgAl_3}$	Cmcm	6.2101	6.1186	10.8691		412.9950	[70]
$\mathrm{CeAuAl_3}$	$\mathrm{BaNiSn_3}$	4.3660		10.8445	2.4839	206.7174	[84]
$\mathrm{CeAuGa_3}$	$\mathrm{BaNiSn_3}$	4.337		10.660	2.4579	200.510	[45]

exclusively by X element. Both structures are clearly centrosymmetric. The non-centrosymmetric $\mathrm{BaNiSn_3}$ is completely ordered structure type with following atomic coordinates:

2Ce in 2(a): $(0,\ 0,\ z_{\mathrm{Ce}}), (\frac{1}{2}, \frac{1}{2}, \frac{1}{2} + z_{\mathrm{Ce}})$
$2T$ in 2(a): $(0,\ 0,\ z_T), (\frac{1}{2}, \frac{1}{2}, \frac{1}{2} + z_T)$
$2X$ in 2(a): $(0,\ 0,\ z_{X_{\mathrm{a}}}), (\frac{1}{2}, \frac{1}{2}, \frac{1}{2} + z_{X_{\mathrm{a}}})$
$4X$ in 4(b): $(0,\ \frac{1}{2}, z_{X_{\mathrm{b}}}), (\frac{1}{2}, 0, z_{X_{\mathrm{b}}}), (\frac{1}{2}, 1, \frac{1}{2} + z_{X_{\mathrm{b}}}), (1, \frac{1}{2}, \frac{1}{2} + z_{X_{\mathrm{b}}})$,

where $z_{\dots}$ represents the shift along the c-axis, while $z_{\mathrm{Ce}} \approx 0$ and $z_{X_{\mathrm{b}}} \approx 0.25$. The case of $\mathrm{CaBe_2Ge_2}$-type structure is slightly different as the mutual stacking of layers along the tetragonal axis leads to ordered centrosymmetric structure with primitive unit cell. Figure of primitive unit cell will be shown in following section 4.2 together with the study of $CePd_2Al_2$ compound. $CaBe_2Ge_2$-type structure has two possible origins shifted by $(\frac{1}{4}, -\frac{1}{4}, 0)$ to each other. The unit cell with the origin 1 described by atomic coordinates:

2Ce in 2(c): $(0,\, \frac{1}{2}, z_{\mathrm{Ce}}), (\frac{1}{2}, 0, -z_{\mathrm{Ce}})$
$2T$ in 2(a): $(0,\, 0,\, 0),\, (\frac{1}{2}, \frac{1}{2}, 0)$
$2T$ in 2(c): $(0,\, \frac{1}{2}, z_{T_{\mathrm{c}}}), (\frac{1}{2}, 0, -z_{T_{\mathrm{c}}})$
$2X$ in 2(b): $(0,\, 0,\, \frac{1}{2}), \frac{1}{2}, \frac{1}{2}, \frac{1}{2})$
$2X$ in 2(c): $(0,\, \frac{1}{2}, z_{X_{\mathrm{c}}}), (\frac{1}{2}, 0, -z_{X_{\mathrm{c}}})$

could be shown in the same way as other $BaAl_4$ derivates by shifting the atomic positions by $(\frac{1}{2}, 0, -z_{\mathrm{Ce}})$. Alternatively, the structure with origin 2 with atomic positions shifted by $(\frac{1}{4}, \frac{1}{4}, z_{\mathrm{Ce}})$ would lead to the same representation. The elementary cell of $CaBe_2Ge_2$-type structure shown in Figure 4.1 is thus not the primitive unit cell.

4.1.2 Crystal structure of $CeCuAl_3$

Crystal structure determination on $CeCuAl_3$ single crystal

Several tetragonal crystal structures were suggested for $CeCuAl_3$ by pollycrystalline studies [56, 53, 51, 50, 57, 45, 52, 4, 58], as introduced in section 3.2. Nevertheless, the determination of crystal structure type based on powder X-ray diffraction is very complicated as Ce atoms contribute significantly stronger to diffraction patterns than Cu and Al (which contribute similarly due to similar number of electrons). To distinguish between structure types shown in Figure 4.1, the precise method allowing observation of Cu and Al atoms in given atomic positions is needed. The diffraction experiment on single crystal employing a four-circle goniometer is one of the methods allowing a correct determination of crystal structure type.

The preparation of $CeCuAl_3$ single crystal and its structural and chemical characterization is described in sections 2.1 and 2.2: the single crystal was prepared from polycrystalline precursor using the Czochralski growing method. Prepared polycrystalline sample was annealed for 8 days at 900°C in quartz tube, the rate of heating the sample from room temperature was 3°C per minute, the rate of cooling down from 900°C was 1°C per minute. The single crystal was first investigated in its as-cast form and subsequently it has been annealed in the same way as polycrystalline sample.

The prepared ingot (Figure 2.1) was investigated by means of Laue X-ray and neutron diffraction verifying the quality and tetragonal symmetry of the sample (see Figure 2.4). The powder X-ray diffraction on powderized part of single crystal recorded at room temperature confirms that this compound crystallizes in the tetragonal structure. The best fit of the diffraction pattern was obtained for the $BaNiSn_3$-type structure ($R_{\mathrm{Bragg}} = 6.9\%$ compared to $R_{\mathrm{Bragg}} = 31.3\%$ for the $ThCr_2Si_2$-type). Introducing certain degree of Cu-Al disorder to the $BaNiSn_3$ structure did not lead to any improvement of the fit. We examined closely also the diffraction patterns of polycrystalline sample with similar result. These results, pointing to the $BaNiSn_3$ structure, are well consistent with the neutron diffraction

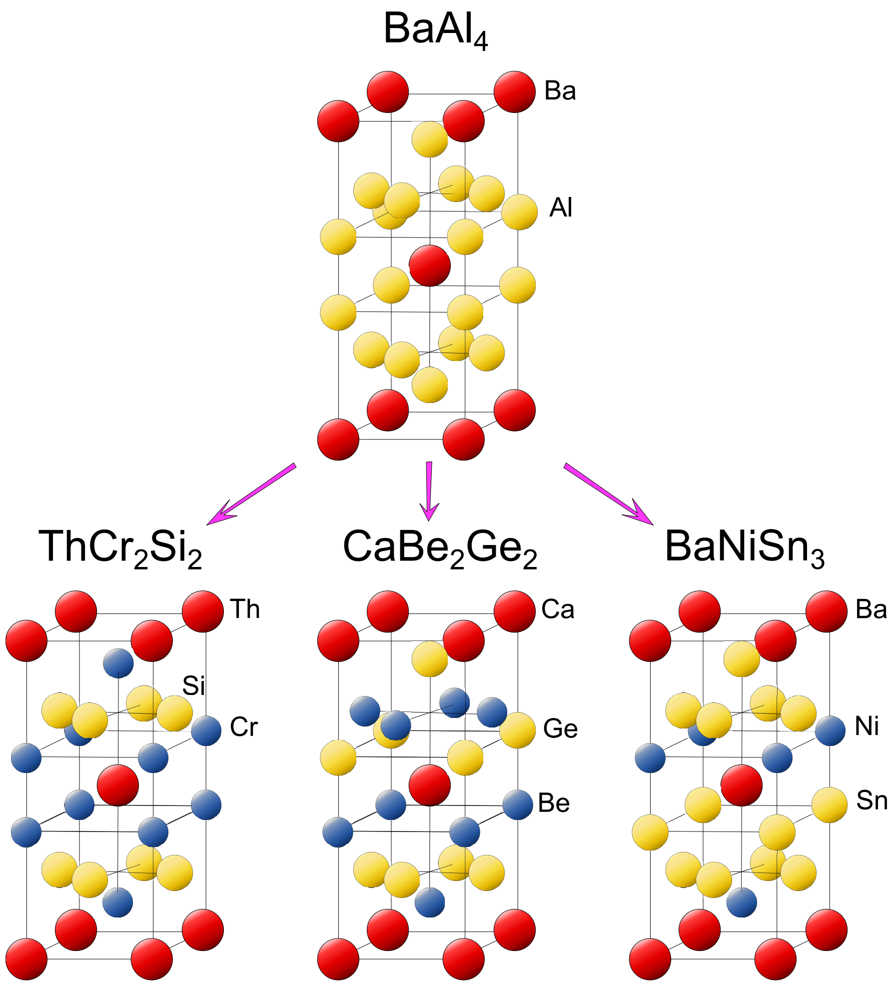

Figure 4.1: The tetragonal structure types: centrosymmetric $BaAl_4$ (I4/mmm, 139) and three its derivatives - centrosymmetric $ThCr_2Si_2$ (I4/mmm, 139), ordered primitive $CaBe_2Ge_2$ (P4/nmm, 129) and ordered non-centrosymmetric $BaNiSn_3$ (I4mm, 107) structure. $CaBe_2Ge_2$-type structure has two possible origins shifted by $(\frac{1}{4}, -\frac{1}{4}, 0)$ to each other; presented figure was drawn taking the origin 1 shifted by $(\frac{1}{2}, 0, -z_{\mathrm{Ce}})$ or alternatively origin 2 shifted by $(\frac{1}{4}, \frac{1}{4}, z_{\mathrm{Ce}})$, i.e. the primitive unit cell is not shown, for better lucidity.

data [57]. However, we should have in mind somewhat limited sensitivity of powder X-ray diffraction to Cu and Al positions and Cu-Al disorder.

The crystal structure was then uniquely determined by single crystal X-ray diffraction (295 independent reflections, $R_{\mathrm{int}} = 0.0169$) as tetragonal $BaNiSn_3$-type structure (space group I4mm, 107) without any sign of disorder in Cu and Al atomic positions. We should note, that the best structure solution was obtained when a racemic-twinning has been introduced. It seems that there exists two equally populated domains which are connected by a mirroring, where the mirror plane is perpendicular to the four-fold axis. The refined structure parameters at room temperature and at 150 K are summarized in Table 4.2. The thermal displacements of atoms are listed in Table 4.2 as well.

The chemical composition investigation of our $CeCuAl_3$ single crystal as well as polycrystalline sample was done employing the EDX analysis. The analysis confirms the stochiometric composition Ce:Cu:Al = 1:1:3 (with up to 0.03 error

Table 4.2: Structure parameters of $\mathrm{CeCuAl_3}$ single crystal determined from X-ray diffraction patterns taken at 150 K and at room temperature. $V_{\mathrm{f.u.}}$ is the volume per fundamental unit cell. z_{Ce}, z_{Cu}, $z_{\mathrm{Al_a}}$ and $z_{\mathrm{Al_b}}$ are fraction coordinates of atoms in the unit cell (see previous subsection 4.1.1). R is the agreement factor for the fit of diffraction patterns (goodness of fit on F^2). The thermal displacements of atoms are described by: $-2\pi^2(h^2a^{*2}\mathrm{U}_{11} + ... + 2hka^*b^*\mathrm{U}_{12})$, where matrix elements U_{12}, U_{13} and U_{23} are equal to zero. SHELXS-97 program employing the Rietveld analysis was used for the determination of structure parameters.

T (K)	150	296
a (pm)	425.27(3)	426.20(2)
c (pm)	1066.80(7)	1068.06(5)
c/a	2.5085(2)	2.5060(2)
$V_{\mathrm{f.u.}}$ ($10^6\mathrm{pm}^3$)	96.47(2)	97.01(2)
atomic positions:		
2Ce in 2(a)	$(0, 0, 0_{\mathrm{fix}})$	$(0, 0, 0_{\mathrm{fix}})$
2Cu in 2(a)	(0, 0, 0.0946(3))	(0, 0, 0.0942(2))
2Al in 2(a)	(0, 0, 0.3689(1))	(0, 0, 0.36909(8))
4Al in 4(b)	$(0, \frac{1}{2}, 0.2508(2))$	$(0, \frac{1}{2}, 0.2505(2))$
thermal displacement:		
U_{11} (Ce)	0.0032(2)	0.00490(7)
U_{22} (Ce)	0.0032(2)	0.00490(7)
U_{33} (Ce)	0.0041(2)	0.0069(1)
U_{11} (Cu)	0.0068(4)	0.0097(2)
U_{22} (Cu)	0.0068(4)	0.0097(2)
U_{33} (Cu)	0.0093(7)	0.0108(3)
U_{11} (Al)	0.006(1)	0.0086(9)
U_{22} (Al)	0.006(1)	0.0095(9)
U_{33} (Al)	0.0061(5)	0.0092(3)
U_{11} ($\mathrm{Al_b}$)	0.0056(8)	0.0077(4)
U_{22} ($\mathrm{Al_b}$)	0.0056(8)	0.0077(4)
U_{33} ($\mathrm{Al_b}$)	0.011(2)	0.0128(9)
R (%)	2.36	1.12

of analysis). The distribution of elements in sample was also checked by EDX equipment, homogeneous distribution of elements can be seen in Figure 2.3.

Structural phase transition in $\mathrm{CeCuAl_3}$

Some properties of $\mathrm{CeCuAl_3}$ are slightly influenced by sample thermal treatment [51]. These changes can be ascribed to the annealing process which generally improves the quality of the sample, i.e. reduces the residual resistivity and also improves the thermal properties of the sample. To optimize the sample thermal treatment, the knowledge of the phase diagram and mainly the melting temperature is essential. We have performed DSC measurement to reveal the melting temperature. Surprisingly, we have observed a further phase transition in course of these measurements.

The DSC temperature scans revealed the melting temperature of 1275°C (see inset of Figure 4.2) which justifies the optimal annealing temperature around 900°C. Additionally, the measured scans, presented in Figure 4.2, show a clear λ-peak between 279°C and 335°C which corresponds to the structural phase transition in the sample. The transition temperature of 320°C was obtained in usual way for this type of transition, i.e. as the temperature where the heating peak has minimum. This anomaly is observed also for cooling and is reproduced in all measurements independently on maximal temperature (500°C - 900°C) of the scan, even not by achieving the melting temperature. The change of enthalpy associated with this transition is higher for heating (1.353 J.g^{-1}) than for cooling (0.959 J.g^{-1}) what might suggest a certain change of structure after the heating-cooling cycle. Further, DSC measurement on annealed and polycrystalline sample showed the same behavior. The lanthanum analogue $LaCuAl_3$ exhibits signs of similar anomaly during the heating cycle, nevertheless much weaker as shown in Figure 4.2. The enthalpy corresponding to this phase transition reaches only 0.153 J.g^{-1}, nearly 10 times smaller value than for $CeCuAl_3$. No anomaly is observed during the cooling process in $LaCuAl_3$. The same behavior was reproduced by second subsequent cycle on the same $LaCuAl_3$ sample.

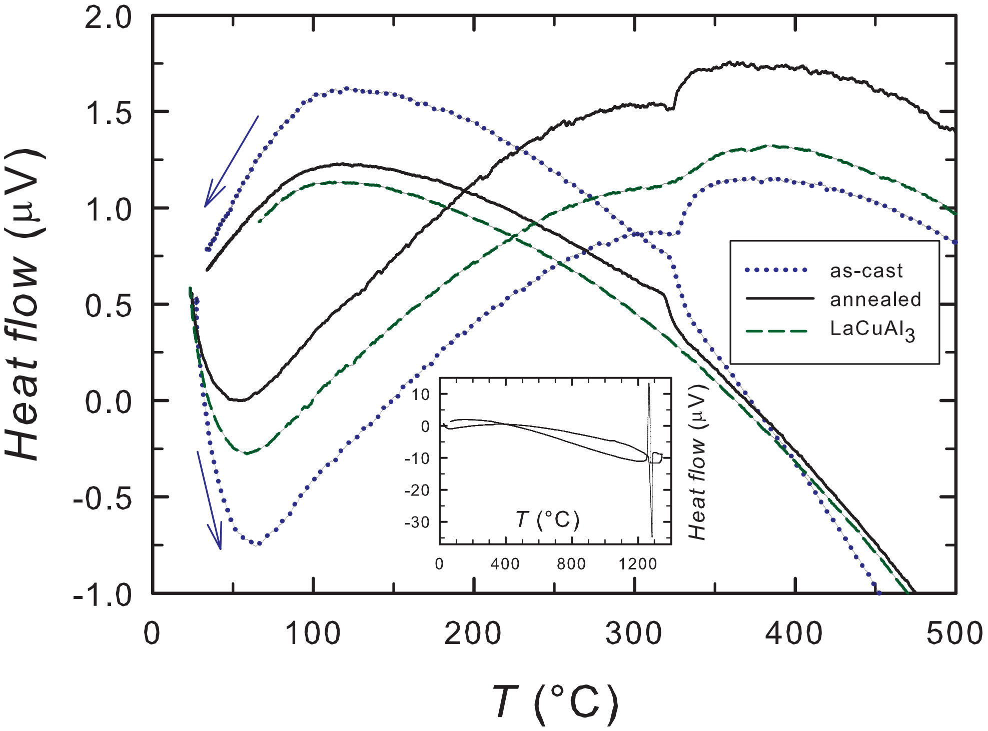

Figure 4.2: Differencial scanning calorimetry performed on as-cast and annealed $CeCuAl_3$ single crystal as well as on polycrystalline $LaCuAl_3$. Heating/cooling rate was 10°C per minute. The inset shows data for annealed single crystal up to melting temperature.

The high-temperature powder X-ray diffraction experiment was performed on as-cast and annealed $CeCuAl_3$ single crystal, as well as on annealed polycrystalline $CeCuAl_3$ and $LaCuAl_3$ samples to reveal the microscopic origin of the anomaly observed by DSC measurement. Results of the refinement of diffraction

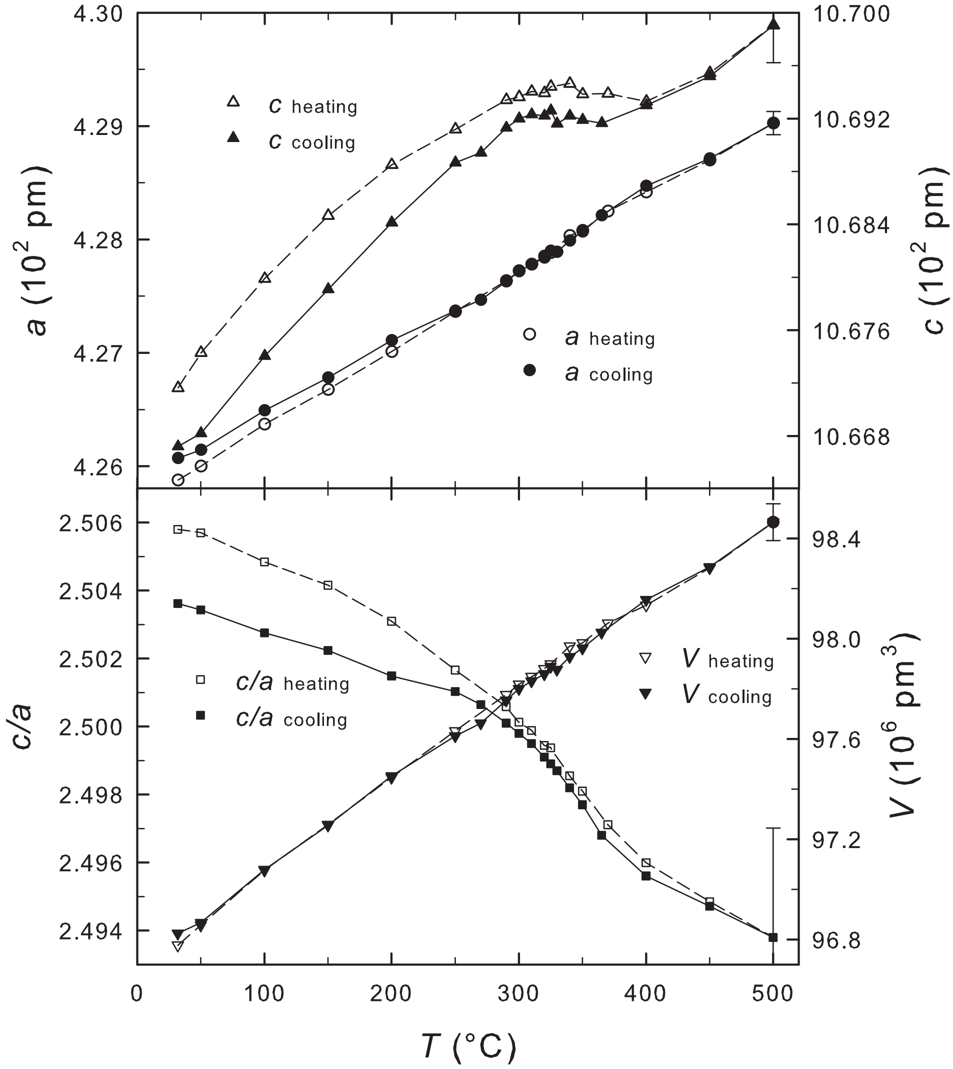

Figure 4.3: The lattice parameters of the annealed single crystal $\mathrm{CeCuAl_3}$ obtained by high-temperature X-ray diffraction. The error for each lattice parameter is almost constant during the heating/cooling process, for this reason and for better lucidity we show error bars only for the value at 500°C (highest error). The agreement factor of the fit of our model to the experimental data was almost the same ($R_{\mathrm{Bragg}} \approx 6.9\%$) for all measurements.

patterns using the Fullprof program [11] are presented in Figures 4.3 and 4.4. Linear increase of lattice parameters with increasing temperature is observed up to 250°C, the usual effect of thermal expansion takes place. The atomic fraction coordinates, i.e. z_{Cu} and $z_{\mathrm{Al_a}}$, are unaffected up to 250°C. The transition seen in DSC is then reflected by anomalous development of the c parameter (or c/a ratio) around 300°C. The lattice parameters increase again linearly above ≈ 350°C which suggests a stable high-temperature phase, in agreement with DSC analysis. The measurement during the cooling to room temperature shows very similar development of lattice parameters but the transition from high-temperature to low-temperature phase does not lead to the original values of lattice parameters, see Figure 4.3. The lattice parameter a has higher value and parameter c

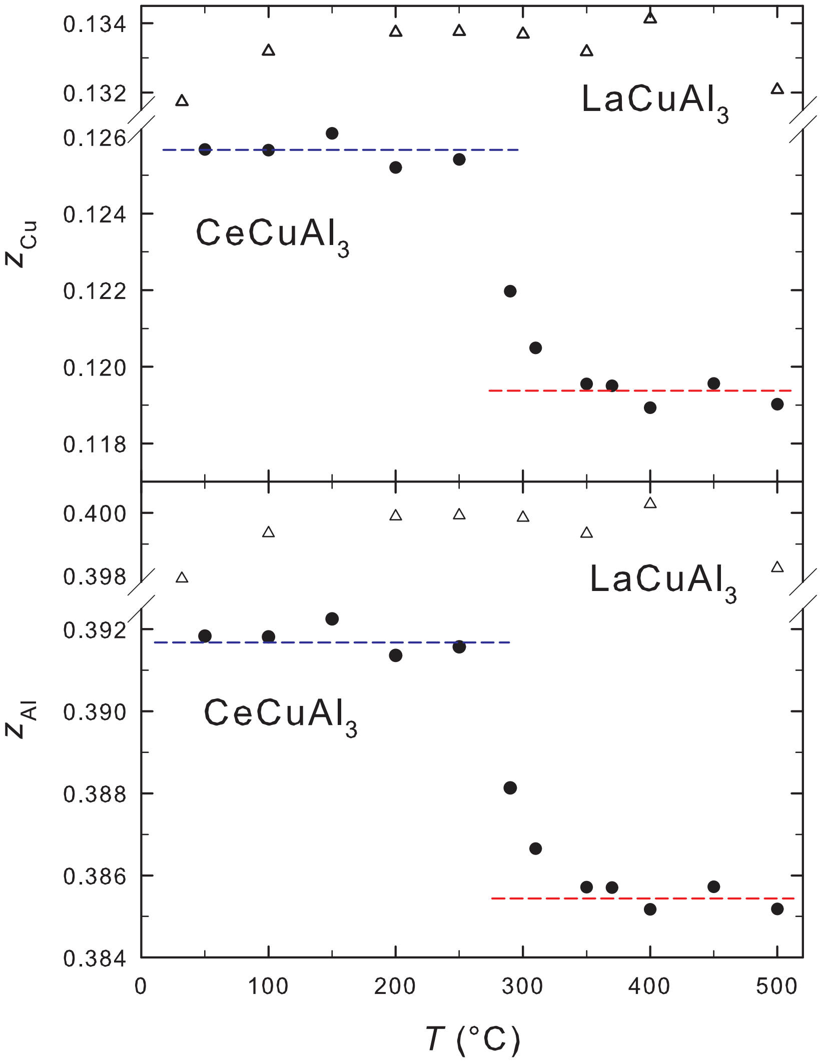

Figure 4.4: The atomic fraction coordinates of annealed single crystal CeCuAl$_3$ and LaCuAl$_3$ polycrystal obtained by high-temperature X-ray diffraction. The error of determination of atomic positions is $\approx 6.10^{-3}$. The lines are to guide the eye.

has lower value compared to initial ones before the heating/cooling cycle. The change can be expressed as $\cong 0.05$ % of their initial values. Although the lattice parameters in CeCuAl$_3$ are different after heating/cooling cycle, the volume of fundamental unit cell stays almost unaffected because the parameters a and c change in opposite way.

The transition around $\approx 300^{o}$C is more visible in development of atomic fraction coordinates z_{Cu} and $z_{\mathrm{Al_a}}$ plotted in Figure 4.4. The difference between these coordinates at temperatures below and above 300^{o}C is $\approx 6.10^{-3}$ what represents almost 2% change of the value of these coordinates (see also illustrative picture of changed atomic coordinates in Figure 4.5 and changes of interatomic distances given in Table 4.3). We are aware that the numerical error of determination of these values is also approximately 6.10^{-3}. Furthermore, the uncertainty of determination of atomic positions from powder diffraction data is higher than only numerical error. In powder diffraction patterns, we face the problem of overlapping of the diffraction lines which is not present when using the single crystal diffraction data. The overlapping can strongly affect, together with diffraction data quality, the accuracy of parameters of the structural model. The atomic positions determined using single crystal diffraction are much more accurate. The values obtained from powder diffraction are bounded with relatively high error and here serve mainly to follow qualitatively their temperature development. Despite relatively high error, the tendency, scatter of the values and mainly reproducibility of the effect on several samples are clear enough to conclude that the phase transition is present in $CeCuAl_3$.

Table 4.3: Interatomic distances in $CeCuAl_3$ obtained by employment of the Rietveld analysis at temperatures below and above structural phase transition. The patterns taken on powder sample were processed with Fullprof program [11]. The atomic positions are labelled as shown in previous subsection 4.1.1 and Figure 4.5.

T (°C)	Ce-Cu (pm)	Ce-Al$_\mathrm{a}$ (pm)	Ce-Al$_\mathrm{b}$ (pm)	Cu-Al$_\mathrm{a}$ (pm)	Cu-Al$_\mathrm{b}$ (pm)	Al$_\mathrm{a}$-Al$_\mathrm{b}$ (pm)
500	329.0(5)	326.9(6)	342.7(7)	250.1(6)	255.8(7)	258.9(6)
100	329.7(5)	322.4(7)	341.2(7)	250.8(6)	249.3(7)	261.2(6)

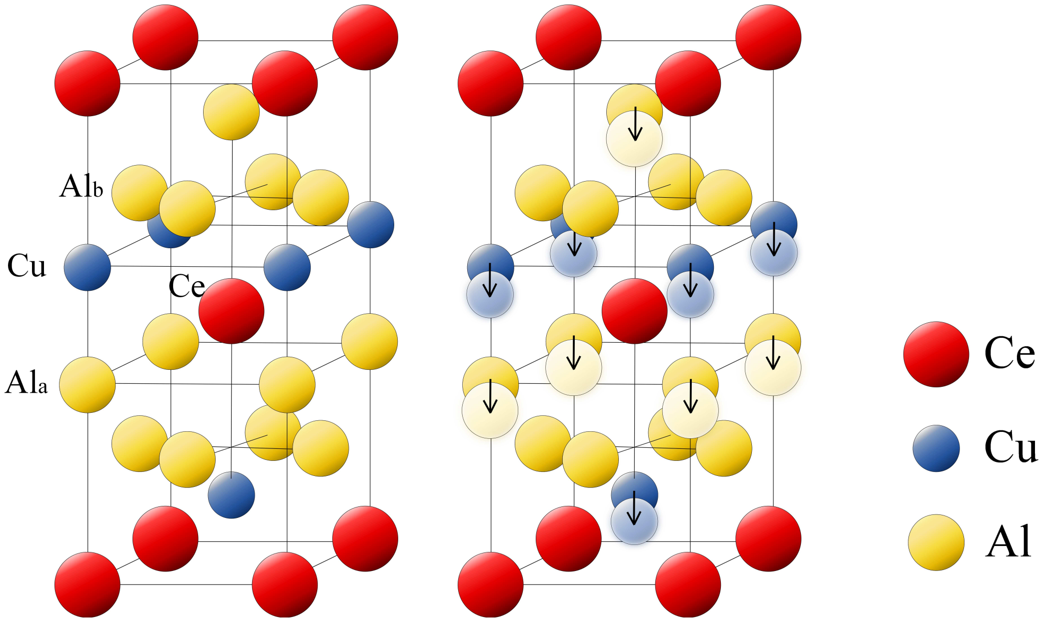

Figure 4.5: The $BaNiSn_3$-type structure adopted by $CeCuAl_3$ below 300°C. The atomic fraction coordinates are changed above 300°C as the smeared Cu and Al atoms with arrows denote. For better clarity, the shift is 10 times higher compared to the real change. The illustrative marking of atoms is done for easier understanding the Table 4.3.

The phase transition was observed for both, as-cast and annealed samples, as well as for polycrystalline sample, at the same temperature range, i.e. between 270°C and 340°C. The changes in structure parameters corresponding to this transition are very similar for all samples. Especially, similar changes in as-cast and annealed samples suggest that each heating/cooling cycle changes the structure parameters independently on maximal temperature, heating/cooling rate and duration of sample annealing.

The refinement of diffraction patterns of $LaCuAl_3$ polycrystal shows ordinary development of lattice parameters, i.e. linear increase with increasing temperature (from 4.295 to 4.325 $.10^2$ pm for parameter a and from 10.672 to 10.720 $.10^2$ pm for parameter c), without any trace of phase transition. The development of fraction coordinates z_{Cu} and $z_{\mathrm{Al_a}}$ of $LaCuAl_3$ is plotted in Figure 4.4. Also here, we are not able to see any clear hint of phase transition as seen in $CeCuAl_3$. If any such transition exists in $LaCuAl_3$, what might indicate the little anomaly in DCS measurements, it is below the experimental sensitivity of our powder X-ray diffraction analysis.

4.1.3 Bulk properties of $CeCuAl_3$ single crystal

The bulk properties of $CeCuAl_3$ have been investigated intensively by means of magnetization, specific heat and electrical resistivity measurements in last years [50, 51, 53, 45, 52, 54]. Nevertheless, the crystal structure of studied samples was often refined differently than by our recent study. We investigated bulk properties of our single crystal to verify previously reported results as well as to obtain reliable data on our single crystal for further neutron scattering studies.

Magnetization measurement

The antiferromagnetic order in $CeCuAl_3$ is indicated by a maximum in the temperature dependence of magnetization measured in low magnetic fields, see Figure 4.6. Clear sharp maximum at $T_{\mathrm{N}} \approx 2.5$ K appears when the magnetic field is applied within the basal plane (no significant differences between basal plane [100] and [110] directions were observed). The maximum is less pronounced and takes place at lower temperature of ≈ 2.4 K when the field is applied along the [001] direction. The difference between zero field-cooled (ZFC) and field-cooled (FC) regimes is rather small in measurements along all significant crystallographic directions (see Figure 4.6) and completely vanishes in the field of 0.05 T.

To bring further evidence of a long range magnetic order and to exclude some kind of spin-glass behavior, the ac-susceptibility measurements were performed. Figure 4.7 shows the temperature dependence of ac-susceptibility with phase transition at T_{N}, in agreement with the static magnetization. The measured dependencies are frequency independent, what points to a long-range magnetic order in $CeCuAl_3$.

The magnetization curves measured with field applied along principal crystallographic directions are plotted in Figure 4.8. We observe relatively strong anisotropy between the curves measured with field parallel and perpendicular to the tetragonal c-axis, in agreement with previously published data [54]. The larger saturation magnetization for field applied perpendicular to the c-axis reflects the fact that the moment of the ground state CEF level is larger for the

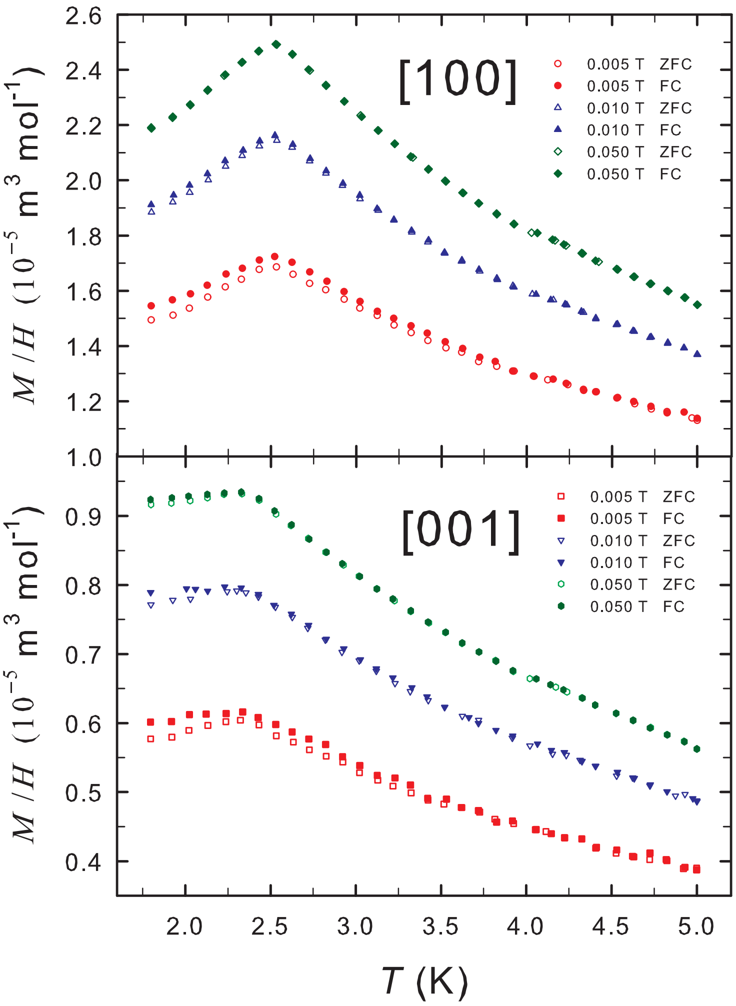

Figure 4.6: The temperature dependence of magnetization along significant crystallographic directions ([100] and [001]) in small magnetic fields. The measured curves overlap significantly, the shift of two of them (0.01 and 0.05 T) was done for better lucidity. ZFC means zero field-cooled and FC field-cooled regimes.

xy-component than for the z-component of magnetic moments. This does not imply necessarily, that the moments order in the basal plane.

In the paramagnetic region, the temperature dependence of M/H, shown in Figure 4.9, follows the Curie-Weiss law at least down to 60 K for measurement with $H \parallel [001]$ and even to much lower temperatures for field perpendicular to [001]. The fitting of measured data to relation 2.2 reveals the effective magnetic moment, μ_{eff}, in good agreement with theoretical value for Ce^{3+} ion, i.e. $\mu_{\mathrm{eff}} = 2.54\ \mu_{\mathrm{B}}$. The Curie paramagnetic temperature is then -52.0 K for $H \parallel [001]$, -6.2 K for $H \parallel [100]$ and - 4.7 K for $H \parallel [110]$ direction. Figure 4.9 shows also comparison of the measured $H/M(T)$ dependencies and calculated curves based on the CF parameters determined from the inelastic neutron scattering data [4]: $\mathrm{B}_2^0 = 0.611(17)$, $\mathrm{B}_4^0 = -0.015(1)$ and $|\mathrm{B}_4^4| = 0.317(4)$ meV (see section 3.2). The calculated dependencies are plotted in Figure 4.9 as lines of corresponding colors. Very good agreement of calculated and measured data is observed for $H \parallel [100]$, but clear discrepancy occurs for $H \parallel [001]$. The calculated

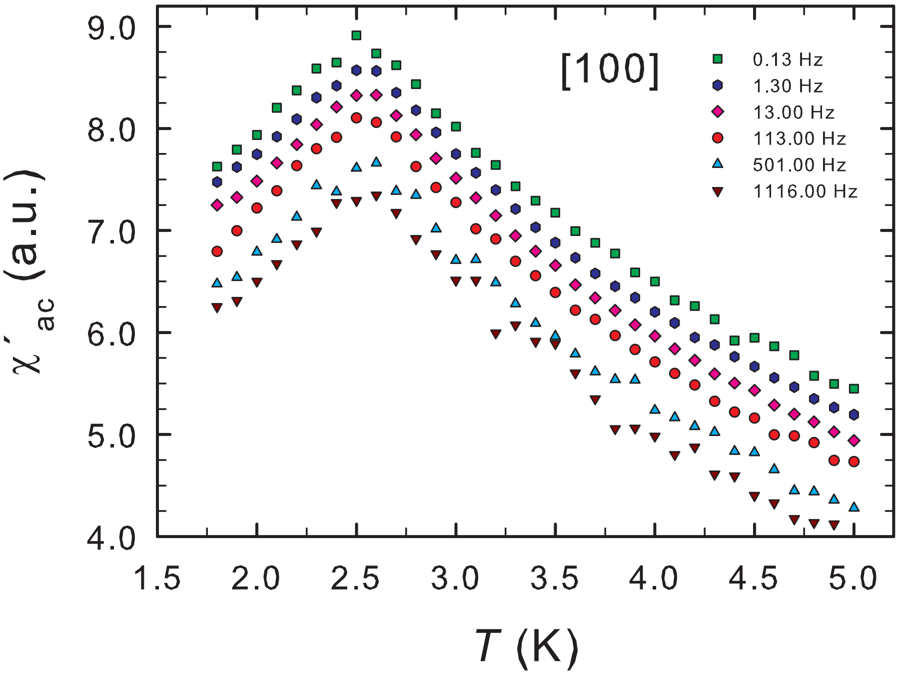

Figure 4.7: The real part of ac-susceptibility measured along [100] direction of $CeCuAl_3$ single crystal. The curves for all frequencies overlap, therefore each frequency curve is shifted by -0.2 from the previous one, for better lucidity. The curve for frequency of 0.13 Hz is not shifted.

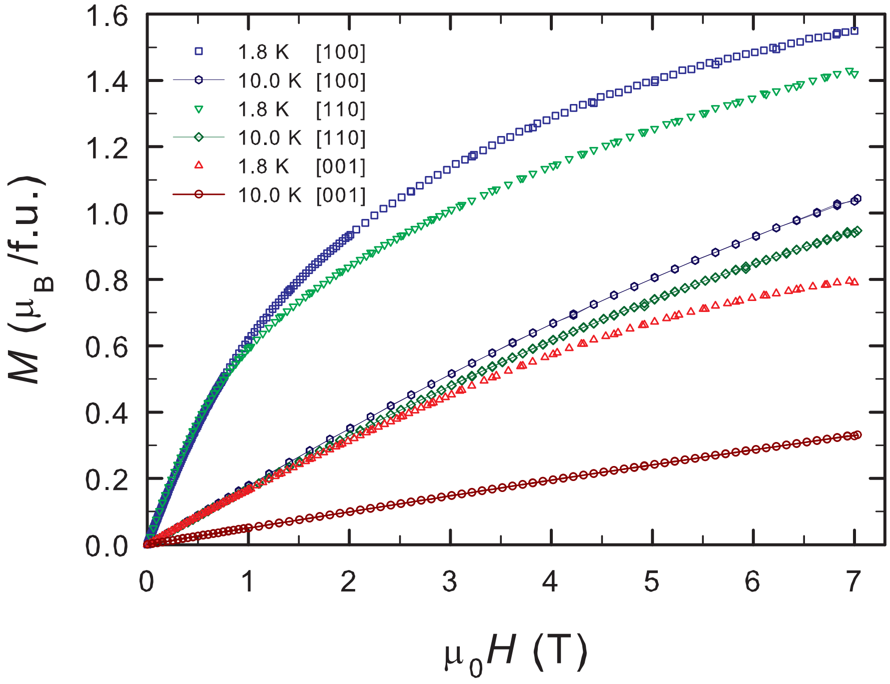

Figure 4.8: The magnetic field dependence of magnetization with magnetic field applied along [100], [110] and [001] directions at temperatures 1.8 and 10 K, i.e. below and above ordering temperature, respectively.

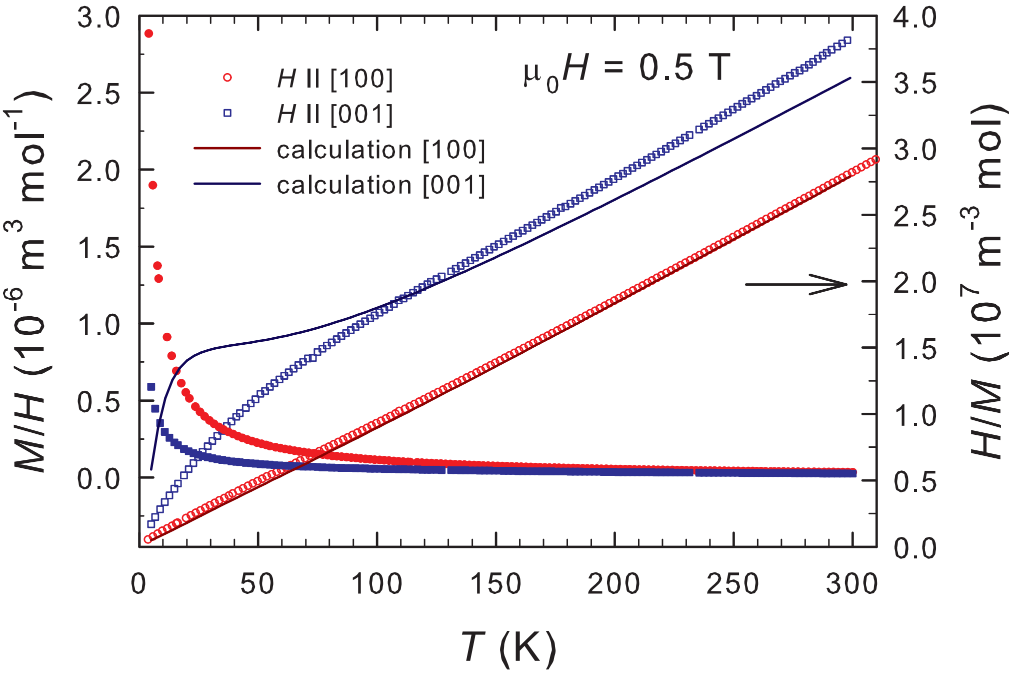

Figure 4.9: The temperature dependence of M/H measured with magnetic field of 0.5 T applied along principal crystallographic directions of CeCuAl$_3$ single crystal. The reciprocal magnetization, H/M, is also plotted. The lines are the calculated dependencies from crystal field parameters given in Ref. [4], see also section 3.2.

curve shows a kink around 30 K, which is not reproduced in the measured data. We note that the measurements were performed several times comparing as-cast samples, annealed samples and also on two sets of independent single crystals, in order to verify the reproducibility of observed M/H dependence. All of these measurements led to almost identical results, well in agreement also with previous study [51]. Any small changes of CF parameters do not lead to significant improvement. Presumably some common analysis of susceptibility and neutron scattering data might lead to a set of CF parameters which would satisfactory describe both experiments.

Specific heat

The specific heat data measured on CeCuAl$_3$ single crystal are shown in Figure 4.10. We observe a well pronounced λ-type anomaly at T_N. The idealization of the anomaly under constraint of the entropy conservation gives us $T_N = 2.5(1)$ K in a good agreement with magnetization data. The anomaly stays almost unaffected by small magnetic field applied along the c-axis. Small shift of the magnetic entropy to lower temperatures in 1 T is consistent with the antiferromagnetic order. The specific heat of a non-magnetic analogue LaCuAl$_3$ is shown in the inset as well. Above $\simeq 30$ K, it is very close to the specific heat of CeCuAl$_3$ as already observed also for polycrystalline sample. We can thus assume that the phonon contribution to total specific heat is very similar in both compounds and also the γ_{el}-coefficient of the electronic specific heat, $C_{el} = \gamma_{el}T$, is approximately the same ($\gamma_{\mathrm{el}} \approx 5$ mJ.mol^{-1}K^{-2}), at least in the paramagnetic region. The magnetic part is directly obtained as $C_{\mathrm{mag}} = C_{\mathrm{CeCuAl_3}} - C_{\mathrm{LaCuAl_3}}$ and its integration up to 300 K shows an increase towards the value of R.ln6 as expected for the Ce^{3+} state. Such an observation is in conflict with the potential 4 double-degenerated levels (ground state and 3 CF exciton-phonons excitated states) as mentioned in section 3.2.

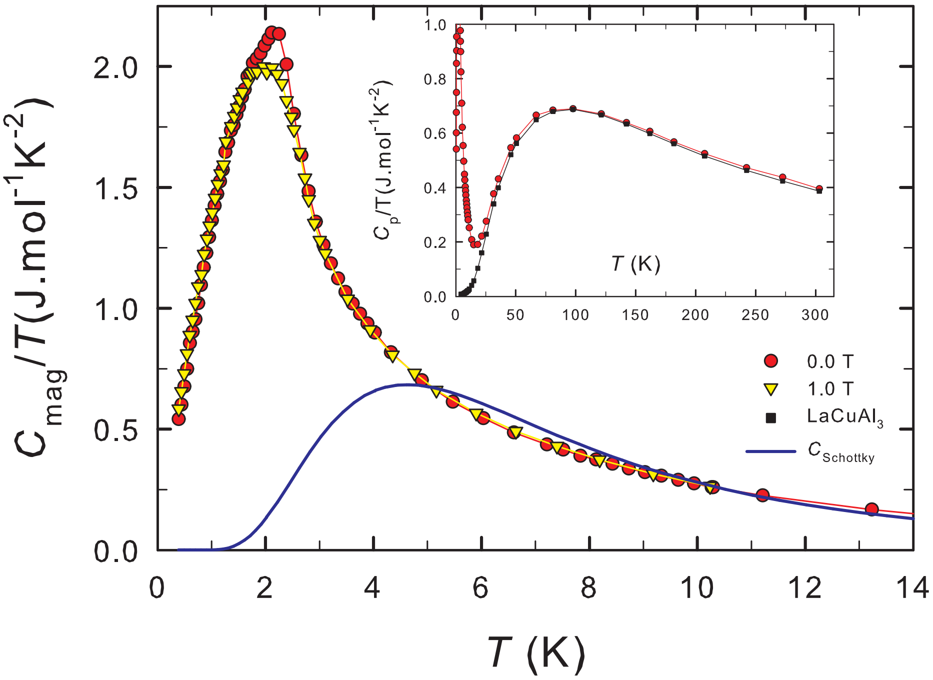

Figure 4.10: The specific heat in static magnetic fields of 0 and 1 T. The blue curve is the Schottky contribution to the specific heat calculated from energies obtained from inelastic scattering data [4]. The magnetic part of specific heat was obtained by substraction of the non-magnetic analogue LaCuAl$_3$ data. The inset shows both analogues in whole temperature range.

The magnetic specific heat in the paramagnetic region well above the ordering temperature is generally described by Schottky formula and the crystal field splitting of the multiplet ground state. As already mentioned above, the CF levels in CeCuAl$_3$ were directly observed by inelastic neutron scattering [4] around 1.3, 9.8 and 20.5 meV. The Schottky contribution calculated using only the levels on 1.3 and 20.5 meV is well in agreement with our specific heat data as demonstrated in Figure 4.10. Taking into account also the energy level at 9.8 meV with degeneracy one (and 20.5 meV level also with degeneracy one) is still well in agreement with the measured data. We note that, contrary to magnetization, the Schottky contribution to the specific heat depends only on the energies of CF levels, not on the corresponding wave functions. The detailed analysis of the specific heat in the magnetically ordered state leads to identical results as described for the polycrystalline sample (see section 4.1.6).

Electrical resistivity

The electrical resistivity measured in zero magnetic field with current along all three principal crystallographic directions is plotted in Figure 4.11. A relatively broad maximum around 10 K is clearly observable in resistivity data measured along all crystallographic directions in perfect agreement with previously published data by Kontani et al. [51]. The decrease below 10 K can be caused by the development of Kondo lattice state and crystal field effect at low temperatures as speculated in Ref. [51]. The kink at low temperatures demonstrates clearly the temperature of magnetic phase transition at around 2.5 K, in good agreement with magnetization and specific heat measurements (see Figure 4.11).

The magnetoresistivity measurements were performed in several arrangements with respect to the electrical current and magnetic field directions. There were 4 types of mutual arrangements of crystallographic directions, electrical current flow j and magnetic field H as shown in Figures 4.12 and 4.13. In all cases, the current flow was perpendicular to the magnetic field ($j \perp H$), i.e. transverse configuration. Temperature dependencies of resistivity in several static fields are plotted in Figure 4.12 and the magnetoresistance (MR) curves in Figure 4.13. Several differences can be traced depending on the experimental arrangement.

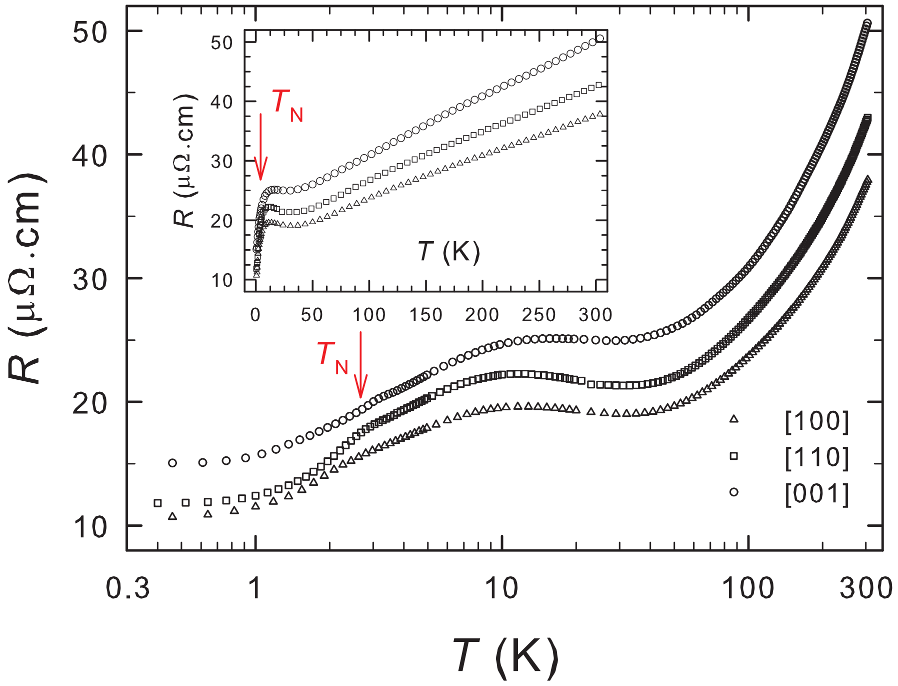

Figure 4.11: The temperature dependence of electrical resistivity with the current along significant crystalographic directions. The arrows indicate magnetic phase transition temperatures as determined from specific heat data.

Large negative magnetoresistance is observed for $j \parallel [001]$, resembling measurements reported for substituted $\mathrm{CeCu}_x\mathrm{Ag}_{1-x}\mathrm{Al}_3$ compounds [86]. Significant difference in resistivity development takes place for $j \perp [001]$ regardless the field direction. In these arrangements, positive MR appears for temperatures below T_N in magnetic fields up to 2-3 T (0.45 and 1.0 K curves in Figure 4.13). We

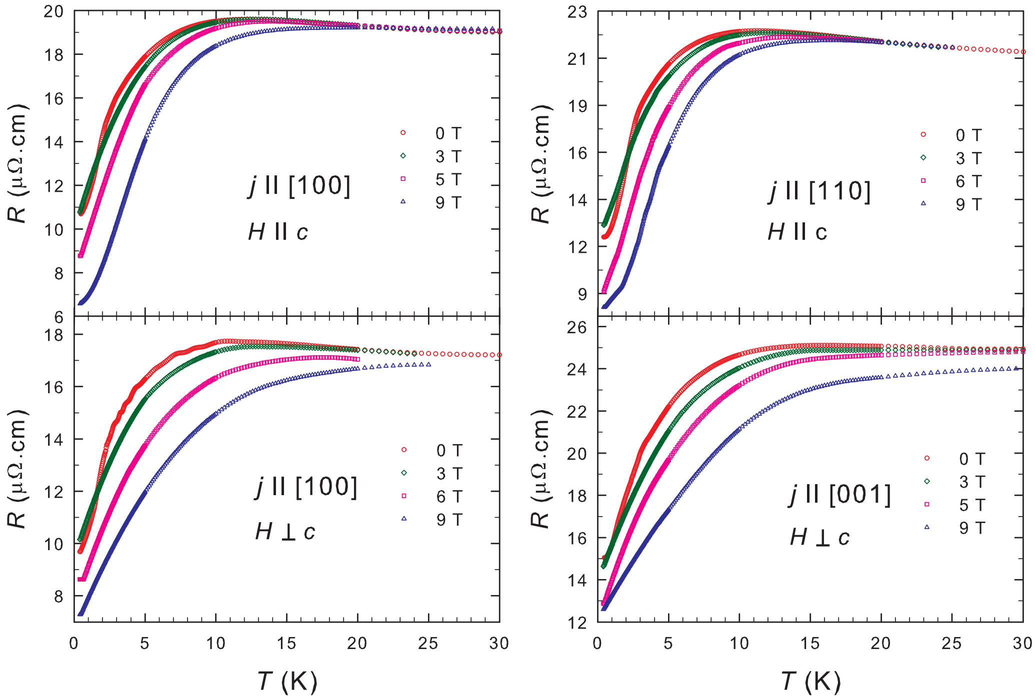

Figure 4.12: The temperature dependence of electrical resistivity in magnetic field measured in several experimental arrangements with respect to current j and magnetic field H directions.

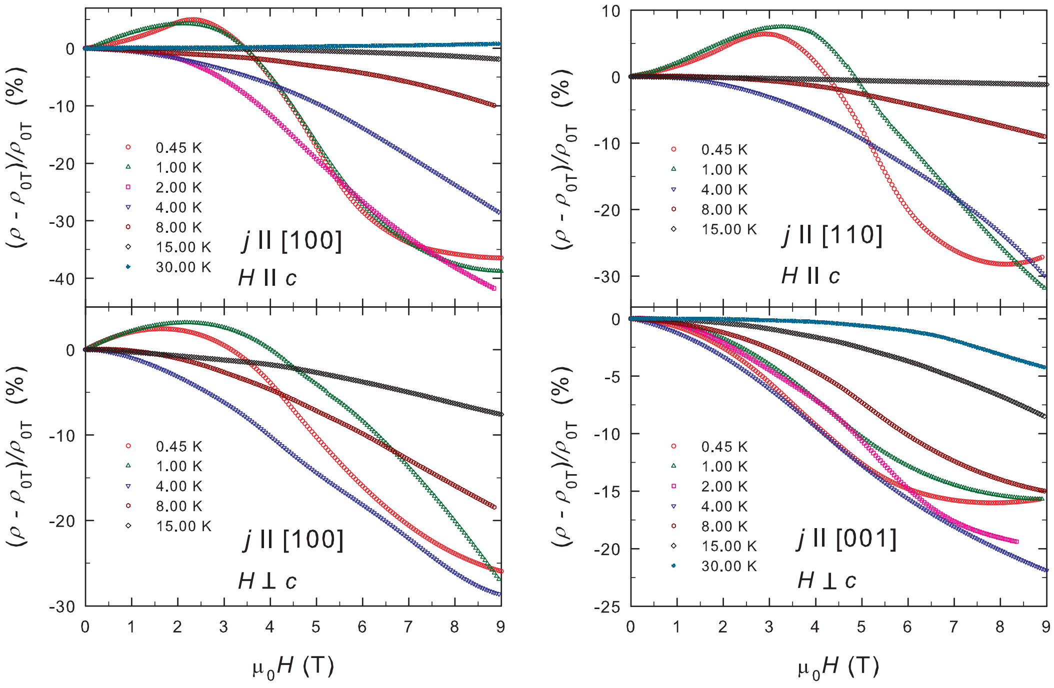

Figure 4.13: The magnetoresistance (MR $= \frac{\rho(H,T)-\rho(0,T)}{\rho(0,T)}$) at several temperatures below and above antiferromagnetic phase transition with the current along principal crystalographic directions. The transverse configuration ($j \perp H$) of current and magnetic field was used.

observe a clear maximum before the resistivity starts to decrease with further field increase. It suggest suppression of the antiferromagnetic order and arise of an induced ferromagnetic state, similarly as was observed for instance in $YbNiAl_2$ [85].

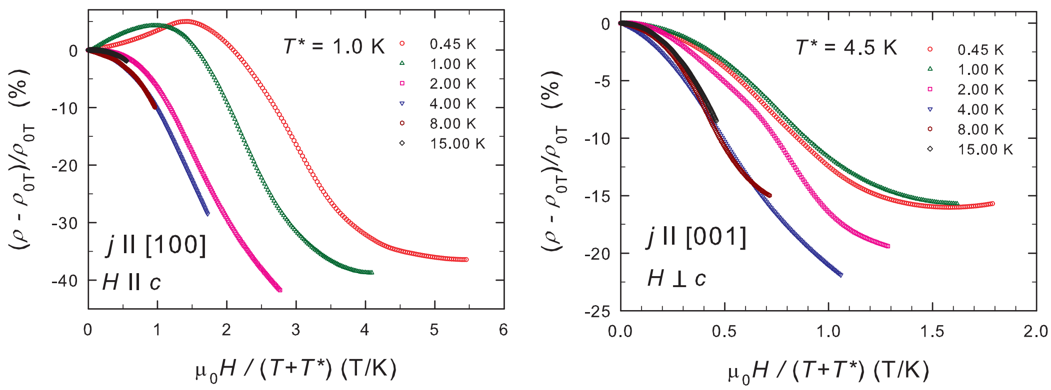

Figure 4.14: The magnetoresistance ($\mathrm{MR} = \frac{\rho(H,T)-\rho(0,T)}{\rho(0,T)}$) in dependence of $\frac{\mu_0 H}{T+T^*}$ in several temperatures with the electrical current along crystalographic directions [100] and [001] and magnetic field parallel and perpendicular to the c-axis, respectively. The overlap of curves measured at temperatures $> T_{\mathrm{N}}$ is observed.

In paramagnetic state, negative magnetoresistance is observed for all arrangements, but clear difference can be traced out for $H \parallel [001]$ and $H \perp [001]$. In the first case, the effect of 9 T field becomes negligible above 20 K, whereas in the latter case relatively large resistivity reduction remains up to 30 K (see Figure 4.12). The decrease of resistivity in rising field could be a result of probably ferromagnetic correlations between the cerium $4f$ moments. Another reason could be a suppression of the Kondo scattering with increasing field. Following the approach discussed also for $CeCu_xAg_{1-x}Al_3$ compounds [86], we can use the single-ion Kondo model with Bethe-ansatz studies [87]. Figure 4.14 is obtained by re-scaling the x-axis as $\frac{\mu_0 H}{T+T^*}$, where T is the temperature for the MR measurement and T^* is a measure of the strength of ferromagnetic correlations in the material [85, 88]. The dependencies measured at temperatures above T_{N} overlap with each other for characteristic temperature $T^* = 1.0$ and 4.5 K for $H \parallel [001]$ and $H \perp [001]$, respectively (the change of T^* by ± 0.5 K leads to much worse overlap between curves measured at $T > T_{\mathrm{N}}$). The former value is close to that found for polycrystalline $CeCu_{0.9}Ag_{0.1}Al_3$ [86]. Positive values of T^* imply that the ferromagnetic correlations between magnetic moments are rather weak. Lower value of T^* for magnetic field along [001] direction suggests that ferromagnetic correlations are stronger along the c-axis than in the basal plane. The development between magnetic and paramagnetic state is also demonstrated in Figure 4.14 (data measured at 2 K).

4.1.4 Magnetic structure in $CeCuAl_3$

To bring an unambiguous proof of the type of the magnetic order in $CeCuAl_3$, we have performed a series of neutron diffraction experiments on $CeCuAl_3$ single crystal. The measurement were performed using CYCLOPS (ILL, Grenoble, France), PANDA (FRMII, MLZ, Garching, Germany) and D10 (ILL, Grenoble, France) instruments on the same piece of single crystal. We note, that our previous effort to determine the magnetic structure in $CeCuAl_3$ using powder neutron diffraction (E6 instrument, HZB, Berlin) did not lead to any results. We were not able to observe any magnetic peak in diffraction patterns, presumably because of small size of magnetic moment on Ce.

Neutron diffraction on $CeCuAl_3$ single crystal

The magnetic order in $CeCuAl_3$ was studied first by Laue neutron diffraction on CYCLOPS diffractometer [89]. Laue patterns taken at 2 and 6 K are shown in Figure 4.15. The comparison of diffraction patterns obtained in the magnetically ordered state and in the paramagnetic state, respectively, revealed three weak magnetic reflections at low Q-region pointing to relatively small magnetic moment in the compound, in agreement with our previous powder neutron diffraction experiment. Positions of magnetic satellites out of the Bragg reflections unambiguously prove the antiferromagnetic ground state in $CeCuAl_3$. The analysis of the measured Laue patterns (using Esmeralda program [90]) allows us to determine several possible propagation vectors, $\vec{k}$, consistent with our data: (0.2, 0.2, 0), (0.33, 0, 0), (0.5, 0.25, 0), (0.4, 0.4, 0) and (0.4, 0.6, 0). We should note that, in addition, there are several other incommensurate vectors $\vec{k}$, which could describe the three found magnetic reflections as well. None of the determined vectors coincides with $(\frac{1}{2}, \frac{1}{2}, 0)$ propagation reported in the work of Oohara et al. [55].

The propagation vector of magnetic structure in $CeCuAl_3$ was found in course of our inelastic neutron scattering experiment on PANDA instrument. The mapping of reciprocal space revealed several magnetic reflections (two of them shown in Figure 4.16), which are described unambiguously by the propagation vector $\vec{k} = (0.4, 0.6, 0)$. The rest of possible propagation vectors determined from CYCLOPS data can be excluded. We followed temperature development of the intensity on the magnetic reflection (0.6, -0.4, 0), see Figure 4.17. The magnetic moment of $CeCuAl_3$ increases with decreasing temperature down to 1.7(1) K and remains constant (within the measurement error) at lower temperatures. The fit of the magnetic intensity to the power law $I \sim (T_\mathrm{N} - T)^{2\beta}$ revealed the ordering temperature of $T_\mathrm{N} = 2.7$ K, corresponding well to the one obtained from macroscopic measurements, see also Refs. [50, 51, 45, 52]. The obtained value of the critical exponent $\beta = 0.4$ is relatively close to the theoretical value of 0.313 expected for the Ising three-dimensional system [91].

The known structure parameters and propagation vector $\vec{k} = (0.4, 0.6, 0)$ were used to calculate possible magnetic structures using the representation analysis (employing the program BasIreps [11]). It should be noted, that there is only one crystallographic site for the Ce atom per magnetic unit cell and other Ce atoms are related by the symmetry operators. The calculation revealed two irreducible representations. Three basis vectors: (1, -1, 0), (1, 1, 0) and (0, 0, 1) belong to these representations where the latter two belong to the same irreducible representation. The one dimensional representation corresponds to moments within the basal plane. When the irreducible representation contains more than one basis vector, any linear combination of these vectors represents also allowed magnetic

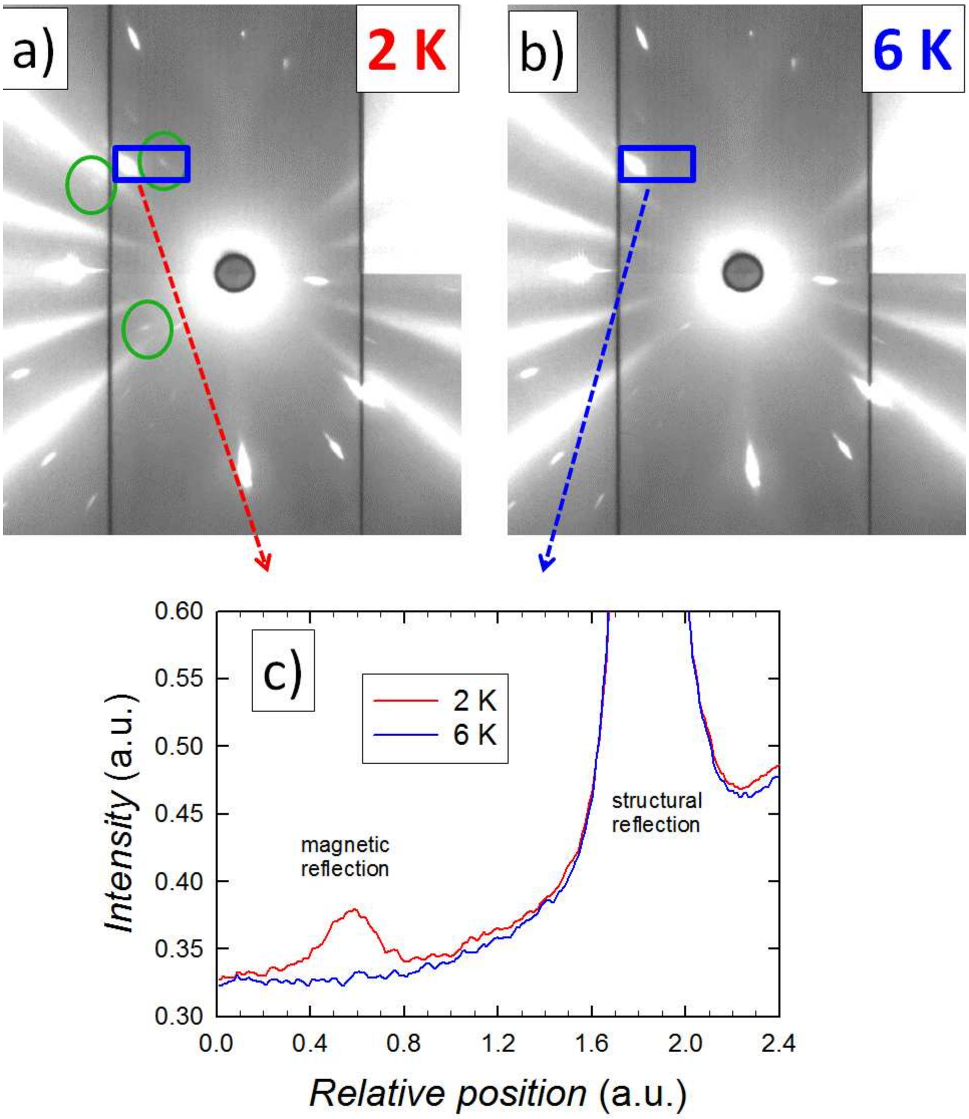

Figure 4.15: The Laue patterns obtained at 2 K and 6 K by CYCLOPS diffractometer at ILL, Grenoble. Three magnetic reflections are marked by green circles in panel a). The integrated intensities calculated by Esmeralda program [90] from Laue patterns are shown in panel c).

moment arrangements. The second, two dimensional representation, thus allows any direction of magnetic moments with respect to the c-axis. $BaNiSn_3$-type structure (I4mm, 107) is non-centrosymmetric structure, therefore propagation vector $\vec{k}$ is not equivalent to -$\vec{k}$. Both propagation vectors $\vec{k}$ and -$\vec{k}$ as well as propagation vectors (0.4, -0.6, 0) and (-0.4, 0.6, 0) have to be taken into account during the data refinement in the next step.

The magnetic structure described by propagation vector $\vec{k} = (0.4, 0.6, 0)$ was investigated by neutron diffraction experiment on D10 instrument. After thorough inspection of the crystal structure (the investigation of 24 nuclear reflections; allowed reflections satisfied the condition $h+k+l = 2n$ confirming body-centered space group), the intensities on magnetic satellites described by propagation vector $\vec{k}$ were measured at 1.7 K. The integrated intensities $|F_{\text{meas}}|$ of 25 measured

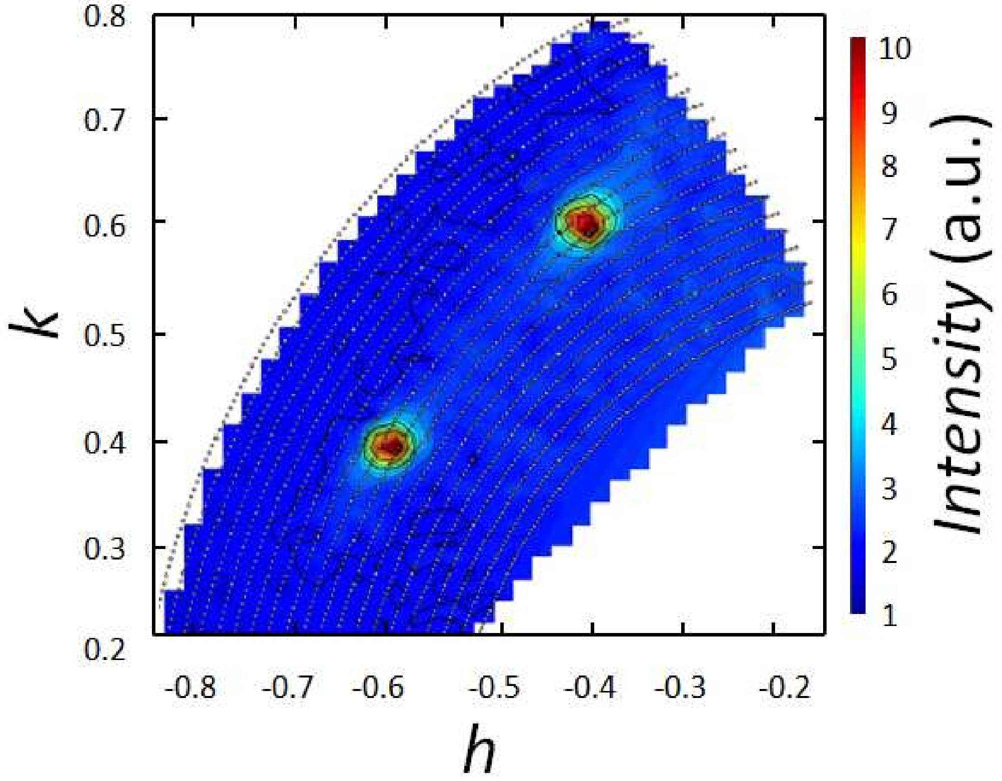

Figure 4.16: The map of hk-plane obtained by measurement on PANDA instrument in MLZ, Garching. Magnetic reflections (-0.6, 0.4, 0) and (-0.4, 0.6, 0) are observed.

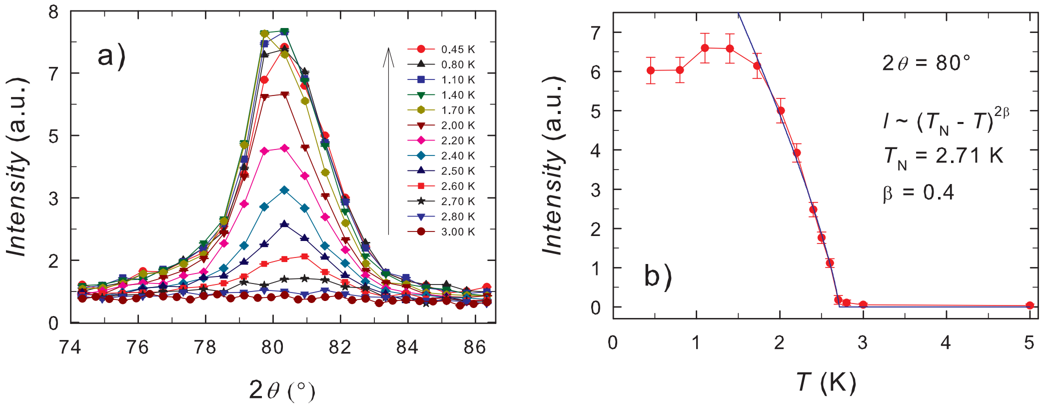

Figure 4.17: The temperature dependence of the intensity on magnetic reflection (0.6, -0.4, 0). The error bars on figure a) are within the symbols. The blue curve on panel b) is fit of the data to $I \sim (T_{\mathrm{N}} - T)^{2\beta}$.

independent magnetic reflections are listed in Table 4.4. All the magnetic reflections are the satellites of allowed nuclear reflections (described by $h+k+l = 2n$); zero intensity was found on (0.4, 0.6, 0) satellites of forbidden nuclear reflections ($h + k + l = 2n + 1$). The measured data were fitted to the model of magnetic structures based on the results of representation analysis using the Fullprof pack-

Table 4.4: 25 magnetic reflections with measured integrated intensities $|F_{\text{meas}}|$. $|F_{\text{calc}}|$ represents the calculated intensity processed by Fullprof program [11] for magnetic structure presented in Figure 4.18.

h	k	l	$\lvert F_{\text{meas}}\rvert$	$\lvert F_{\text{calc}}\rvert$
0.4	0.4	1	23(1)	21.3
-0.4	-0.4	1	25(1)	21.3
0.4	1.4	0	15(4)	12.6
-0.4	0.6	0	61(7)	61.2
0.6	0.6	1	13(1)	11.1
-0.6	-0.6	1	18(1)	11.1
0.4	-0.6	2	55(3)	58.3
-0.4	-1.4	2	22(3)	20.6
0.4	0.4	3	46(1)	45.5
-0.4	-0.4	3	50(1)	45.4
-0.6	1.4	3	39(2)	41.2
-1.4	0.6	3	40(3)	41.2
1.4	0.4	2	22(2)	20.6
0.6	-0.4	2	55(4)	58.3
1.4	-0.6	1	40(3)	44.8
0.6	-1.4	1	39(1)	44.8
0.6	0.6	3	31(1)	35.5
-0.6	-0.6	3	36(1)	35.5
1.6	-0.4	1	36(4)	37.0
-1.6	0.4	1	33(5)	37.0
-0.4	0.6	4	53(7)	48.0
0.4	-0.6	4	54(3)	48.0
-0.4	1.6	3	39(2)	35.7
0.4	-1.6	3	39(3)	35.7
0.6	1.6	0	16(5)	8.4

age [11]. The intensity on nuclear reflections measured in the paramagnetic and in the ordered state remains unchanged, excluding clearly $\vec{k} = (0, 0, 0)$ propagation of magnetic moments in CeCuAl$_3$. The extinction in the sample was treated by fitting the nuclear data to the phenomenological Zachariasen formula [26], while 6 fitting parameters corresponding to different crystallographic directions were used [11]. Consideration of extinction during the Rietveld refinement lead to the significant decrease of R_{F} factor (from 5.3% to 1.7%). The obtained parameters were fixed for the fit of magnetic data. The absorption of the material was not taken into account during the fitting as the intensity on equivalent reflections was the same within experimental error; CeCuAl$_3$ does not contain any strongly absorbing element.

Far best agreement between the magnetic data and fit ($R_{\text{F}} = 5.2\%$, see calculated intensities $|F_{\text{calc}}|$ in Table 4.4) was obtained for the magnetic structure with the arrangement of magnetic moments described by the (1, 1, 0) basis vector. The magnetic structure is of amplitude modulated type with maximum magnetic moment reaching 0.28(1) μ_B/Ce^{3+}, see Figure 4.18. The amplitude modulated magnetic structure with strongly reduced magnetic moments lying within the basal plane is well consistent also with results of previous ^{27}Al NQR study [92]. All magnetic reflections measured on D10 instrument are described by propagation vectors (0.4, -0.6, 0) and (-0.4, 0.6, 0). As follows from the representation analysis, any linear combination of (1, 1, 0) and (0, 0, 1) basis vectors should be considered. Considering non-zero component described by (0, 0, 1) would lead to tilting of magnetic moments out of the basal plane. Nevertheless, allowing a free z-component does not lead to any significant improvement of the fit and converges to a zero value of z-component. We should note, that allowing a subtle tilt of magnetic moments within the basal plane from [110] crystallographic direction leads to somewhat better agreement factor of $R_F = 4.3\%$. The model using the (1, -1, 0) basis vector gives an unacceptable fit with $R_F = 35.6\%$.

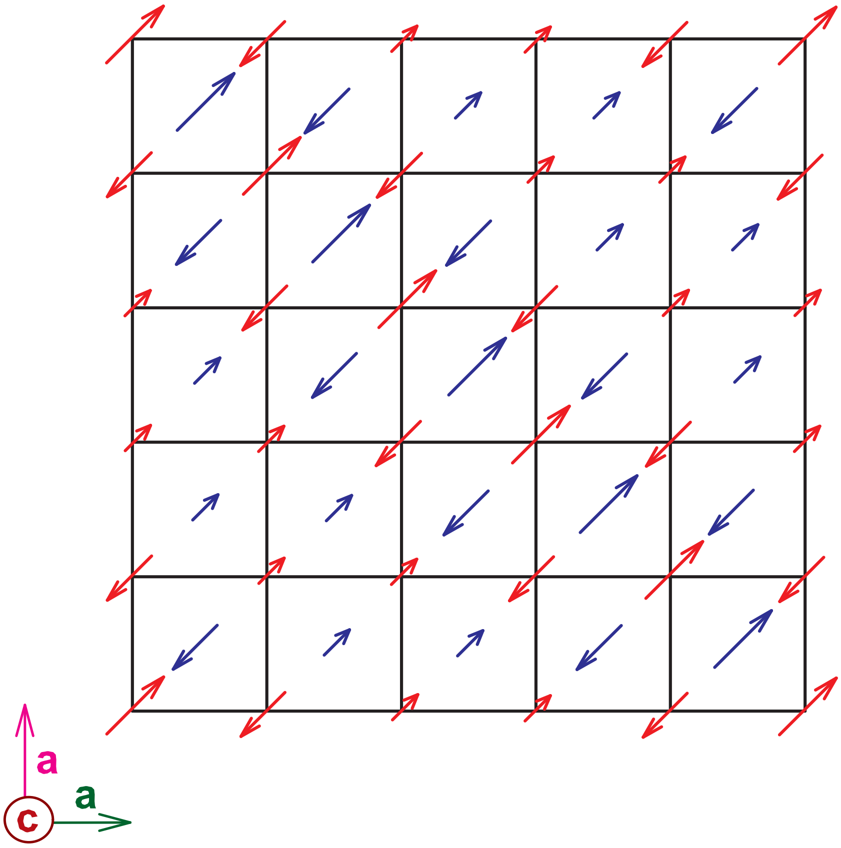

Figure 4.18: The magnetic structure of CeCuAl$_3$ described by propagation vector $\vec{k} = (0.4, 0.6, 0)$. Red arrows symbolize magnetic moments at $z_{\mathrm{Ce}} = 0$, blue arrows then moments at $z_{\mathrm{Ce}} = \frac{1}{2}$. All moments lie within basal planes.

The discrepancy between our results and previous study of Oohara et al. [55] needs to be further discussed. The propagation vector $(\frac{1}{2}, \frac{1}{2}, 0)$ found by former neutron diffraction experiment [55] is clearly not reproduced in any of our three independent neutron experiments, the agreement holds only for the z-component $k_z = 0$. Some differences in the crystal structure and/or sample quality may be a reason for different propagation vector. $CeCuAl_3$ crystal used by Oohara et al. [55] was originally reported to crystallize in the $BaAl_4$-type superlattice [51] without further details concerning e.g. atomic positions and occupancies. The experiments in our present work were performed on structurally well described single crystal with the tetragonal ordered non-centrosymmetric $BaNiSn_3$-type structure [74]. Moreover, during our experiments on PANDA and D10 instruments, we investigated the possibility of another magnetic propagation vector as presented in Ref. [55]. We found out a tiny peak corresponding to the reflection (0.5, 0.5, 0) and another one at (-0.5, 0.5, 0) reflection. The intensities of these peaks were considerably weaker than the ones observed for magnetic peaks described by propagation vector (0.4, 0.6, 0), see Figure 4.16 (the peak described as (-0.5, 0.5, 0) is not visible in the intensity scale). Nevertheless, we were able to examine these $(\frac{1}{2}, \frac{1}{2}, 0)$ peaks at temperatures from 1.7 K to 200 K during our measurement on D10 instrument. No change of the intensity of these peaks was observed in the whole temperature interval. On the other hand, the peaks described by $\vec{k} = (0.4, 0.6, 0)$ disappeared at temperature of 2.7 K (as demonstrated in Figure 4.17). $\frac{\lambda}{2}$ contamination from the (1, 1, 0) nuclear reflection might be a certain source of intensity on the $(\frac{1}{2}, \frac{1}{2}, 0)$ reflection. However Oohara et al. [55] presented the temperature development of the observed peak, which is in a strong disagreement with $\frac{\lambda}{2}$ contamination. Such a temperature evolution was not reproduced by our study. The structural difference thus remains the only explanation.

The measurements employing the inelastic neutron scattering on $CeCuAl_3$ [4] and $CeAuAl_3$ [84] strongly corroborate our results. The crystal field parameters obtained for both isoelectronic and isostructural compounds: $B_2^0 = 0.611$ meV, $B_4^0 = -0.015$ meV and $|B_4^4| = 0.317$ meV for $CeCuAl_3$ and $B_2^0 = 1.2036$ meV, $B_4^0 = -0.0031$ meV and $|B_4^4| = 0.4269$ meV for $CeAuAl_3$, lead to the same type of magnetic anisotropy with magnetic moments arranged within the basal plane. Indeed, our present study on $CeCuAl_3$ as well as previous investigation of $CeAuAl_3$ [84] reveal the magnetic moments to be confined within the basal plane. The magnetic structures are thus fully consistent with reported CF parameters. On the other hand, the $CeCuAl_3$ study of Oohara et al. [55] points out to the magnetic moments aligned along the c-axis, which is in the strong disagreement with our study and also with the CF parameters [4].

Magnetic structures in CeTX_3 compounds

We should discuss the value of magnetic moment in $CeCuAl_3$ (0.28(1) μ_B/Ce^{3+}) which is significantly reduced compared to full Ce^{3+} moment. Such a small ground state magnetic moment is not exceptional among CeTX_3 compounds adopting the $BaNiSn_3$-type structure. $CeCoGe_3$ compound reveals the magnetic moment of 0.405 μ_B/Ce^{3+} [41], $CeRhGe_3$ the moment of 0.45 μ_B/Ce^{3+} [39]. Even a smaller value of magnetic moment (0.13 μ_B/Ce^{3+}) was found in $CeRhSi_3$ [78]. A similar value is predicted also for $CeIrSi_3$ [79]. On the other hand, $CeCuGa_3$ (1.24 μ_B/Ce^{3+}) [47] and $CeAuAl_3$ (1.05 μ_B/Ce^{3+}) [84] reveal significantly higher magnetic moments. The small value of magnetic moment in these CeTX_3 compounds is often associated to the influence of Kondo effect on long-range magnetic ordering. However, the Néel temperature and Kondo temperature are similar for all CeTX_3 compounds pointing out to similar reduction of magnetic moment due to Kondo effect. It is thus unlikely, that the magnetic moments within CeTX_3 family differ so significantly because of a sole Kondo effect and other mechanisms have to be taken into account. The influence of crystal field plays an important role, however, the values of magnetic moments based on CF calculations are slightly higher then 1 μ_B/Ce^{3+} for above listed compounds. The previous ^{27}Al NQR studies on CeCuAl$_3$ [92] and NMR on CeAuAl$_3$ [93] brought the significant piece of information about the size of magnetic moment in these compounds. While in CeAuAl$_3$ the Ce magnetic moment is predicted to be reduced by about 25% due to Kondo screening [93], CeCuAl$_3$ should exhibit much smaller magnetic moment (< 0.2 μ_B/Ce^{3+}) [92]. Based on the ^{27}Al NQR results, the cancellation of the respective internal fields from nearest neighbor Ce moments is a probable explanation for such a small value. Indeed, the neutron scattering study on CeAuAl$_3$ [84] revealed significantly higher magnetic moment than that in CeCuAl$_3$ in our present study. This agreement shows, that the interatomic distances play crucial role in the formation of magnetic ground state. The reason behind so significantly different values of magnetic moment in CeTX_3 compounds needs to be further investigated, though. Presumably, the combination of neutron scattering and nuclear magnetic resonance techniques would bring proper explanation.

When comparing the magnetic propagation vectors within the CeTX_3 family of compounds crystallizing in the non-centrosymmetric BaNiSn$_3$-type structure, one can distinguish three different types of magnetic structure propagation: CeCuAl$_3$ ($\vec{k} = (0.4, 0.6, 0)$) and CeCuGa$_3$ ($\vec{k} = (0.176, 0.176, 0)$) [47] form the first group, in which the magnetic moments lie within the basal plane and the antiferromagnetic propagation occurs also within the basal plane. The second group is formed by compounds with the magnetic structure characterized by propagation vectors $\vec{k} = (k_x = k_y = 0,\, k_z \neq 0)$, i.e. the magnetic moments form ferromagnetic planes which are propagating antiferromagnetically along the c-axis. CeCoGe$_3$ with $\vec{k} = (0, 0, \frac{1}{2})$ [41], CeRhGe$_3$ with $\vec{k} = (0,\ 0,\ \frac{3}{4})$ [39] and recently investigated CeAuAl$_3$ with $\vec{k} = (0,\ 0,\ 0.52)$ [84] belong to this group. The last part of CeTX_3 family crystallizing in BaNiSn$_3$-type structure contains compounds with more complex magnetic structures described by more general propagation vectors: CeRhSi$_3$ and CeIrSi$_3$ show the propagation vectors (0.218, 0, 0.5) and (0.265, 0, 0.43), respectively [78, 79]. The systematics in the propagation of magnetic moments in these compounds is not obvious so far. One might expect, that the lattice parameters would play an important role in the magnetic structure formation. The c/a ratio itself does not seem to be the only driving parameter - rather close values of c/a ratio 2.48 and 2.51 are found for CeAuAl$_3$ and CeCuAl$_3$ compounds showing different propagation direction [74, 84], see Table 4.1. The c/a ratio in CeTGe$_3$ and CeTSi$_3$ takes the value of ≈ 2.3 [41, 39, 78, 79] and these compounds exhibit propagation vector with z-component $k_z \neq 0$.

The nearest interatomic Ce-Ce distance (i.e. lattice parameter a, see Table 4.1) seems to be crucial for the ordering of magnetic moments in CeTX_3 compounds: CeCuAl$_3$ [74] and CeCuGa$_3$ [47] with $k_z = 0$ exhibit nearest Ce-Ce neighbors distances lower than 4.3 Å, whereas CeCoGe$_3$ [41], CeRhGe$_3$ [39] and CeAuAl$_3$ [84] with $a >$ 4.3 Å propagate along the tetragonal axis ($k_z \neq 0$). In the third group formed by CeRhSi$_3$ [78] and CeIrSi$_3$ [79], both a and c are relatively small (i.e. small lattice volume), what brings the second nearest Ce-Ce neighbors

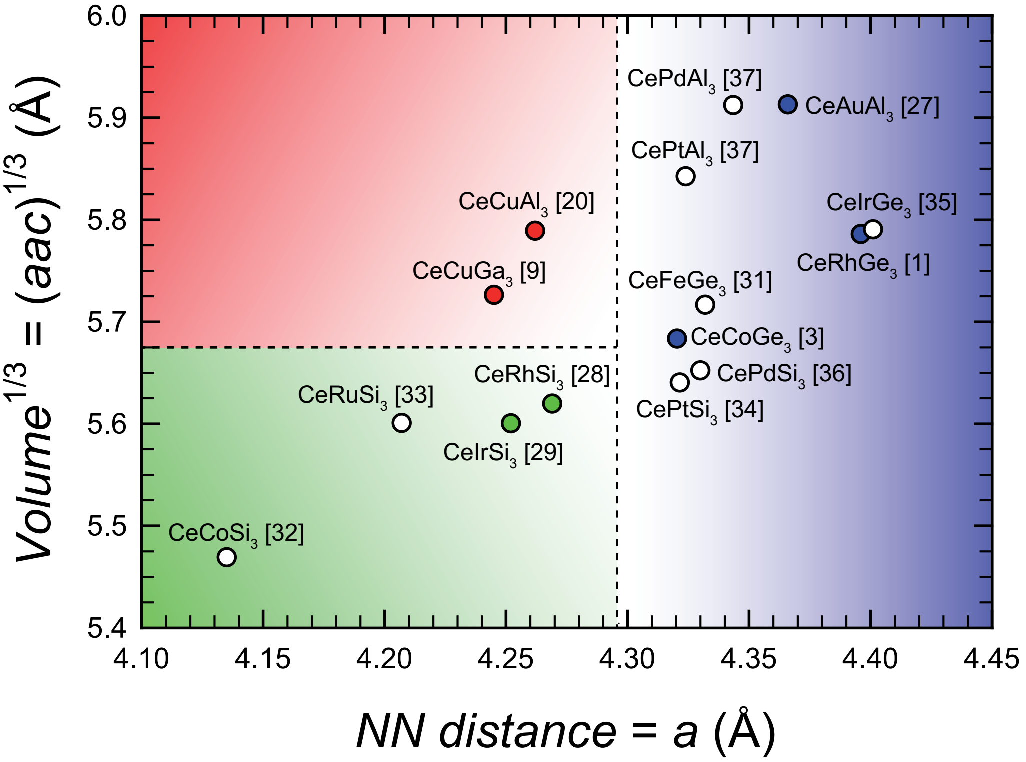

Figure 4.19: The lattice parameters of CeTX_3 compounds. Nearest Ce-Ce neighbors distance, i.e. lattice parameter a vs. cube root of volume of elementary unit cell $(aac)^{\frac{1}{3}}$ is shown. The colored symbols mark the type of magnetic propagation vector as discussed in text: red symbol belongs to the compounds with zero z-component of magnetic propagation vector, blue symbol then to the compounds with ($k_x = k_y = 0$, $k_z \neq 0$) and green symbol marks the compounds with more complex propagation vectors. White circles denote compounds with not yet revealed magnetic structures. The colored areas accordingly denote predicted propagation in other CeTX_3 compounds.

significantly closer to each other (≈ 5.7 Å, compare to ≈ 6.1 Å for $CeCuAl_3$ [74] and $CeCuGa_3$ [47]) and probably has some impact on the magnetic propagation. We are aware that the tentative considerations above are based on the knowledge of magnetic structures only in a rather limited number of compounds. We have constructed a phase diagram of CeTX_3 compounds (presented in Figure 4.19) based on above considerations and lattice parameters listed in Table 4.1. CeTX_3 compounds are divided into three groups according to their lattice parameter a (i.e. nearest interatomic Ce-Ce distance) and volume of elementary unit cell. This arrangement respects the type of magnetic propagation vector in all previously studied compounds. The predictions on the type of magnetic propagation vector for other CeTX_3 compounds has to be yet confirmed.

4.1.5 Inelastic scattering on $CeCuAl_3$ single crystal

The lowest lying magnetic excitations in $CeCuAl_3$ were investigated by inelastic neutron scattering on single crystal employing ThALES spectrometer at the ILL, Grenoble. Figure 4.20 shows the energy transfer scans around $\vec{Q}$ point (0.4, 0.6, 0) below and above the ordering temperature (T_N = 2.7 K). The temperature development of the peak around 1.5 meV corresponds well to the results on the polycrystalline sample [4] and clearly points out to the crystal field nature of this peak. Moreover, the observed peak is $\vec{Q}$-independent as expected for CF excitation.

Below ordering temperature, we observe an additional anomaly at around 1 meV, which could be tentatively attributed to the magnetic excitations in ordered state.

The CF peak-feature sits on top of broader continuum, which extends to about 3 meV energy transfer and seems to be temperature independent, suggesting an interplay between magnetic moment correlations, Kondo screening of magnetic moments and crystal field effects similarly as in $\mathrm{CeIn_3}$ [94]. Nevertheless, the experiment with polarized neutron analysis is needed to reveal the nature of this anomaly properly.

In a future study on IN20 spectrometer with polarized neutron analysis is planned (accepted proposal at ILL) to investigate the higher-energy part of spectrum of $\mathrm{CeCuAl_3}$, i.e. to study the whole picture of crystal field excitations as well as vibron state in single crystal. Such a study intends to bring further understanding into the CF exciton-phonons interaction as we are able to distinguish between magnetic and phonon contributions to the INS spectra using polarized analysis on IN20 spectrometer.

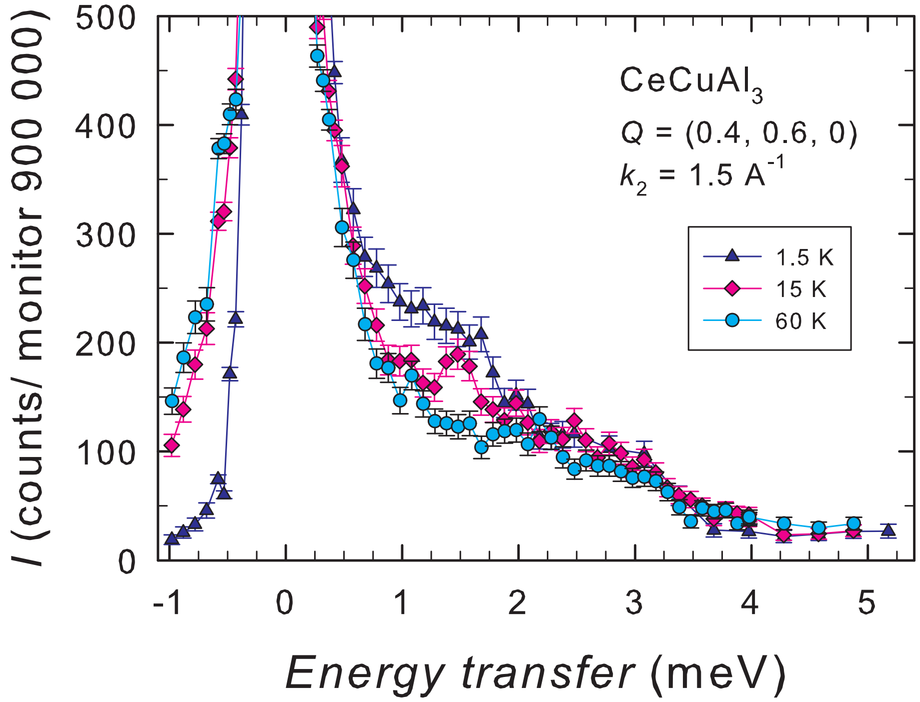

Figure 4.20: The low-energy part of inelastic neutron scattering spectrum of $\mathrm{CeCuAl_3}$ measured using the ThALES spectrometer at ILL, Grenoble. The measurement was performed at $\vec{Q}$ point (0.4, 0.6, 0) with scattered $\vec{k}_2$ = 1.5 $\mathrm{\AA}^{-1}$. The intensity is given in units of counts per monitor as the counting time per different parts of the spectrum were different. The time for measuring one point at around 1.5 meV was ≈ 7 min.

4.1.6 Crystal field excitations in $Ce(Cu,Al)_4$ compounds

Together with the detailed investigation of $CeCuAl_3$ single crystal, we studied also several substituted systems to obtain a broader picture of the microscopic nature of $CeCuAl_3$ and its changes with the doping (as mentioned in section 3.2).

$Ce(Cu,Al)_4$ compounds have been to some extent investigated, see e.g. Refs. [54, 95, 96]. The previous magnetization measurements of $CeCu_xAl_{4-x}$ single crystals, compounds with $x = 0.7, 0.8, 0.9, 1.0$ and 1.1, revealed the a-axis as the easy magnetization axis for all concentrations and a clear strengthening of the ferromagnetic interactions with decreasing Cu content [54, 95]. The ordering temperature showed only a weak concentration dependence. The crystal field splitting of the two lowest doublets deduced from the magnetization curves increases roughly linearly from ~ 9 K to ~ 24 K with decreasing x from 1.1 to 0.7 [54, 95]. In the case of $x \cong 0.7$ compound, this relatively small crystal-field splitting was ruled out by specific heat measurements which indicated much higher splitting between the ground state and first excited state [96]. This discrepancy together with the the effort to track the change of nature of the magnetic ground state in these compounds motivated us to perform investigation of the $CeCu_xAl_{4-x}$ system by means of specific heat and mainly neutron scattering measurements.

Specific heat in $Ce(Cu,Al)_4$ compounds

Polycrystalline samples of $CeCu_xAl_{4-x}$ with x between 0.75 and 1.25 were prepared by arc-melting stoichiometric mixtures of pure elements in a mono-arc furnace under protection of an argon atmosphere. The samples were turned and re-melted several times to achieve better homogeneity. Subsequently, the samples were annealed for 7 days in evacuated quartz tubes at temperature of 800°C.

The X-ray diffraction showed that all the prepared samples crystallize in the tetragonal $BaNiSn_3$-type structure with a partial disorder of Cu-Al atoms on the 4(b) positions corresponding to non-stoichiometricity of compounds with $x \neq 1$. The determined lattice parameters are given in Table 4.5. Both a and c decrease nearly linearly with increasing the Cu content up to $x = 1.1$ and stay almost constant for higher Cu concentrations. The decrease of c is much steeper, the c/a ratio therefore decreases as well. The samples appear to be single phase for concentrations up to $x = 1.1$, diffraction patterns of samples with higher Cu concentrations contained also several weak foreign peaks. Previous phase composition study showed solid solubility of the $CeCu_xAl_{4-x}$ ternary system to be in the range $0.73 < x < 1.10$ [97]. Our results thus seem to be consistent with this observation, furthermore indicating that for $x > 1.1$ the phase with the $BaNiSn_3$-type structure still remains as a major phase, but probably with the $CeCu_{1.1}Al_{2.9}$ composition. This surmise was subsequently confirmed by the EDX analysis on selected samples. The expected composition and homogeneous Cu-Al distribution was found for samples with $x \leq 1.1$. In contrary, $CeCu_{1.25}Al_{3.75}$ sample showed three phases: the major phase with the $CeCu_{1.1}Al_{2.9}$ composition and two minor phases with a compositions that roughly correspond to $Ce(Cu_{0.6}Al_{0.4})_5$ (mentioned also in [97]) and cubic Laves phase $CeAl_2$ with a small admixture of Cu in place of Al.

The specific heat of studied materials consists of the phonon, C_{ph}, electronic, C_{el}, and magnetic, C_{mag}, contributions. The phonon contribution in magnetic

Table 4.5: Structural parameters of $\mathrm{CeCu}_x\mathrm{Al}_{4-x}$ compounds and characteristics derived from the specific heat data. Lattice parameters and the unit cell volume, $V_{\mathrm{f.u.}}$, were determined from powder X-ray diffraction at room temperature. T_{ord} is the ordering temperature, S_{ord} the magnetic entropy at T_{ord} used for the estimation of Kondo temperature, T_{K}, using equation 4.2. δ and A_{mag} are parameters which result from the fit to equation 4.1.

x	0.7 [96]	0.75	0.8	0.9	1.0	1.1
$\mathrm{CeCu}_x\mathrm{Al}_{4-x}$						
a (Å)	4.262	4.263(1)	4.260(1)	4.255(1)	4.256(1)	4.253(1)
c (Å)	10.776	10.729(2)	10.713(2)	10.663(2)	10.663(2)	10.595(2)
$V_{\mathrm{f.u.}}$ (Å^3)	195.7	195.0(1)	194.4(1)	193.0(1)	192.6(1)	191.6(1)
T_{ord} (K)	4.0	3.5(2)	-	3.0(2)	3.0(2)	2.6(2)
S_{ord} (J.mol^{-1}K^{-1})	3.3	3.4	-	4.1	4.1	3.7
T_{K} (K)	7.2(5)	6.3(4)	-	4.3(4)	4.2(4)	4.3(4)
δ (K)	0.4	0.16	-	-	0.23	0.18
A_{mag} (J.mol^{-1}K$^{-5/2}$)	0.9	1.0	-	-	1.7	1.8
$\mathrm{LaCu}_x\mathrm{Al}_{4-x}$						
a (Å)	-	4.306(1)	4.301(1)	4.294(1)	4.294(1)	4.291(1)
c (Å)	-	10.757(2)	10.746(2)	10.703(2)	10.669(2)	10.654(2)
$V_{\mathrm{f.u.}}$ (Å^3)	-	199.5(1)	198.8(1)	197.4(1)	196.7(1)	196.1(1)

compounds can be often reasonably estimated from the specific heat of the nonmagnetic analogues with the same crystal structure and similar mass and unit cell dimensions. In the case of $\mathrm{CeCu}_x\mathrm{Al}_{4-x}$ series, $\mathrm{LaCu}_x\mathrm{Al}_{4-x}$ compounds represent a natural choice for this purpose (see also section 1.1). Concerning the electronic part, one has to be more careful. This contribution can be expressed as $C_{\mathrm{el}} = \gamma_{\mathrm{el}}T$, where γ_{el} is the coefficient proportional to the density of states at the Fermi level. The Ce-based compounds show often enhanced C_{el} compared to equivalent compounds containing other rare-earth. We plot the specific heat of $\mathrm{CeCu}_x\mathrm{Al}_{4-x}$ and $\mathrm{LaCu}_x\mathrm{Al}_{4-x}$ compounds for the two border concentrations ($x = 0.75$ and 1.1) in Figure 4.21. The specific heat of the two remaining compounds ($x = 0.9$ and 1.0) lies between C_{p} of the two drawn concentrations above 20 K and is not shown to avoid large overlapping. The difference between the Ce and La analogues smoothly decreases with increasing temperature, what rather clearly indicates that also the electronic contribution should be almost the same ($\gamma_{\mathrm{el}} \cong 5$ mJ.mol^{-1}K^{-2}) in the Ce and La-based analogues, at least at higher temperatures in the paramagnetic region. The magnetic part, C_{mag}, in $\mathrm{CeCu}_x\mathrm{Al}_{4-x}$ compounds was then calculated simply by subtracting C_{p} of the corresponding La analogue. The obtained magnetic entropies, S_{mag}, are displayed in the inset of Figure 4.21. It shows a general tendency to saturate close to the expected value of R.ln6, what confirms that the La compounds represent suitable approximation of the nonmagnetic contributions.

Let us now analyze C_{mag} in the paramagnetic region. Well above the ordering

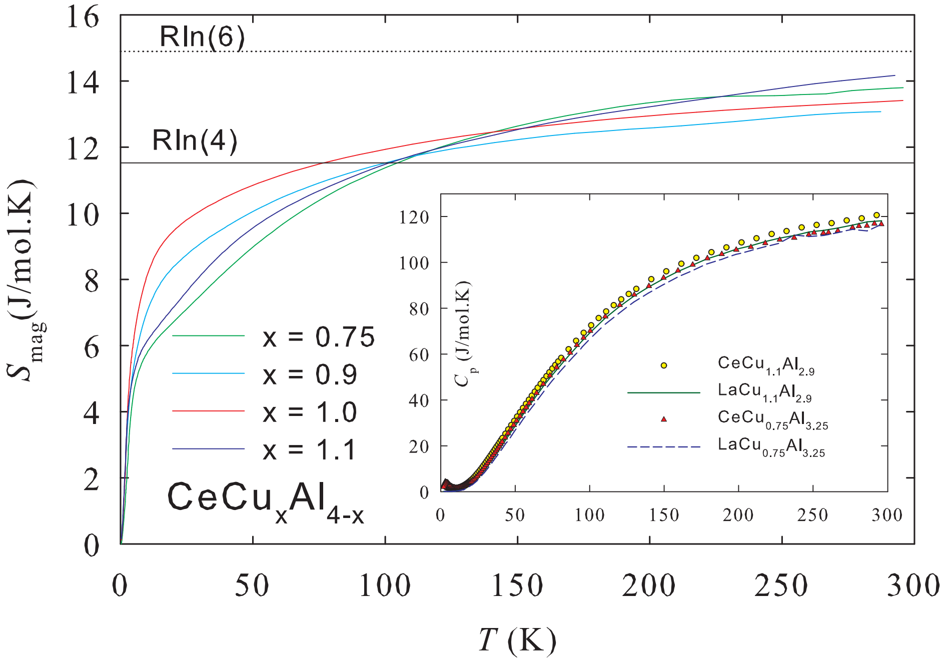

Figure 4.21: The magnetic entropy of CeCu$_x$Al$_{4-x}$ compounds in the whole measured temperature range. The inset shows the temperature dependence of the specific heat of CeCu$_x$Al$_{4-x}$ and LaCu$_x$Al$_{4-x}$ ($x = 0.75$ and 1.1) compounds. The other concentrations exhibit basically similar behavior above 10 K.

temperature (listed in Table 4.5), it is assumed to be described by usual Schottky contribution describing the crystal field excitations, see equation 2.7.

The CF energy levels at $E_1 = 1.3$ meV and $E_2 = 20.5$ meV were directly observed by inelastic neutron scattering in CeCuAl$_3$ [4]. The Schottky contribution calculated using these values is compared with experimental data in Figure 4.22. The main features are reproduced, especially the enhancement of C_{mag} below 20 K. The difference between observed and calculated data may be ascribed to certain dispersion of the CF levels and possible small differences in the phonon spectra of CeCuAl$_3$ and LaCuAl$_3$. We have also to remind the existence of the vibron state in CeCuAl$_3$, see section 3.2 [4], which certainly influences both the phonon and Schottky contributions.

Certain development of the energy splitting between the ground state and first excited state with respect to Cu concentration x was deduced from magnetization curves [54]. E_1 was reported to increase almost linearly from ~ 0.8 meV for $x = 1.1$ to ~ 2 meV for $x = 0.7$ [54, 95]. The predicted value of $E_1 \sim 2$ meV for CeCu$_{0.7}$Al$_{3.3}$ is however in a strong disagreement with the heat capacity data [96]. According to the specific heat, it was suggested that E_1 should lie above ~ 7 meV. Our present analysis is in a good agreement with this former study. We can clearly exclude existence of E_1 around 2 meV for CeCu$_{0.75}$Al$_{3.25}$ even considering all the uncertainties mentioned above for CeCuAl$_3$. We estimate $E_1 \simeq 8.6$ meV, the corresponding data are drawn in Figure 4.22. CeCu$_{0.9}$Al$_{3.1}$

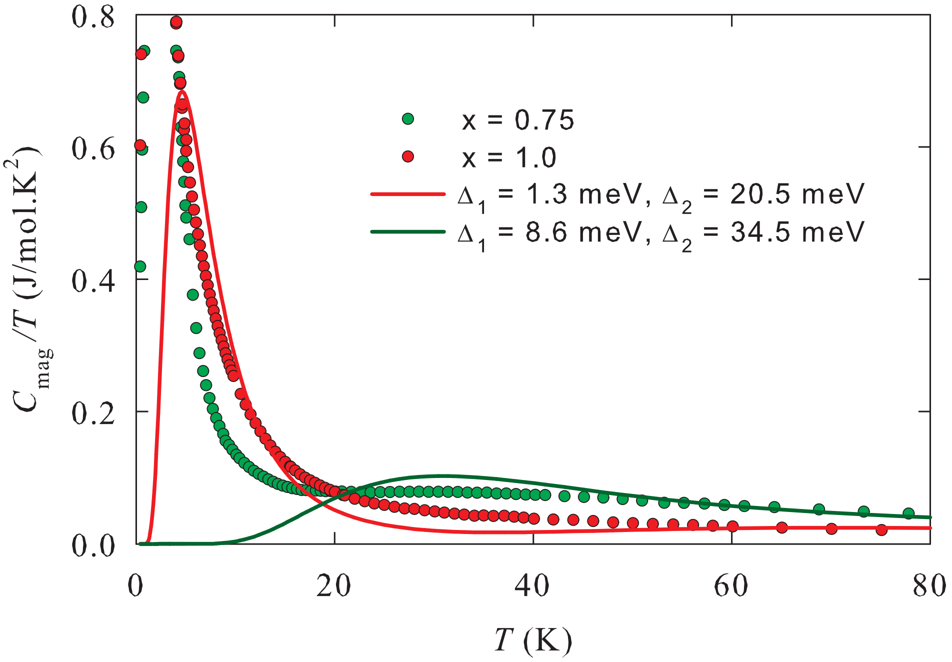

Figure 4.22: The magnetic specific heat in the paramagnetic region. The full lines represent calculation of Schottky contribution to specific heat using equation 2.7.

shows rather similar behavior as CeCuAl$_3$ with a large C_{mag} below 20 K and thus relatively small splitting E_1, whereas CeCu$_{1.1}$Al$_{2.9}$ is much closer to CeCu$_{0.75}$Al$_{3.25}$ (compare also the entropy in Figure 4.21). We can thus tentatively conclude that the energy splitting to the first excited state does not follow a linear dependence on x as previously suggested [54], but instead seems to have a minimum value around the stoichiometric CeCuAl$_3$ and increase strongly for x moving away from 1.0. This speculative picture is to be confirmed by inelastic neutron scattering.

The low-temperature part of C_{mag}/T for all concentrations is drawn in Figure 4.23. For comparison, we include also the data of CeCu$_{0.7}$Al$_{3.3}$ taken from Ref.[96]. The deduced ordering temperatures are summarized in Table 4.5. CeCu$_{0.9}$Al$_{3.1}$ shows an additional transition at $T_1 = 1.2$ K. The temperature dependence of C_{mag} below T_{ord} seems to be qualitatively similar for all compounds. It is somewhat surprising as the ground state was reported to develop between ferromagnetic for CeCu$_{0.7}$Al$_{3.3}$ [95, 54] and antiferromagnetic in CeCuAl$_3$. The $C_{\mathrm{mag}} \approx T^3$ dependence which should occur in a typical 3D antiferromagnet is clearly not observed for any Cu-Al concentration. Therefore, we tried to follow the approach applied for CeCu$_{0.7}$Al$_{3.3}$ and fit the data below T_{ord} to the following formula [98, 96]:

$$C_{\mathrm{mag}} = e^{-\frac{\delta}{T}} A_{\mathrm{mag}} T^{\frac{3}{2}}. \tag{4.1}$$

The coefficient A_{mag} is related to the spin velocity in the magnetically ordered state and δ is the energy gap in the magnon dispersion relation. The $T^{\frac{3}{2}}$ term corresponds to 3D ferromagnetic magnons. The results of the fit are summa-

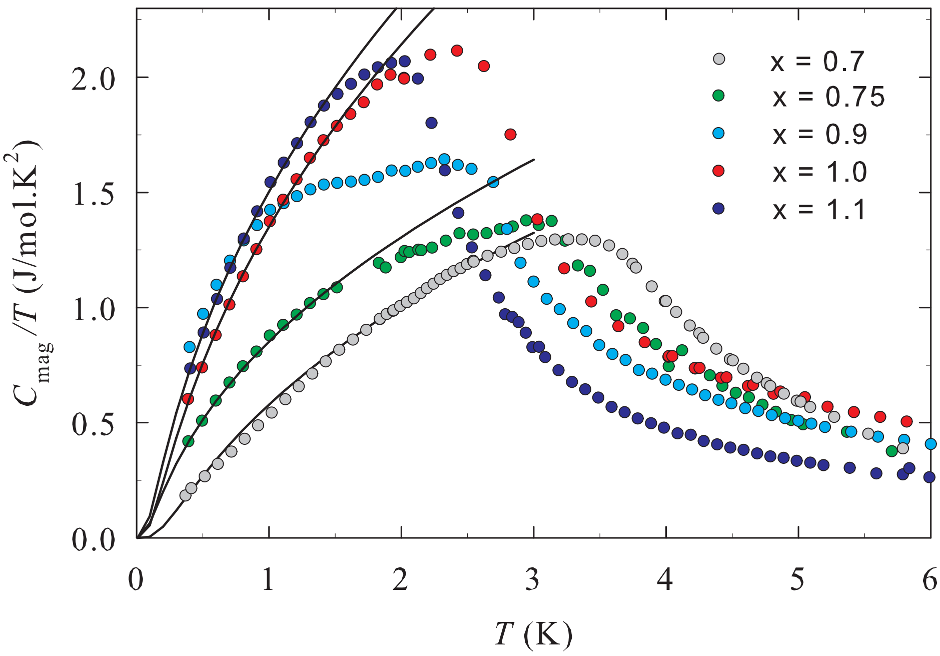

Figure 4.23: The low temperature part of the magnetic specific heat. The full lines represent the fit to equation 4.1 with the parameters listed in Table 4.5. The data for $CeCu_{0.7}Al_{3.3}$ were taken from Ref. [96].

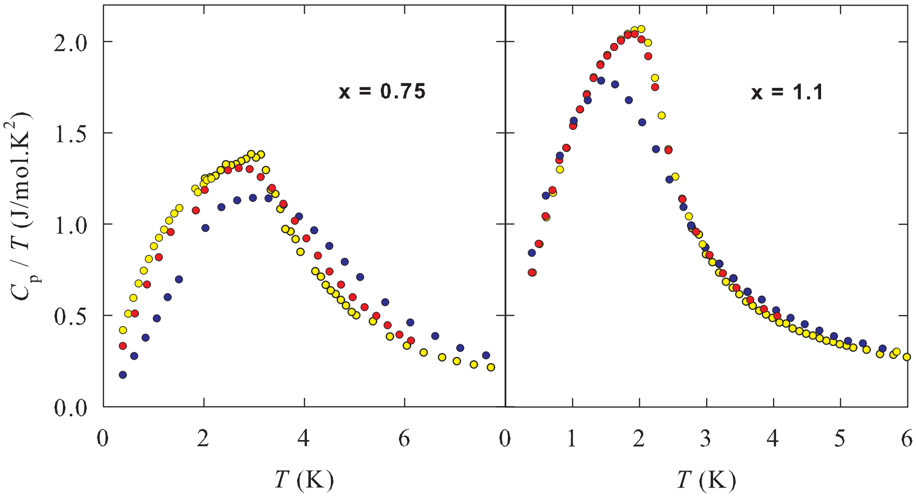

Figure 4.24: The low-temperature specific heat of $CeCu_xAl_{4-x}$ ($x = 0.75$ and 1.1) measured in external fields of 0.0 T (yellow), 0.2 T (red) and 1.0 T (blue).

rized in Table 4.5 and the calculated data are drawn in Figure 4.23, except for $CeCu_{0.9}Al_{3.1}$ where the temperature region below T_1 is too small to perform a reasonable fit. As can be seen from Figure 4.23, the data are well reproduced. All the parameters listed in Table 4.5 were obtained assuming no increase of the electronic part at low temperatures. To allow better comparison, we refit also the data for $x = 0.7$ [96] under this condition. Introducing additional $\gamma_{\mathrm{el}}T$ term in equation 4.1, which would reflect larger low-temperature γ_{el}-value compared to the paramagnetic state, leads still to reasonable fits for γ_{el} up to $\simeq 100$ mJ.mol^{-1}K^{-2}. The value of δ would then also change as both parameters are highly correlated.

Another quantity which can be directly evaluated from the low-temperature $\frac{C_{\mathrm{mag}}}{T}$ data is the magnetic entropy at the ordering temperature, S_{ord}. The determined values are listed in Table 4.5. We note that we do not include the Schottky part into it. Nevertheless, it would represent only a minor change of $\simeq$ 5% of S_{ord} in CeCuAl$_3$ where the first excited state occurs at lowest energy. All the values are lower compared to R.ln2 expected for a doublet ground state for Ce^{3+} ion in an ideal case. The reduction can be ascribed to competing Kondo effect which exhausts part of the magnetic entropy above the ordering temperature. The Kondo temperature can be roughly calculated using the simple calculation based on the two-level model [99]:

$$\frac{S_{T_{\mathrm{N}}}}{R} = \ln(1 + \mathrm{e}^{-\frac{T_{\mathrm{K}}}{T_{\mathrm{N}}}}) + \frac{T_{\mathrm{K}}}{T_{\mathrm{N}}} \frac{\mathrm{e}^{-\frac{T_{\mathrm{K}}}{T_{\mathrm{N}}}}}{1 + \mathrm{e}^{-\frac{T_{\mathrm{K}}}{T_{\mathrm{N}}}}}, \tag{4.2}$$

where R is universal gas constant. The calculated T_{K} are given in Table 4.5. The value for $x = 0.7$ was corrected, the original value written in Ref. [96] does not correspond to the given S_{ord} and T_{ord}. Although the absolute value of T_{K} might differ depending on the type of measurement and analysis approach, the trend should be credible: T_{K} decreases with increasing x between 0.7 and 0.9 and then stays almost unchanged up to $x = 1.1$. It is a somewhat surprising tendency as one expects usually an opposite development of T_{ord} and T_{K}.

An important information about the nature of the ground state can be obtained from the influence of external magnetic field on C_{mag}. We have performed measurements in 0.0, 0.2 and 1.0 T, the results are presented in Figure 4.24. We observe a clear qualitative change between CeCu$_{0.75}$Al$_{3.25}$ and CeCu$_{1.1}$Al$_{2.9}$. In the former case, the entropy (i.e. the area below C_{p}/T) is clearly shifted to higher temperatures already in 0.2 T. It is usually a sign of the ferromagnetic order. It is consistent with previous studies which report ferromagnetic order in CeCu$_{0.7}$Al$_{3.3}$ [95, 96]. Contrary to that, specific heat of CeCuAl$_3$ (see also subsection 4.1.3) and CeCu$_{1.1}$Al$_{2.9}$ is almost unaffected by 0.2 T field, small shift of the entropy to higher temperatures occurs in 1 T. Such behavior might be expected for an antiferromagnet with a slow gradual transition towards ferromagnetic ordering in increasing magnetic field. CeCu$_{0.9}$Al$_{3.1}$ shows a more complex field development representing possibly some transition between both types of behavior.

Inelastic neutron scattering on Ce(Cu,Al)$_4$

The inelastic neutron scattering experiments on CeCu$_x$Al$_{4-x}$ compounds were performed using IRIS and MARI spectrometers at ISIS, Didcot, in collaboration with Dr. Devashibhai T. Adroja. The purpose of the investigation of substituted compounds with $x = 0.75$, 0.9 and 1.1 was to follow a development of the crystal field excitations and vibron state with Cu-Al substitution. According to previous bulk properties measurements and especially the specific heat data analysis (see previous section), we expected the energy spectrum of CeCu$_{0.9}$Al$_{3.1}$ to be similar to parent CeCuAl$_3$, including the additional magneto-phononic excitation peak in the spectrum. The other two compounds with Cu content $x = 0.75$ and 1.1 were expected to exhibit a qualitatively different energy spectrum, presumably without any additional magnetic peak.

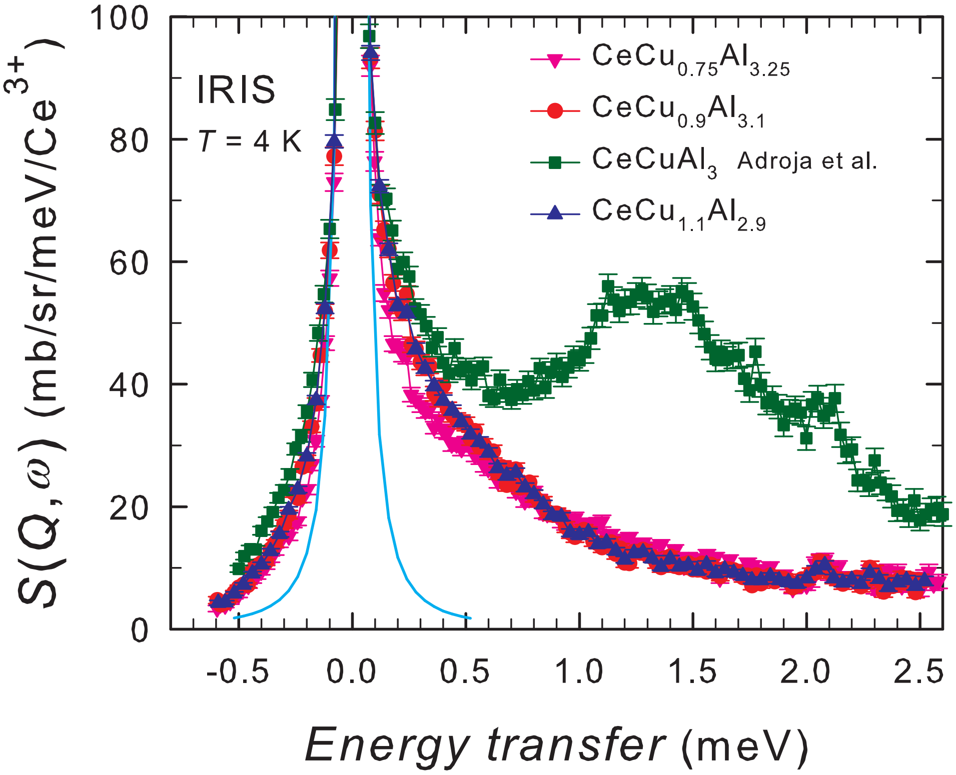

Figure 4.25: The low-energy part of spectra of CeCu$_x$Al$_{4-x}$ measured at 4 K. A clear difference between the parent CeCuAl$_3$ (taken from Ref. [4]) and substituted compounds is observed. The blue full line represents the lorentzian fit of the elastic peak.

The low-energy parts of spectra of investigated compounds measured employing IRIS spectrometer are presented in Figure 4.25. Compared to the parent CeCuAl$_3$ revealing a clear CF peak at around 1.3 meV [4], the substituted compounds exhibit only quite broad quasielastic feature at low energies which is observed also in pure CeCuAl$_3$ [4]. The low-energy parts of spectra of all substituted compounds are very similar. Nevertheless, on the basis of measured data we cannot exclude a shift of CF excitations in substituted compounds to very low energies. A further investigation of low-energy part of spectra (below 1 meV) is necessary and we will perform the INS measurement on IN6 spectrometer at the ILL, Grenoble (accepted proposal).

The higher energy part of CeCu$_x$Al$_{4-x}$ spectra was investigated using MARI spectrometer and measured data are presented in Figure 4.26. The presented data were obtained by subtracting La analogue data from CeCu$_x$Al$_{4-x}$ via relation $S_{\mathrm{M}}(\vec{Q},\omega) = S^{\mathrm{CeCu_xAl_{4-x}}}(\vec{Q},\omega) - \alpha . S^{\mathrm{LaCu_xAl_{4-x}}}(\vec{Q},\omega)$, where α (= 0.673, 0.688 and 0.706) is the ratio of total-scattering cross sections for RCu$_x$Al$_{4-x}$ with R = Ce and La and $x = 0.75$, 0.9 and 1.1, i.e. purely magnetic excitations are shown.

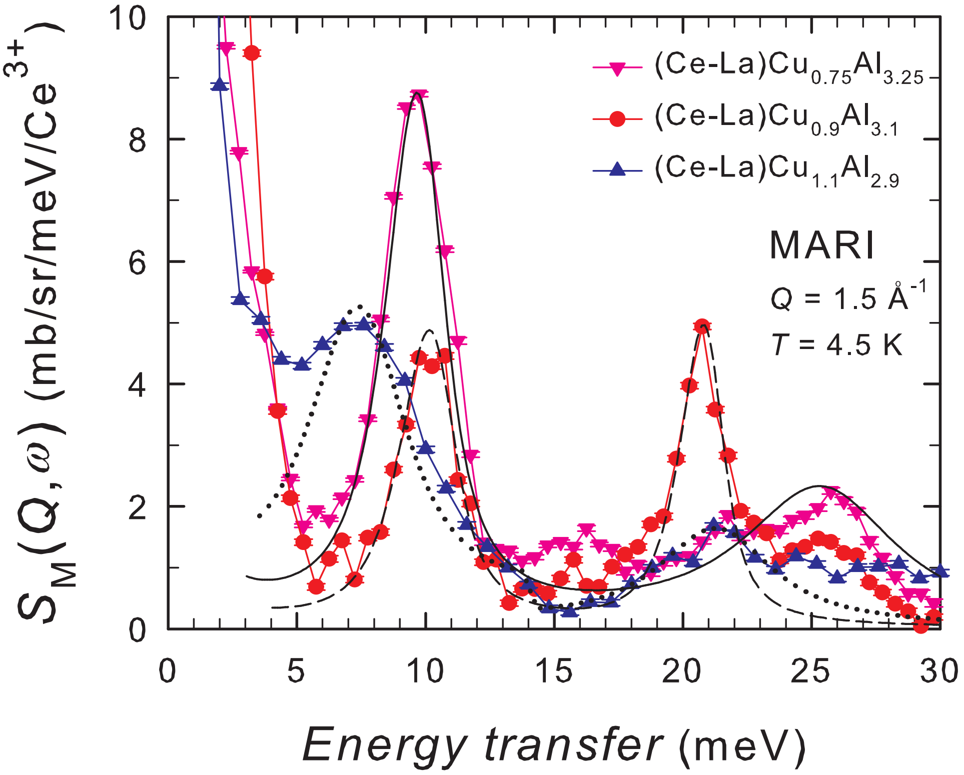

Figure 4.26: The inelastic neutron scattering energy spectra measured on CeCu$_x$Al$_{4-x}$ using MARI spectrometer. The presented magnetic data were obtained by substraction of La analogues data from CeCu$_x$Al$_{4-x}$ data as explained in text.

Two clear CF peaks in energy spectrum of all three investigated Cu-Al substituted compounds are observed. The intensities on observed peaks differ significantly for different Cu-Al content; the most noticeable difference could be traced in comparison to the parent CeCuAl$_3$, see Figure 3.2. The peak around 10 meV found for CeCu$_x$Al$_{4-x}$ with $x \leq 1$ shifts to lower energy of 7 meV in CeCu$_{1.1}$Al$_{2.9}$. Moreover, the intensity on 10 meV peak decreases with increasing Cu content from $x = 0.75$ to $x = 1$, while for concentration with $x = 1.1$ the intensity of 7 meV peak is higher again. Such a development of the intensity might point out to the presence/absence of the CF peak at low-energy part of the spectra, i.e. a small intensity on 10 meV peak originates in the presence of the CF peak at low energies (at around 1.3 meV in CeCuAl$_3$ [4]), while higher energy means no low-energy CF excitations. In other words, a strong CF exciton-phonon interaction has also a great impact on the intensity of all CF (CF-phonon) peaks. Such an assumption seems to be correct as we do not observe any CF peak at low energies for substituted compounds (see Figure 4.25), however, a further investigation and mainly theoretical description are necessary.

The measured CeCu$_x$Al$_{4-x}$ INS spectra in Figure 4.26 were fitted to the CF Hamiltonian presented in equation 1.7 and the refined CF parameters are in listed in Table 4.6. The refined CF parameters do not differ significantly as the CF excitations are found at similar energies. In contrast with parent CeCuAl$_3$, B_4^0 parameter has a positive sign leading to no CF excitation in low-energy part

Table 4.6: The parameters and eigen-values of crystal field Hamiltonian describing the CF excitations in CeCu$_x$Al$_{4-x}$ compounds. Data were measured at 4.5 K. The data for pure CeCuAl$_3$ were taken from Ref. [4]. See text and Figure 4.26 for more details.

x	0.75	0.9	1.0 [4]	1.1
Δ_1 (meV)	9.8(1)	10.1(1)	1.3	7.2(2)
Δ_2 (meV)	26.3(2)	20.7(2)	9.8	20.6(2)
Δ_2' (meV)			20.5	
B_2^0 (meV)	0.90(2)	0.61(2)	0.611(2)	0.88(8)
B_4^0 (meV)	0.042(1)	0.039(1)	-0.015(1)	0.045(1)
B_4^4 (meV)	0.265(3)	0.229(3)	0.317(4)	0.210(4)

of the spectra of all substituted compounds. The parameter B_2^0 develops also remarkably: B_2^0 is almost the same for pure CeCuAl$_3$ [4] and for $x = 0.9$ substitution, whereas it differs significantly for $x = 0.75$ and 1.1 (and stays almost the same for these two concentrations). The other two CF parameters have a similar values in all three substituted compounds. Such a development of CF parameters with Cu-Al substitutions suggests that CeCu$_{0.9}$Al$_{3.1}$ stays closest to parent CeCuAl$_3$ (the CF exciton-phonons interaction is still not strong enough to invoke an additional magneto-elastic peak), while other to compositions reveal quite different energy spectra.

We note the presence of another two small peaks at around 15 and 25 meV in energy spectra of CeCu$_{0.75}$Al$_{3.25}$ and CeCu$_{0.9}$Al$_{3.1}$, respectively. These peaks could be associated with phonon peaks, which differ slightly in Ce and La analogues, i.e. the phonon part of spectra is not completely subtracted from the data. Second explanation could be the presence of strong CF exciton-phonon interactions, which cannot be proven due to relatively strong phonon peaks. Third possibility could be a variation of composition of studied samples; there was a large amount of sample used for the measurement. Nevertheless, the samples were thoroughly checked by X-ray diffraction and EDX analysis before the experiment, which showed single phase samples.

4.2 CePd$_2$Al$_2$ and CeT_2X_2 compounds

The ternary intermetallic CeT_2X_2 compounds (where T = transition element d-metal and X = p-metal) stay in the foreground of interest already many years. The physical properties as heavy-fermion behavior, valence-fluctuations, non-Fermi-liquid behavior or pressure induced superconductivity are frequently present in CeT_2X_2 compounds crystallizing in the ThCr$_2$Si$_2$-type structure (space group I4/mmm), see Figure 4.1 and Refs. [100, 101, 102, 29, 104, 105, 106, 107]. The observed behavior is frequently discussed with respect to the competition between RKKY and Kondo interactions. The influence of the crystal electric field is also a strong mechanism one has to take into account. The second crystal structure in which CeT_2X_2 compounds were often found to crystallize, CaBe$_2$Ge$_2$-type (P4/nmm), differs from the former one only by a different stacking of the layers along the tetragonal c-axis, see Figure 4.1. Nevertheless, such a structure difference influences significantly the electronic properties as well as the structure stability of CeT_2X_2 compounds. The compounds crystallizing in $CaBe_2Ge_2$-type structure typically do not reveal properties mentioned above for those crystallizing in $ThCr_2Si_2$-type. On the other hand, compounds crystallizing in $CaBe_2Ge_2$-type structure undergo a structural phase transition to structures with lower symmetry (or structural distortion) in many cases, see Refs. [108, 3, 109, 110] as an example.

$CePd_2Al_2$ crystallizes in the $CaBe_2Ge_2$-type structure and reveals both structural instability and interesting physical properties. $CePd_2Al_2$ was reported to undergo the structural phase transition from tetragonal ordered centrosymmetric $CaBe_2Ge_2$-type structure to centrosymmetric orthorhombic Cmma-type structure at $T_{\mathrm{struc}} = 13.5$ K [3]. See Figures 4.1 and 4.27 for the illustration. Beside the structural phase transition, another highly interesting phenomenon was observed in $CePd_2Al_2$: the inelastic neutron scattering energy spectra display an additional peak which cannot be described in terms of pure crystal field splitting [3]. The Thalmeier-Fulde model based on CF exciton-phonons interactions [36] well describes this additional peak with following parameters of crystal field and electron-phonon interaction [3]: $\mathrm{B}_2^0 = 0.6$ meV, $\mathrm{B}_4^0 = 0.0302$ meV, $\mathrm{B}_4^4 = 0.027$ meV and $\mathrm{g}_0 = 1.41$ meV. See also chapter 3.

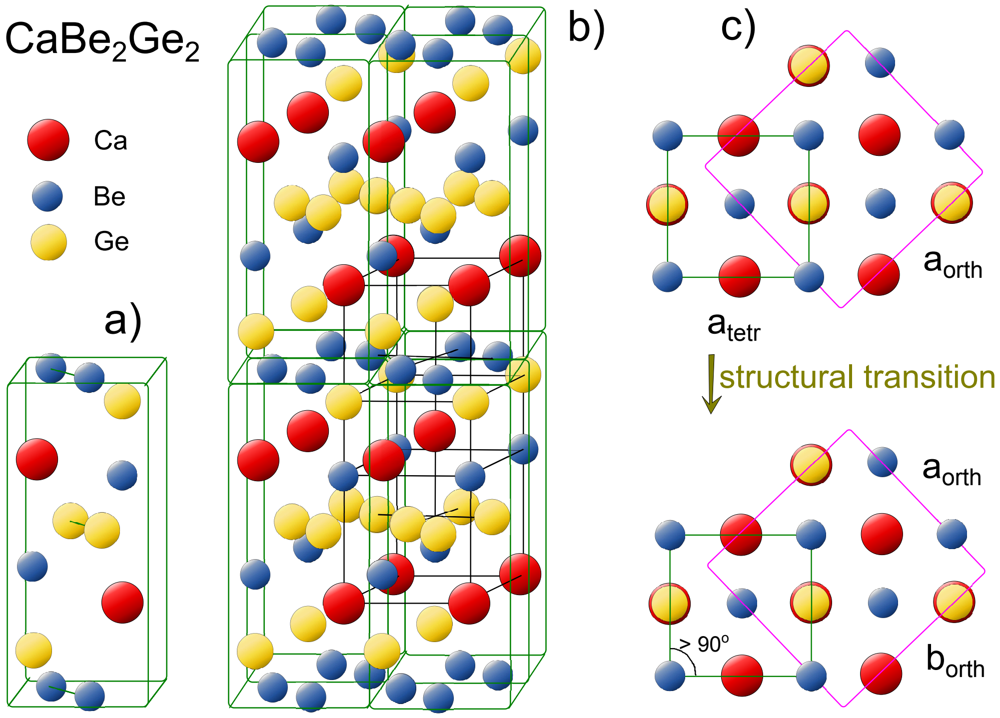

Figure 4.27: The elementary unit cell of tetragonal centrosymmetric ordered $CaBe_2Ge_2$-type structure (a), 8 elementary unit cells with marked unit cell as shown in Figure 4.1 (b) and transition from tetragonal to orthorhombic Cmma structure (c). Tetragonal (orthorhombic) plane is shown in figure (c).

$LaPd_2Al_2$ reveals the same type of structural phase transition as $CePd_2Al_2$ at temperature $T_{\mathrm{struc}}^{\mathrm{La}} = 91.5$ K [3]. The temperature of structural transition in Ce and La counterparts is discussed with respect to the presence of vibron state: the strong electron-phonon interaction stabilizes the tetragonal phase in $CePd_2Al_2$, i.e. the structural transition is observed at lower temperatures than for La analogue [3].

4.2.1 $CePd_2Al_2$ single crystal

To investigate physical properties in $CePd_2Al_2$ in detail, we prepared a single crystalline sample. Our study of single crystal is described in detail in the master thesis of Petr Doležal [62] and in our paper [64], especially then the results concerning the magnetization measurement, electrical resistivity measurement and measurement of the electrical resistivity under hydrostatic pressure.

Preparation and structure characterization

The $CePd_2Al_2$ single crystal was prepared from polycrystalline precursor using the tri-arc furnace employing modified Czochralski pulling method (see section 2.1). Grown sample was additionally sealed in quartz glass and annealed at 800°C for 10 days. Prepared single crystal was checked first by Laue X-ray diffraction pointing to a single grain crystal adopting a tetragonal structure. Subsequently, small part of ingot was crushed and investigated by powder X-ray diffraction at room temperature. The one phase diffraction patterns were fitted to the model containing the tetragonal ordered centrosymmetric $CaBe_2Ge_2$-type structure (space group 129, P4/nmm) using the Rietveld analysis employing the Fullprof program [11]. The best fit was obtained for lattice parameters: $a = 441.5(1)$ pm and $c = 987.5(2)$ pm (with the agreement factors $R_{\mathrm{Bragg}} = 6.5\%$ and $R_{\mathrm{f}} = 6.4\%$). The obtained values of lattice parameters are well in agreement with polycrystalline data (see subsection 4.2.2 and Ref. [111]).

The EDX analysis revealed a single phase sample with the stoichiometry Ce:Pd:Al = 1:2:2. The composition was checked on several places of the crystal, showing small deviations from homogeneous distribution of individual elements. These deviations were lower than 3%, i.e. comparable or slightly exceeding the experimental error.

Magnetization measurement

The temperature dependencies of magnetization in the paramagnetic region measured along and perpendicular to the c-axis are presented in Figure 4.28. The measurement along basal plane directions [100] and [110] (not shown for better lucidity) led to almost the same dependencies, indicating very small basal-plane anisotropy. The data were fitted to the Curie-Weiss law (equation 2.2) in temperature region from 80 to 300 K for all directions resulting in the effective magnetic moment values of 2.59 μ_{B} and 2.45 μ_{B} for directions [100] and [001], respectively, close to the value expected for Ce^{3+} free ion. The paramagnetic Curie temperature, θ_{P}, was estimated to be -3.4 K and -80.0 K for directions [100] and [001], respectively. The values of H/M and corresponding Curie-Weiss fits (black lines) are shown in Figure 4.28. The negative values of θ_{P} for both crystallographic directions suggest the antiferromagnetic order. The large difference between the θ_{P} values obtained for $H \parallel [100]$ and $H \parallel [001]$ reflects a strong CF anisotropy in $CePd_2Al_2$. The comparison of M/H for [100] and [001] then indicates the magnetization easy basal-plane in $CePd_2Al_2$.

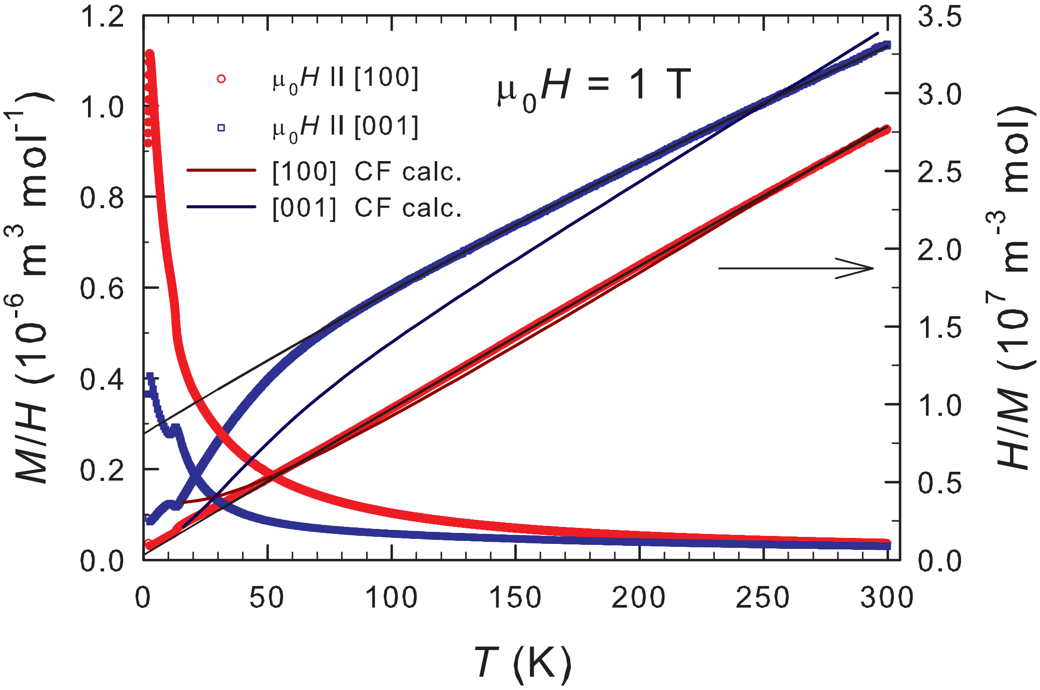

Figure 4.28: The temperature dependencies of M/H measured with external magnetic field of 1 T along [100] and [001] directions. The reciprocal values are presented as well. The black lines are $H/M(T)$ dependencies calculated from parameters μ_{eff} and θ_{P} (obtained from the fits of measured data to the Curie-Weiss law 2.2). The figure was previously published also in the diploma work of P. Doležal [62] and Ref. [64]. The colored lines are $H/M(T)$ dependencies calculated from CF parameters determined from neutron scattering data [3]: $\mathrm{B}_2^0 = 0.60$ meV, $\mathrm{B}_4^0 = 0.0302$ meV and $|\mathrm{B}_4^4| = 0.027$ meV.

Specific heat

The specific heat measured on $CePd_2Al_2$ single crystal and its polycrystalline La counterpart is presented in Figure 4.29. The magnetic phase transition at 2.7 K as obtained from magnetization measurement [64] is well reproduced by clear anomaly on specific heat data. The transition temperature obtained by the idealization of the specific heat jump at the phase transition temperature under the constraint of entropy conservation yields $T_{\mathrm{N}} = 2.7(1)$ K. The anomaly is almost unaffected by the application of an external field up to 1 T. Although only a clear shift of T_{N} and magnetic entropy to lower temperatures would serve as a clear indication for the antiferromagnetic order, such behavior might still be consistent with antiferromagnetic ground state. A subtle shift of entropy to higher temperatures in magnetic field of 3 T then probably reflects changes in the magnetic structure with signs of ferromagnetic order in higher fields, in agreement with magnetization measurements (metamagnetic transition was observed around 2 T for [100] direction) [64]. The clearly pronounced anomaly corresponding to the structural phase transition from tetragonal to orthorhombic structure is observed around 13 K. The magnetic field of 3 T has no impact on this anomaly (see Figure 4.29).

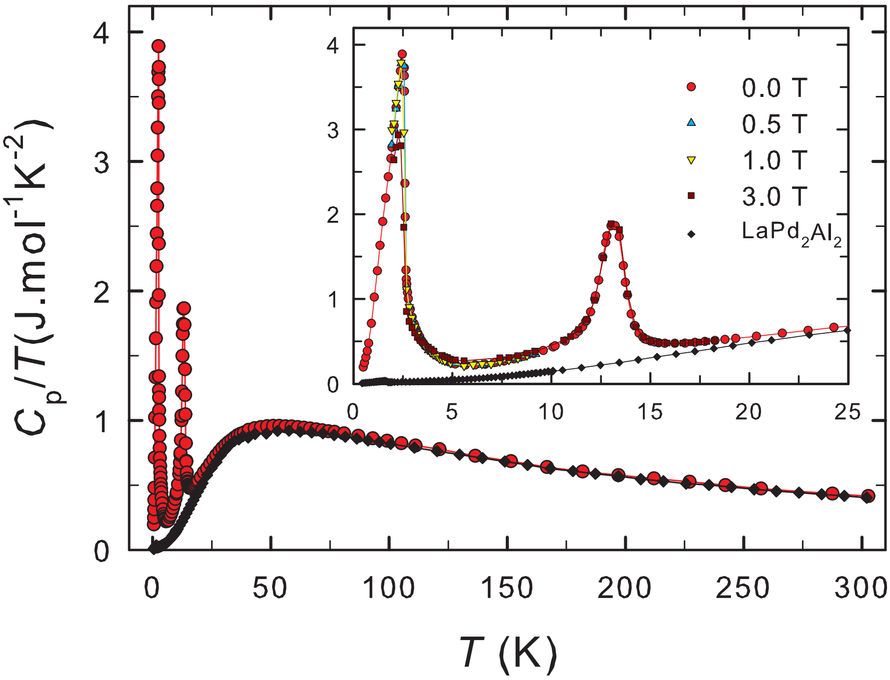

Figure 4.29: The temperature dependence of specific heat in $CePd_2Al_2$ single crystal and $LaPd_2Al_2$ polycrystal. The inset contains the zoomed low-temperature region with the data measured in external magnetic field applied along [100] direction. The figure was previously published also in the diploma work of P. Doležal [62] and Ref. [64].

The total specific heat of $CePd_2Al_2$ is considered to consist of phonon, electronic and magnetic contributions: $C_\mathrm{p} = C_\mathrm{ph} + C_\mathrm{el} + C_\mathrm{mag}$. The isostructural non-magnetic La analogue could be used for a reasonable estimation of the phonon and electronic part of specific heat. The almost perfect overlap of specific heat data for Ce and La counterparts at high temperatures justifies such an approach (see Figures 4.29 and 4.30). However, both compounds undergo the structural phase transition, which brings certain uncertainties in the estimation of C_mag. The structural transition in $LaPd_2Al_2$ around 99 K reveals itself in only very small broad anomaly on specific heat data as discussed in section 4.2.2. On the other hand, the anomaly around 13 K in $CePd_2Al_2$ is well pronounced (see Figure 4.29). We should note, however, that the measurement was done on polycrystalline sample of $LaPd_2Al_2$, whereas single crystal of $CePd_2Al_2$ was measured. The structural transition in $CePd_2Al_2$ is furthermore affected by CF exciton-phonons interaction which involves cerium magnetic degrees of freedom, so it can contribute to the overall magnetic entropy. In Figure 4.31, we show the magnetic entropy obtained as a simple difference between the Ce and La data (i.e. fully including the entropy related to the transition around 13 K) and magnetic entropy obtained when the specific heat corresponding to the anomaly around 13 K is completely subtracted from the Ce data. The two approaches could be considered as a lower and upper limit of the magnetic entropy. The error of estimation

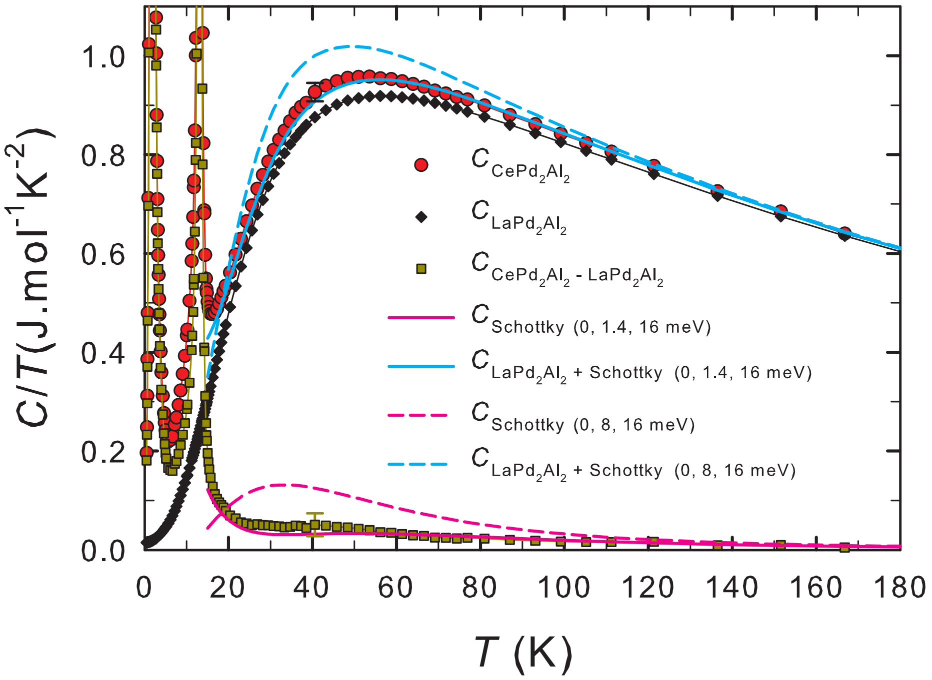

Figure 4.30: The specific heat of $CePd_2Al_2$, $LaPd_2Al_2$, the magnetic contribution to the specific heat for Ce analogue and Schottky contribution to the specific heat. Schottky contribution was calculated from CF splitting energies 0, 1.4 and 16 meV (solid line) and 0, 8 and 16 meV (dashed line) [3]. For illustration, the error bar at 40 K corresponds to 2% error of the heat capacity measurement.

of magnetic specific heat (Figure 4.30) and entropy is also enhanced due to the fact that the La and Ce counterparts have a slightly different crystal structure between 13 and 99 K.

Let us now focus on the magnetic entropy at lowest temperatures which is not affected by any uncertainties related to the structural transition. The values of S_{mag} at the lowest measured temperature of 0.4 K are obtained assuming linear C_{p}/T vs. T dependence below 0.4 K. The magnetic entropy at the ordering temperature, $S_{T_{\mathrm{N}}} = 4.4$ J.mol^{-1}K^{-1}, is significantly lower than R.ln2 expected for a doublet ground state of the Ce^{3+} ion. The value of R.ln2 is reached only around 7 K, see inset of Figure 4.31. Although certain ambiguity of extrapolation of the low-temperature part could lead to a certain error (up to 5%), the reduction of the magnetic entropy at T_{N} seems to originate in a competition of RKKY and Kondo interactions, i.e. Kondo effect exhausts part of the magnetic entropy above the ordering temperature. One can speculate alternatively about the short-range correlations above T_{N}. The $S_{T_{\mathrm{N}}}$ value was used for a rough estimation of Kondo temperature, T_{K}, via equation 4.2: $T_{\mathrm{K}} = 3.4(2)$ K.

Crystal field in $CePd_2Al_2$ - discussion

The vibron state was observed as an additional peak in the inelastic neutron spectra of $CePd_2Al_2$ compound adopting tetragonal structure [3]. Although the theory how to incorporate the vibron states into the calculation of magnetization and heat capacity is, to our knowledge, not developed yet, we can try to test CF

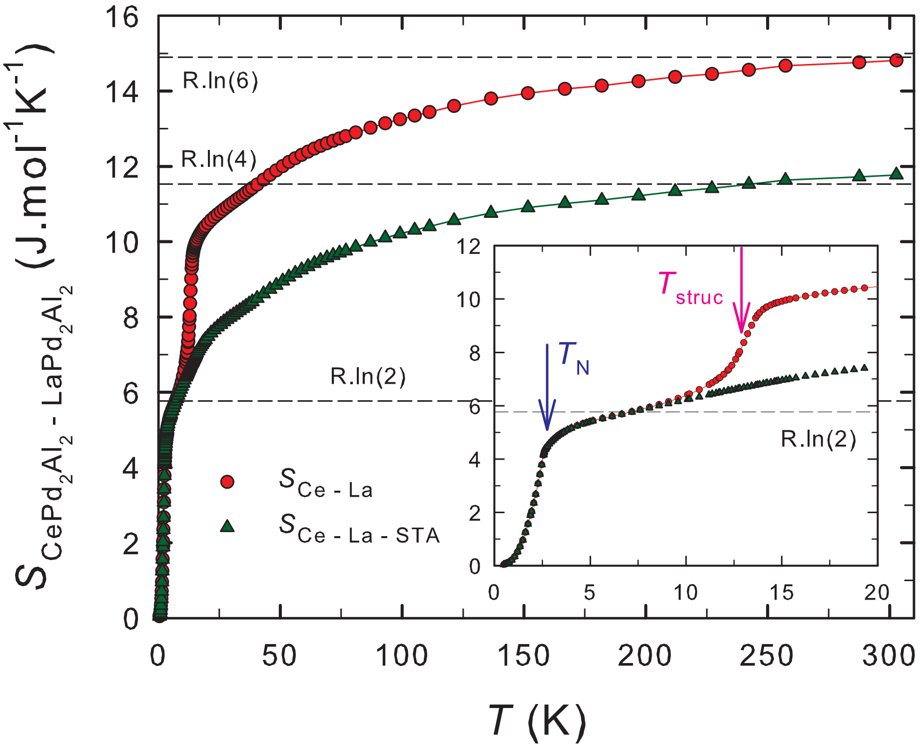

Figure 4.31: The temperature dependence of magnetic entropy determined as simple difference between the Ce and La data ($S_{\mathrm{Ce-La}}$) and with additional subtraction of the specific heat of the structural transition anomaly at T_{struc} ($S_{\mathrm{Ce-La-STA}}$). The inset contains the zoomed low-temperature part of entropy, where the arrows mark the phase transitions as obtained from anomalies on specific heat data.

parameters by comparing with the magnetization and specific heat data without taking into account the influence of vibron state. The measured $H/M(T)$ dependencies in Figure 4.28 are compared to the curves (colored lines corresponding to specific magnetic field directions) calculated using the above given CF parameters. The agreement between the measured data and calculated curves is impressive: not only the mutual anisotropy, but also the magnetization magnitude are in a good agreement. The observed discrepancies at lower temperatures could be tentatively ascribed to the influence of vibron state which is not taken into account during the calculation as well as the influence of structural phase transition.

The magnetic part of specific heat in the paramagnetic region well above the ordering temperature is generally described by Schottky formula and the crystal field splitting of the multiplet ground state. The Schottky contribution above 13 K is calculated from CF splitting energies for tetragonal crystal structure: 0, 1.4, 8 and 16 meV. At lower temperatures the compound adopts already orthorhombic crystal structure, where the CF parameters and also eigenenergies are significantly different, see section 4.2.4. The experimental C_{mag} was compared with the Schottky contribution calculated using the energies of CF levels: 0, 8 and 16 meV. The data are drawn in Figure 4.30. The calculation clearly fails to describe the experimental data, even considering somewhat enhanced error of the magnetic specific heat. Instead, the data are well reproduced when considering energy level at 1.4 meV (with degeneracy 2), see Figure 4.30. The degeneracy of individual levels might be matter of debate. Figure 4.30 shows a simple case with further doublet state at 16 meV and no level at 8 meV. Taking into account only levels at 1.4 and 8 meV leads to much worse agreement (not shown).

4.2.2 Physical properties of $\mathbf{CePd_2(Al,Ga)_2}$ compounds

Crystal structure and structural phase transitions

Polycrystalline $R\mathrm{Pd_2Al_{2-\mathit{x}}Ga_\mathit{x}}$ samples, where $R = \mathrm{Ce}$ and La and where x ranges from 0.0 to 2.0 with a step of 0.4, were prepared by arc-melting of pure elements in a mono-arc furnace under the protection of an argon atmosphere. All the samples were additionally sealed in a quartz glass under pressure of 10^{-4} Pa and annealed for 10 days at 850°C.

To verify the crystal structure and to refine the structural parameters, the X-ray diffraction patterns were recorded at room temperature. The structure parameters were refined by Rietveld analysis using the Fullprof program [11]. The analysis revealed the ordered centrosymmetric tetragonal crystal structure of $\mathrm{CaBe_2Ge_2}$-type (space group 129, P4/nmm) at room temperature for the whole series. The refined lattice parameters are listed in Table 4.7. The stoichiometry and chemical composition of prepared samples were checked subsequently by EDX analysis revealing one phase samples with expected stoichiometries.

The low-temperature X-ray diffraction was used to investigate the structural phase transitions in $\mathrm{(Ce,La)Pd_2Al_{2-\mathit{x}}Ga_\mathit{x}}$ compounds in detail. Detailed description of structure parameters development with temperature is part of the master thesis of Petr Doležal [62] (only in czech language) and our recent publication [111]. We restrict ourself only to the description of found low-T orthorhombic structures (see Figure 4.27) and to the development of structural transition temperatures in $\mathrm{CePd_2Al_{2-\mathit{x}}Ga_\mathit{x}}$ and $\mathrm{LaPd_2Al_{2-\mathit{x}}Ga_\mathit{x}}$ series (see Table 4.7 and Figure 4.32) as it is important for further discussion in section 4.2.4.

The $\mathrm{CePd_2Al_{2-\mathit{x}}Ga_\mathit{x}}$ compounds undergo the structural phase transition from tetragonal $\mathrm{CaBe_2Ge_2}$-type structure to orthorhombic structure (Cmma) in temperature range from 13 to 130 K depending on Al-Ga concentration. Surprisingly, the statement is valid also for $\mathrm{CePd_2Ga_2}$, for which the low-temperature phase was identified as the triclinic structure by Kitagawa et al. [109]. Nevertheless, the low-temperature lattice parameters in $\mathrm{CePd_2Ga_2}$ and in the rest of the series differ significantly, what leads us to labels: orthorhombic I and orthorhombic II structure for $x < 2$ and $x = 2$, respectively. The lattice parameters a and b differ only slightly in the case of orthorhombic I structure. Their values are very close to the length of a basal plane diagonal of tetragonal structure (see Figure 4.27), i.e. $a_\mathrm{orth} \approx b_\mathrm{orth} = \sqrt{2}a_\mathrm{tetr}$. Orthorhombic II structure then reveals more pronounced difference between parameters a and b. The orthorhombic I and II structures are isostructural, nevertheless, the Al-Ga substitution does not lead to the transition between them. One can rather suppose a formation of one of them, while the other wears off. Intervals of coexistence could be traced. For more details see Ref. [111]. Ce and La counterparts undergo the same type of structural transition.

The concentration dependencies of the structural phase transition temperature, T_struc, in $\mathrm{CePd_2Al_{2-\mathit{x}}Ga_\mathit{x}}$ and $\mathrm{LaPd_2Al_{2-\mathit{x}}Ga_\mathit{x}}$ compounds (as determined

Table 4.7: Basic structural and magnetic properties of (Ce,La)$Pd_2Al_{2-x}Ga_x$ compounds. The lattice parameters a and c at room temperature as determined by Fullprof program [11]. The agreement factors of the fit to data were < 12% in all compounds. The effective magnetic moment μ_{eff} and paramagnetic Curie temperature θ_{p} as determined from H/M vs T dependencies. Néel temperature T_{N} was obtained from magnetization and electrical resistivity measurements. Moreover, structural phase transition temperatures of $CePd_2Al_{2-x}Ga_x$ compounds, $T_{\mathrm{struc}}^{\mathrm{Ce}}$, and their lanthanum analogues, $T_{\mathrm{struc}}^{\mathrm{La}}$, as obtained from electrical resistivity measurements are presented. T^* is a parameter that represents inter alia the strength of ferromagnetic correlations in a given compound obtained from MR measurements.

x	a (pm)	c (pm)	T_{struc} (K)	μ_{eff} (μ_{B})	θ_{p} (K)	$T_{\mathrm{N}}^{\mathrm{mag}}$ (K)	$T_{\mathrm{N}}^{\mathrm{res}}$ (K)	T^* (K)
$CePd_2Al_{2-x}Ga_x$			$T_{\mathrm{struc}}^{\mathrm{Ce}}$					
0.0	441.5(3)	987.4(6)	13.5(9)	2.55(2)	-12.8(3)	2.8(1)	2.7(1)	2.0(5)
0.4	441.3(4)	990.2(8)	15.4(9)	2.52(2)	-13.2(3)		2.6(1)	3.0(5)
0.8	441.4(3)	987.0(6)	15.6(9)	2.53(2)	-13.0(3)	2.5(1)	2.5(1)	2.0(5)
1.2	441.5(3)	985.2(6)	62(7)	2.53(2)	-14.8(3)	2.4(1)	2.4(1)	1.0(5)
1.6	441.8(5)	983.5(9)	88(8)	2.61(2)	-17.5(3)	2.3(1)	2.4(1)	0.5(4)
2.0	442.5(4)	984.5(7)	126(7)	2.56(2)	-15.5(3)	2.2(1)	2.3(1)	0.0(4)
$LaPd_2Al_{2-x}Ga_x$			$T_{\mathrm{struc}}^{\mathrm{La}}$					
0.0	444.4(3)	989.9(6)	99.1(5)					
0.4	444.4(3)	989.6(7)	96.1(5)					
0.8	444.4(4)	988.2(9)	88.9(5)					
1.2	444.7(5)	987.1(9)	70.3(5)					
1.6	444.7(4)	985.4(8)	69.0(5)					
2.0	444.6(3)	985.2(7)	64.1(5)					

from electrical resistivity measurement, in good agreement with low-T X-ray diffraction data) are presented in Figure 4.32. The concentration development of structural transition temperature is very different in these two series. $T_{\mathrm{struc}}^{\mathrm{La}}$ shows a smooth weak decrease with increasing Ga content. In contrast, $T_{\mathrm{struc}}^{\mathrm{Ce}}$ remains almost unchanged between $x = 0.0$ and $x = 0.8$ and starts to increase strongly with further increase of Ga content. The concentration region $x \in (0.8, 1.2)$ coincides with the change of the character of the transition. Well pronounced transitions can be traced on electrical resistivity and specific heat data for $x \geq 1.2$).

Another point, which should be discussed, is a relation between the observed structural properties and occurrence of the vibron states in these compounds. The comparison of structural transition temperatures in the Ce- and La-based compounds shows $T_{\mathrm{struc}}^{\mathrm{Ce}} < T_{\mathrm{struc}}^{\mathrm{La}}$ for RPd_2Al_2 system and in contrast $T_{\mathrm{struc}}^{\mathrm{Ce}} > T_{\mathrm{struc}}^{\mathrm{La}}$ for RPd_2Ga_2 system. This observation was tentatively attributed to the occurrence of the vibron state in $CePd_2Al_2$ which stabilizes the tetragonal structure [3]. Following the concentration dependence of structural transition temperatures in the $RPd_2Al_{2-x}Ga_x$ series (see Table 4.7 and Figure 4.32), one can draw a very tentative hypothesis: the strong electron-phonon interaction resulting in vibron

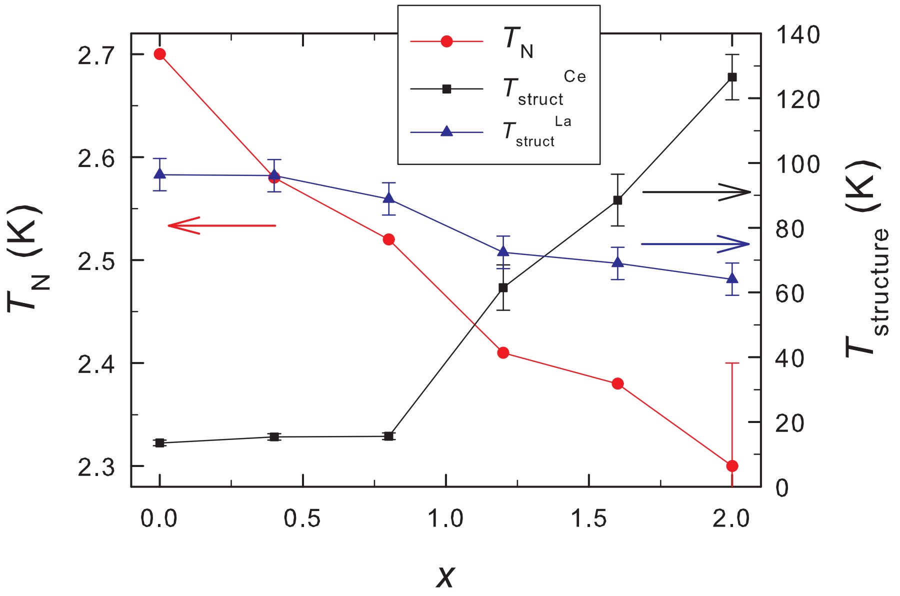

Figure 4.32: The temperatures of magnetic and structural phase transitions in $CePd_2Al_{2-x}Ga_x$ compounds and its La analogues. The error bars for value of T_N are shown only for $x = 2.0$ for better lucidity. See also Table 4.7.

states is present in compounds with $x < 0.8$, where T^{Ce}_{struc} is clearly lower than T^{La}_{struc}, the strength of interaction decreases in concentration interval $x \in (0.8, 1.2\rangle$ and for $x > 1.2$ there are no vibrons. Such a hypothesis is corroborated by our inelastic neutron scattering experiment on selected compounds from studied series (see section 4.2.4).

Magnetization measurement

In the paramagnetic region, the temperature dependencies of magnetization follow the Curie-Weiss law in all the series. The obtained effective magnetic moment, μ_{eff}, is very close to the Ce^{3+} free ion value of 2.54 μ_B, in the whole series. The negative paramagnetic Curie temperature, θ_p, indicates antiferromagnetic ground state in these compounds. Parameters obtained by the fit are given in Table 4.7.

At low temperatures, a maximum in $M(T)$ dependencies is observed for both zero-field cooled and field-cooled regimes pointing to antiferromagnetic ordering. The Néel temperatures, T_N, determined as maxima of $M(T)$ curves, are summarized in Table 4.7. We observe decrease of T_N with increasing Ga content, see Figure 4.32.

The magnetic field dependence of magnetization in Figure 4.33 reveals the metamagnetic phase transition around 1.2 T for all $CePd_2Al_{2-x}Ga_x$ compounds. The Arrot plot, shown in Figure 4.34, shows the behavior expected for antiferromagnetic materials. However, one can observe a clear trend indicating probably stronger ferromagnetic correlations with increasing Ga content.

Specific heat

The specific heat of intermetallic compound can be generally described as a sum of contributions: $C_p = C_{el} + C_{ph} + C_{mag}$. The usual approach to estimate contribu-

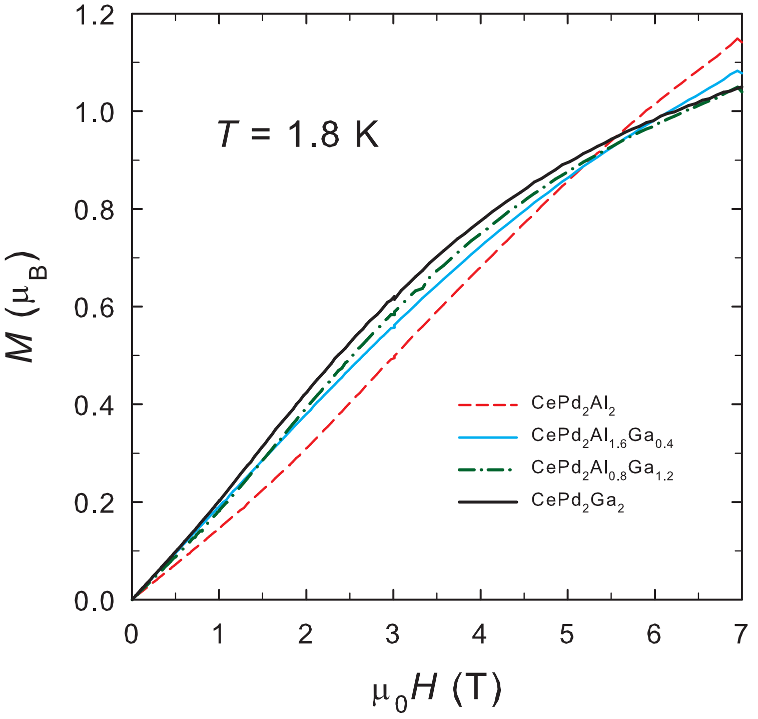

Figure 4.33: The magnetic field dependence of magnetization for $\mathrm{CePd_2Al_{2-x}Ga_x}$ compounds. The curves for x = 0, 0.4, 1.2 and 2 are showed only, for better lucidity.

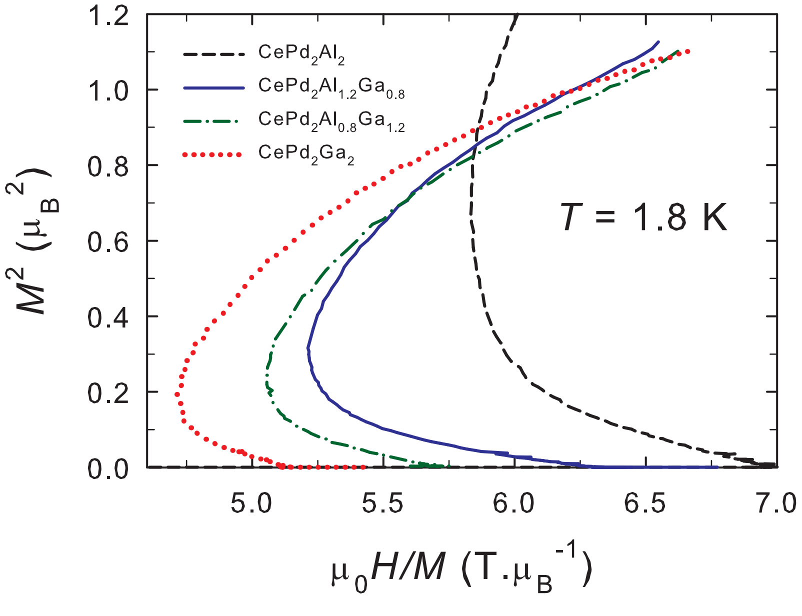

Figure 4.34: Arrot plots of selected $\mathrm{CePd_2Al_{2-x}Ga_x}$ compounds. The remaining compounds follow the same trend (not shown for better lucidity).

tions of $C_{\mathrm{el}} + C_{\mathrm{ph}}$ by measurement of non-magnetic analogue (to obtain magnetic part of specific heat for studied magnetic material) is quite problematic in the case of $\mathrm{CePd_2}X_2$ compounds. Both studied $\mathrm{CePd_2}X_2$ and $\mathrm{LaPd_2}X_2$ analogues undergo the structural phase transition from tetragonal to orthorhombic structure [111]. Moreover, the superconducting transition was observed in all La counterparts [65]. All these transitions are accompanied by relatively large anomalies, what leads to quite rough estimation of C_{mag} even in higher temperature region. Nevertheless, the value of specific heat of La analogues at temperatures lower than 6 K is almost negligible compared to Ce counterparts, for which reason we can estimate C_{mag} with only a minor error.

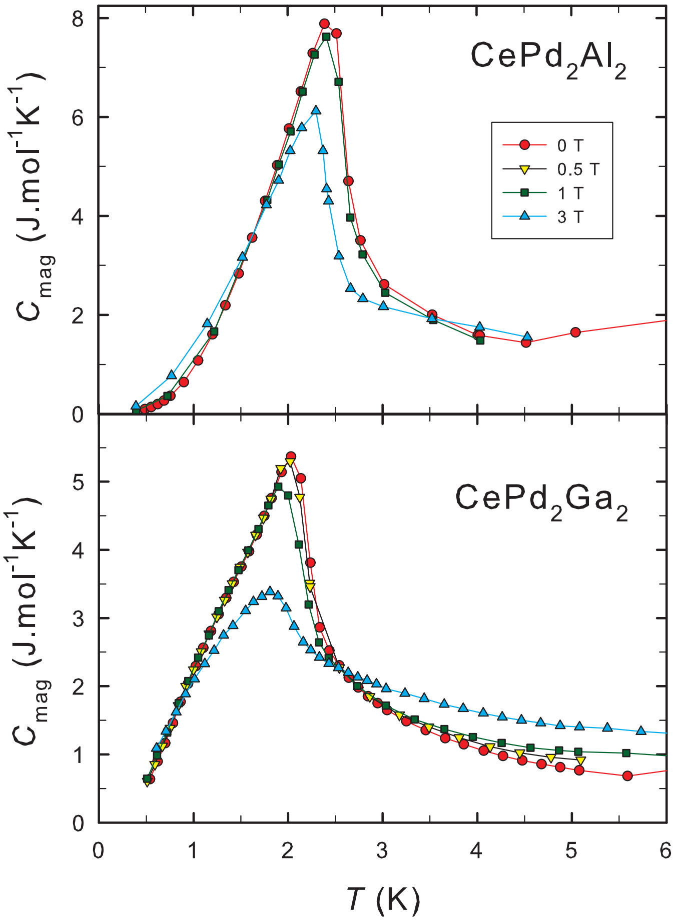

Figure 4.35: The magnetic part of specific heat C_{mag} vs. T in low-temperature region of CePd$_2X_2$ compounds. The development with applied magnetic field is demonstrated as well.

The temperature dependencies of specific heat of $\mathrm{CePd_2Al_2}$ and $\mathrm{CePd_2Ga_2}$ are presented in Figure 4.35. Here, we observe a clear anomaly indicating transition to a magnetically ordered state. The idealization of the specific heat jump at the phase transition temperature under the constraint of entropy conservation yields the T_{N} values 2.7(2) K and 2.2(2) K for $\mathrm{CePd_2Al_2}$ and $\mathrm{CePd_2Ga_2}$, respectively, in good agreement with magnetization measurements (see Table 4.7). The effect of external magnetic field on specific heat is presented in Figure 4.35. The specific heat data of both parent compounds point clearly to the antiferromagnetic ground state as there is no shift of entropy to higher temperatures in applied field up to 1 T. In magnetic field of 3 T, the shift of the entropy to higher temperatures is observed, which could illustrate the field induced transition to ferromagnetic state. Such a behavior is in good agreement with magnetization measurement. One can observe quite different anomalies at ordering temperature for $\mathrm{CePd_2Al_2}$

and $CePd_2Ga_2$. The latter compound exhibits less intense and broader anomaly than the former one. Such a difference for isoelectronic compounds might be ascribed to different structure parameters in low-temperature region. Another explanation could be a competing Kondo interaction, which has more significant impact on $CePd_2Ga_2$. The low-temperature gamma coefficient of $CePd_2Al_2$ is presumably lower than 0.1 $J.mol^{-1}K^{-2}$, the value in $CePd_2Ga_2$ cannot be reasonably estimated from data above 0.4 K. The measurement to temperatures lower than 0.4 K is needed to find proper value in both cases.

The magnetic entropy, S_{mag}, was evaluated from measured specific heat data and is displayed in Figure 4.36. The magnetic entropy at the ordering temperature, $S_{T_{\mathrm{N}}} = 4.1$ and 4.2 J $mol^{-1}K^{-1}$ for $CePd_2Al_2$ and $CePd_2Ga_2$, respectively, is significantly lower than R.ln2 expected for a doublet ground state of the Ce^{3+} ion. A certain ambiguity of extrapolating the low-temperature part of specific heat could be estimated to an error up to 10%. The value of R.ln2 is reached just around 6 - 7 K. The reduction of the magnetic entropy at T_{N} could be ascribed to a competing Kondo effect causing an exhaustion of a part of the magnetic entropy above the ordering temperature. One can speculate alternatively about the short range correlations above T_{N}. The rough estimation of Kondo temperature could be done using equation 4.2 leading to $T_{\mathrm{K}} = 3.8$ K and 3.0 K for $CePd_2Al_2$ and $CePd_2Ga_2$, respectively. T_{K} decreases with increasing Ga content, i.e. with increasing volume of the unit cell (see Table 4.7).

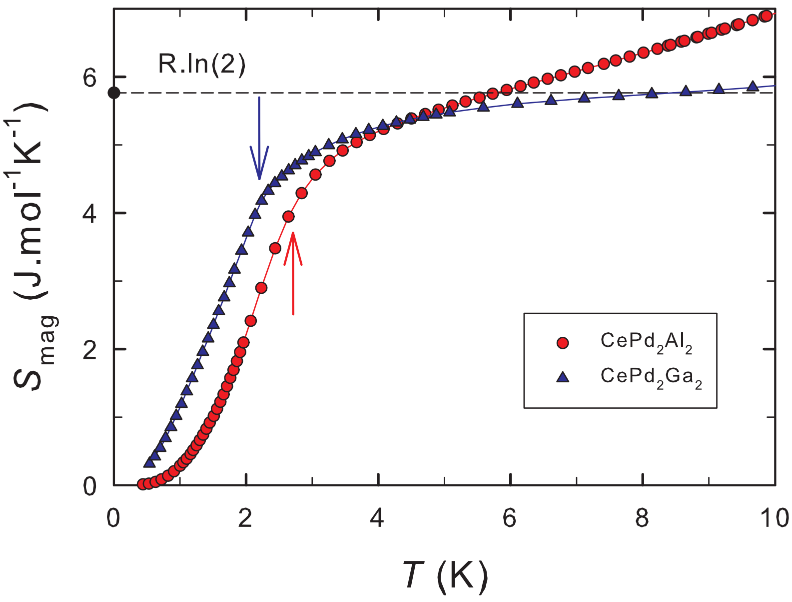

Figure 4.36: The magnetic entropy in $CePd_2Al_2$ and $CePd_2Ga_2$. The value of R.ln2 is drawn as dashed line. The arrows mark the temperature of transition to antiferromagnetic state determined from electrical resistivity measurements.

The phase transitions from tetragonal to orthorhombic structure around 13.5 K and 127 K in $CePd_2Al_2$ and $CePd_2Ga_2$, respectively, are well illustrated on specific heat data, see Figure 4.37. The transition temperatures are well in agreement with our recent electrical resistivity measurements (see following subsection) as well as with the powder X-ray diffraction experiment. The specific heat data of La

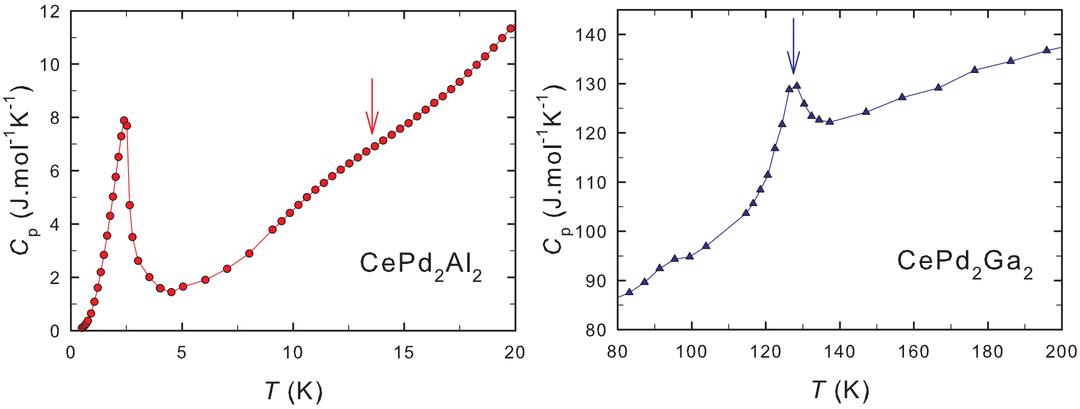

Figure 4.37: The temperature development of specific heat around the structural phase transition in CePd$_2X_2$ compounds. The arrows mark the structural phase transition temperatures obtained by electrical resistivity measurements, see Table 4.7.

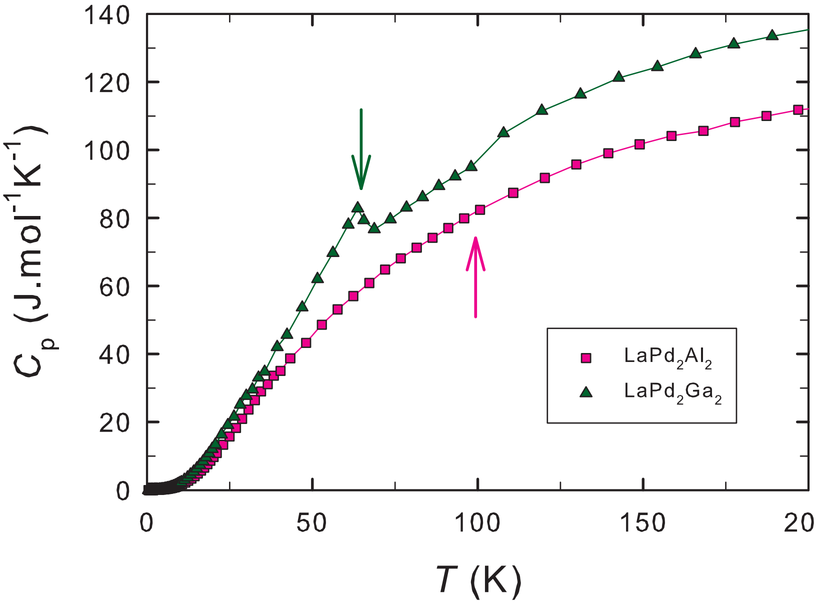

Figure 4.38: The specific heat of LaPd$_2X_2$ compounds. The arrows mark the structural phase transition temperatures obtained by electrical resistivity measurements, see Table 4.7.

counterparts are shown in Figure 4.38. Here, one can observe, that the structural phase transition is bounded with well pronounced anomaly on specific heat data in the case of LaPd$_2$Ga$_2$, whereas LaPd$_2$Al$_2$ reveals almost no sign of structural transition. The transition from tetragonal to orthorhombic II structure reveals itself in pronounced anomalies on electrical resistivity and specific heat data. On the other hand, the transition to orthorhombic I structure is connected with only a weak anomaly on polycrystalline sample (compare with single crystal specific heat data in Figures 4.29 and 4.30). The Schottky specific heat calculated for the whole CePd$_2$(Al,Ga)$_2$ series is presented and discussed in section 4.2.4.

Electrical resistivity

The electrical resistivity data on $CePd_2Al_{2-x}Ga_x$ and $LaPd_2Al_{2-x}Ga_x$ compounds are presented in Figures 4.39 and 4.40. The structural transition from tetragonal to orthorhombic structure is traced as a clear anomaly for $LaPd_2Ga_2$ and several Ga rich $CePd_2Al_{2-x}Ga_x$ ($x \geq 1.2$) compounds. In the remaining compounds, the transition is much less pronounced, nevertheless, it can be revealed when inspecting the first derivative of $R(T)$. The data for $CePd_2Al_2$ and $LaPd_2Al_2$ are shown as an example in insets of Figures 4.39 and 4.40. Although the anomalies are relatively weak, they well correspond to the temperatures of the structural transition as known from low-temperature X-ray diffraction study [111]. One can tentatively conclude that the well pronounced anomaly in $R(T)$ corresponds to transition from tetragonal to orthorhombic II structure, whereas transition between tetragonal and orthorhombic I structure does not lead to any significant effect on resistivity curves.

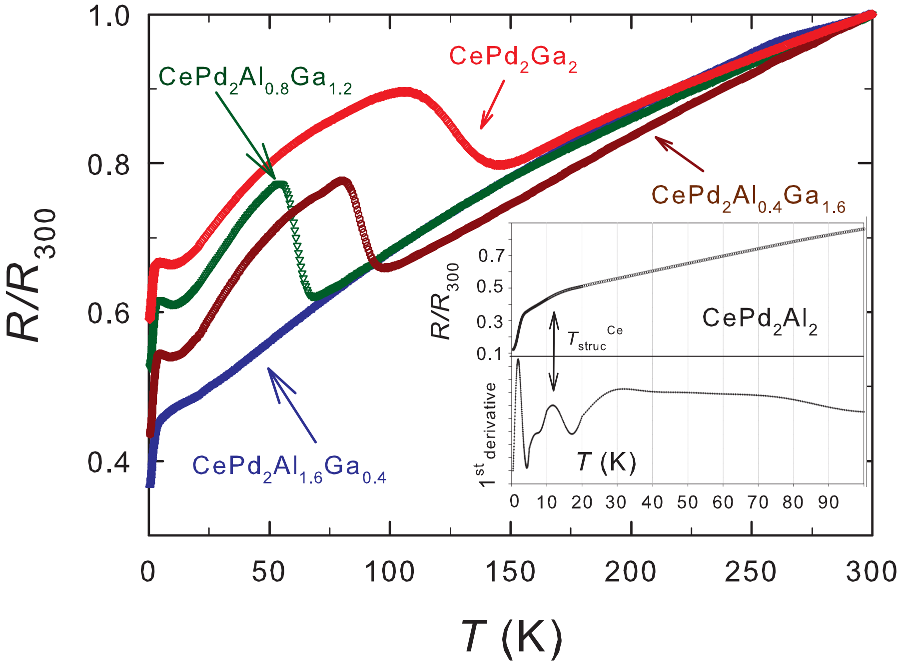

Figure 4.39: The temperature dependence of electrical resistivity. The anomaly corresponding to structural phase transition is clearly visible for $x = 1.2$, 1.6 and 2. The inset contains the first derivative of $R(T)$ for $CePd_2Al_2$. The arrow indicates temperature of structural phase transition.

The anomaly corresponding to the antiferromagnetic phase transition is observed in Figures 4.41 and 4.42. The application of magnetic field has no significant impact on T_N. The values of Néel temperature obtained from first derivative are listed in Table 4.7 and well correspond to the values obtained from magnetization and specific heat measurements. The magnetic field influences the electrical resistivity in similar way in all measured compounds. Pronounced anomaly corresponding to the Kondo interaction or fluctuations associated with the antiferromagnetic ordering, as speculated in Ref. [109], is observed in the Ga rich compounds around 4 - 5 K, see Figure 4.42 as an example.

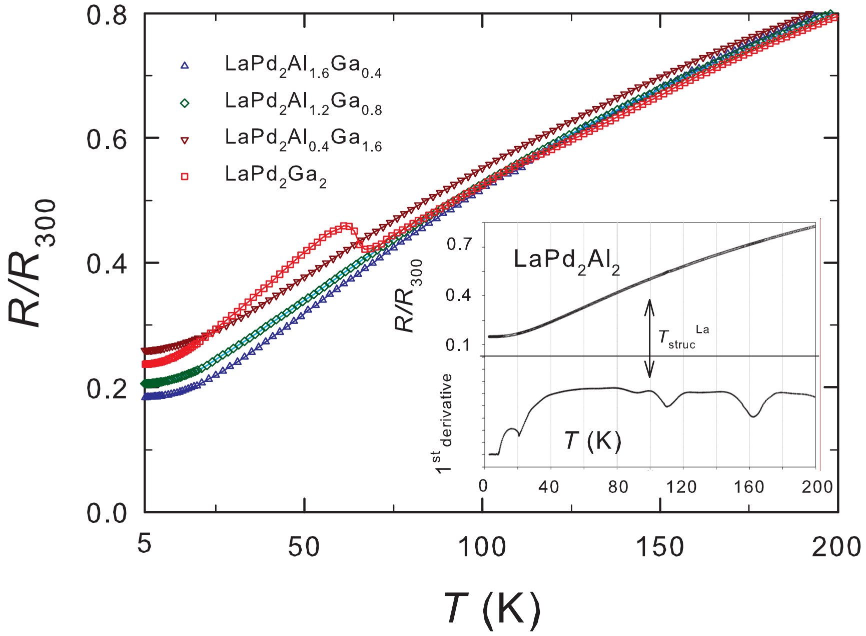

Figure 4.40: The electrical resistivity of $LaPd_2Al_{2-x}Ga_x$ compounds. The inset contains the first derivative of $R(T)$ of $LaPd_2Al_2$. See also Table 4.7. The arrow indicates temperature of structural phase transition.

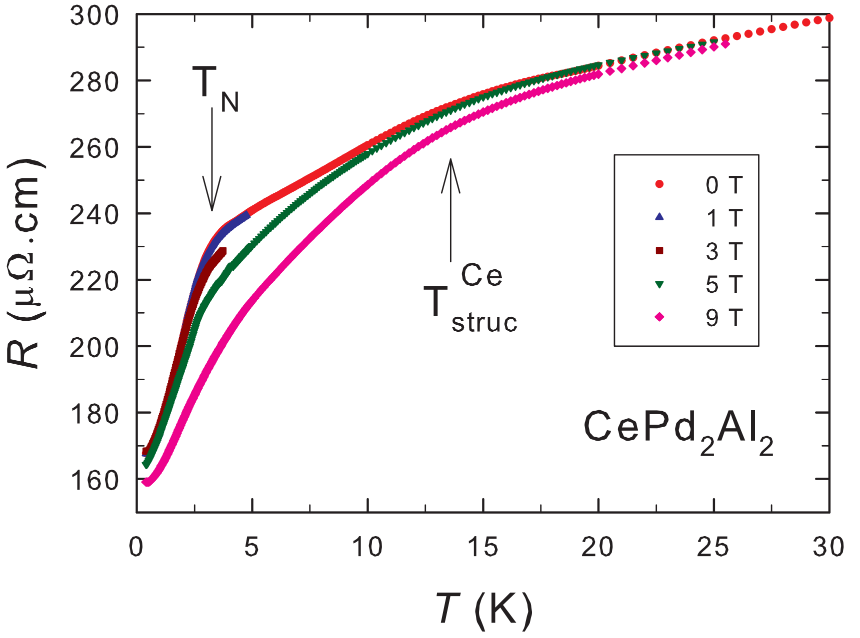

Figure 4.41: The electrical resistivity of $CePd_2Al_2$ in static magnetic field. The anomaly at low temperature region corresponds to the antiferromagnetic phase transition, the anomaly at 13.5 K then corresponds to the structural phase transition.

The magnetoresistivity (MR) measurements reveal quite similar behavior in the whole series (see e.g. $CePd_2Ga_2$ in Figure 4.43). Negative MR is observed in the paramagnetic region. In the ordered state below T_N, the behavior is more

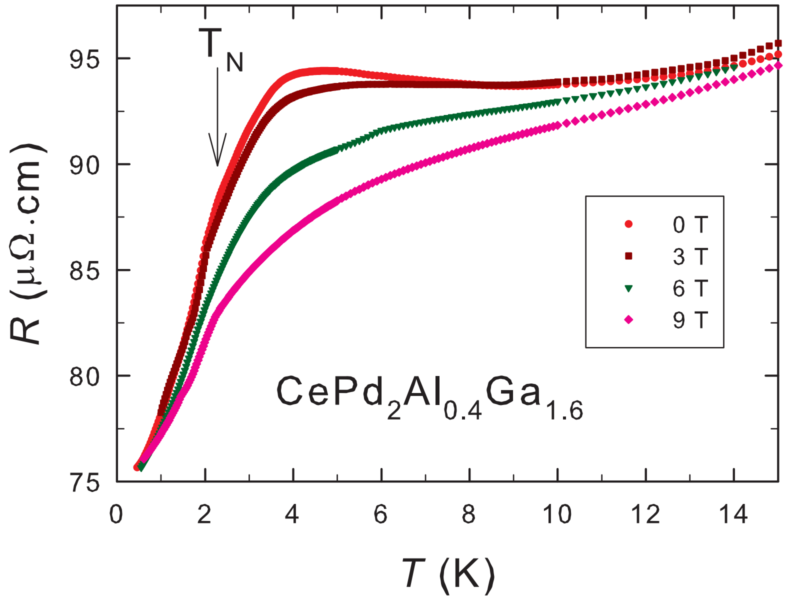

Figure 4.42: The electrical resistivity of CePd$_2$Al$_{0.4}$Ga$_{1.6}$ in static magnetic field. The anomaly at low temperature region corresponds to the antiferromagnetic phase transition.

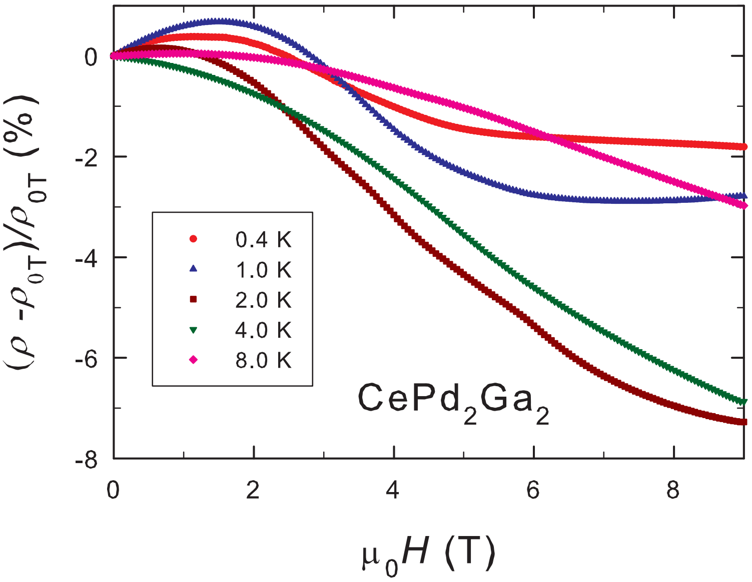

Figure 4.43: The magnetoresistance (MR $= \frac{\rho(H,T)-\rho(0,T)}{\rho(0,T)}$) measurement at several temperatures below and above magnetic phase transition in CePd$_2$Ga$_2$.

complex: the resistivity first starts to increase with applied field up to 1 - 3 T and then decreases with further field increase. Such a behavior could suggest the presence of a strong magnetic correlations between $4f$ moments, what leads to the induced ferromagnetic order as was found in YbNiAl$_2$ [85], for instance. Another explanation could be a suppression of the Kondo scattering with increasing field.

Figure 4.44 was obtained by following the single-ion Kondo model with Bethe-ansatz studies [87]. The x-axis is rescaled as $\frac{\mu_0 H}{T+T^*}$. In the CePd$_2$Al$_{2-x}$Ga$_x$ series,

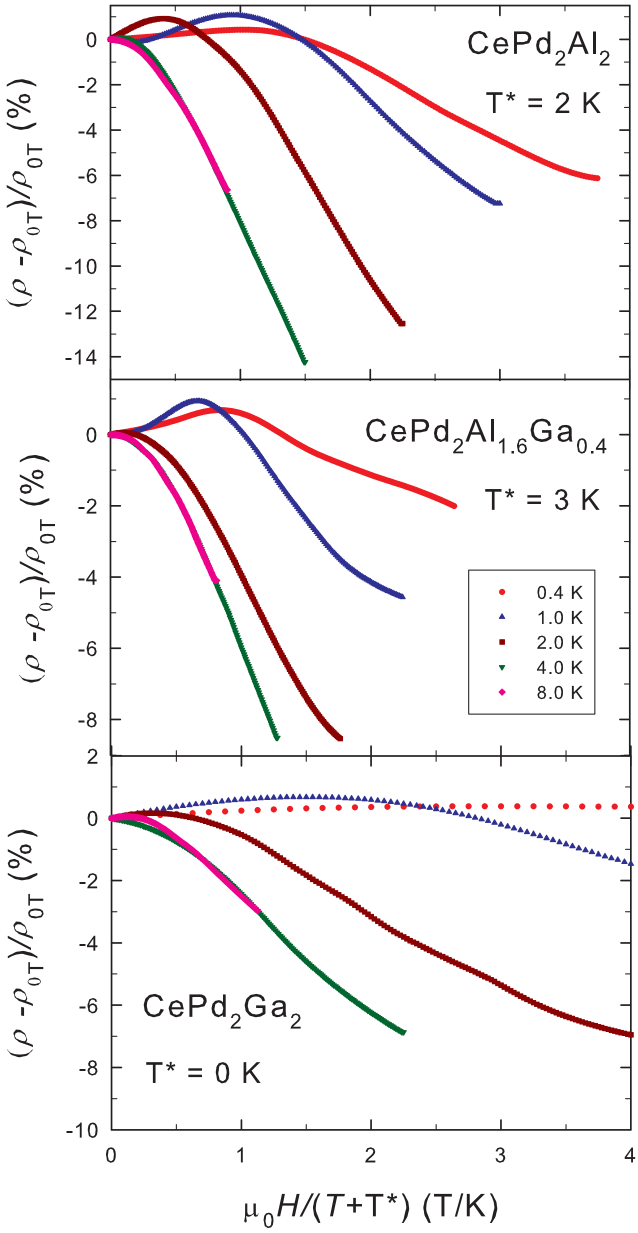

Figure 4.44: The magnetoresistance (MR $= \frac{\rho(H,T)-\rho(0,T)}{\rho(0,T)}$) in dependence of $\frac{\mu_0 H}{T+T^*}$ at several temperatures below and above magnetic phase transition in CePd$_2$Al$_2$, CePd$_2$Al$_{1.6}$Ga$_{0.4}$ and CePd$_2$Ga$_2$ compounds. See text for more details.

T^* slightly increases from parent compound to $x = 0.4$ and then slowly decreases with increasing x (see Table 4.7). The ferromagnetic correlations (i.e. the lowest T^* values) are then expected in parent CePd$_2$Ga$_2$, where $T^* = (0.0 \pm 0.4)$ K. These ferromagnetic correlations in Ga rich compounds are in agreement with magnetization measurements.

4.2.3 Magnetic structures of $CePd_2Al_2$ and $CePd_2Ga_2$

The magnetic structures in $CePd_2Al_2$ and $CePd_2Ga_2$ were studied by means of powder neutron diffraction employing D1B diffractometer at ILL, Grenoble. Measured diffraction patterns are presented in Figures 4.45 and 4.46. A comparison of diffraction patterns taken in paramagnetic and ordered state (at temperatures 5 K and 1.5 K, respectively) reveals several (about ten) clear peaks of magnetic origin for each compound. We note, that the most intensive magnetic peak in diffraction patterns of $CePd_2Ga_2$ corresponds to the only one magnetic reflection found by our former neutron diffraction experiment using E6 diffractometer at HZB, Berlin. [113] We remind the reader, that the low-temperature crystal structure of $CePd_2Ga_2$ is orthorhombic of Cmma-type (see Figure 4.27 for illustration) [111]. The structure parameters determined at $T = 5$ K are listed in Table 4.8.

Table 4.8: The lattice parameters and atomic positions of $CePd_2Al_{2-x}Ga_x$ compounds as determined from neutron diffraction data measured at 5 K.

	$CePd_2Al_2$	$CePd_2Ga_2$
a (Å)	6.269(1)	6.397(1)
b (Å)	6.130(1)	5.945(1)
c (Å)	9.885(2)	9.906(2)
z_{Ce}	0.758(1)	0.764(1)
z_{Pd}	0.371(1)	0.384(1)
$z_{\mathrm{Al(Ga)}}$	0.120(1)	0.133(1)

Compared to previous E6 study [113], the measurement using D1B diffractometer led to the observation of clear magnetic peaks allowing an unambiguous determination of magnetic propagation vectors, as well as complete magnetic structures in both studied compounds. The observed magnetic peaks in $CePd_2Al_2$ are described by an incommensurate propagation vector $\vec{k} = (0.06, 0.54, 0)$, while two commensurate magnetic propagation vectors, $\vec{k_1} = (\frac{1}{2}, \frac{1}{2}, 0)$ and $\vec{k_2} = (0, \frac{1}{2}, 0)$ - together with -$\vec{k_2}$ ($\vec{k_2} \neq$ -$\vec{k_2}$) - are necessary to describe the magnetic structure of $CePd_2Ga_2$. The positions of magnetic reflections are marked in Figures 4.45 and 4.46, respectively. Here, we should compare the found $\vec{k_2} = (0, \frac{1}{2}, 0)$ propagation vector describing the strongest magnetic reflection in $CePd_2Ga_2$ with the vectors suggested by our former measurement (only one magnetic peak observed) [113]. Propagation vector $\vec{k_2}$ in orthorhombic structure corresponds well to $(\frac{1}{4}, \frac{1}{4}, 0)$ vector in triclinic description as suggested by our former study [113]. Both diffraction studies are thus fully consistent.

The determined magnetic propagation vectors and known structure parameters allow to calculate the possible magnetic structures by performing a thorough representation analysis employing the programs BasIreps [11] and MaxMagn [117]. The analysis revealed that the maximal magnetic subgroups of Cmma (space group 67) described by propagation vector $\vec{k_1}$ are only two: monoclinic P_a2 (3) and triclinic $P_S\overline{1}$ (2). The magnetic moments in former subgroup are arranged within the basal plane for Ce on monoclinic crystallographic sites $(0, \frac{1}{8}, z_{\mathrm{Ce}})$, whereas moments on sites $(0, \frac{3}{8}, -z_{\mathrm{Ce}})$ point along the orthorhombic

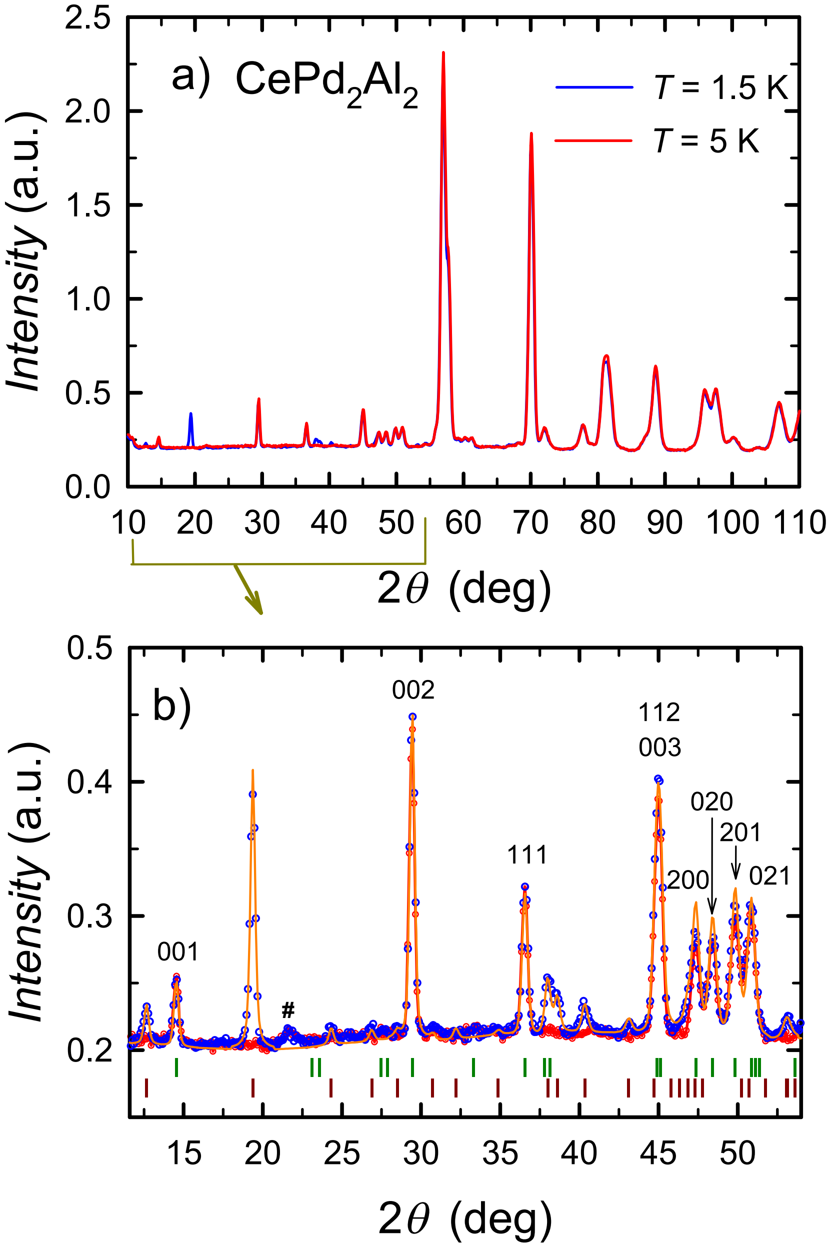

Figure 4.45: The powder neutron diffraction patterns of CePd$_2$Al$_2$ taken at 1.5 K and 5 K using D1B diffractometer at ILL, Grenoble. Panel (b) shows zoomed low-angle region. The full orange line represents the fit done using Fullprof program [11]. Vertical bars under plot mark the positions of nuclear (green) and magnetic ($\vec{k}$ = (0.06, 0.54, 0), dark red) Bragg reflections. The symbol # labels the peak of foreign phase, which is not of magnetic origin.

c-axis. The triclinic subgroup allows any direction of magnetic moments in space.

The investigation of maximal magnetic subgroups of Cmma described by $\vec{k_2}$ leads to 8 space groups with orthorhombic symmetry: P_bmmn (59), P_cbcm (57), P_acca (54), P_cmna (53), P_amna (53), P_amma (51), P_aban (50) and P_accm (49). These subgroups can be divided into 4 classes according to their magnetic moments arrangement. The subgroups P_bmmn (59) and P_amma (51) dictate two different Ce atomic sites (0, $\frac{1}{8}$, z_{Ce}) and (0, $\frac{3}{8}$, $-z_{\mathrm{Ce}}$) with magnetic moments along

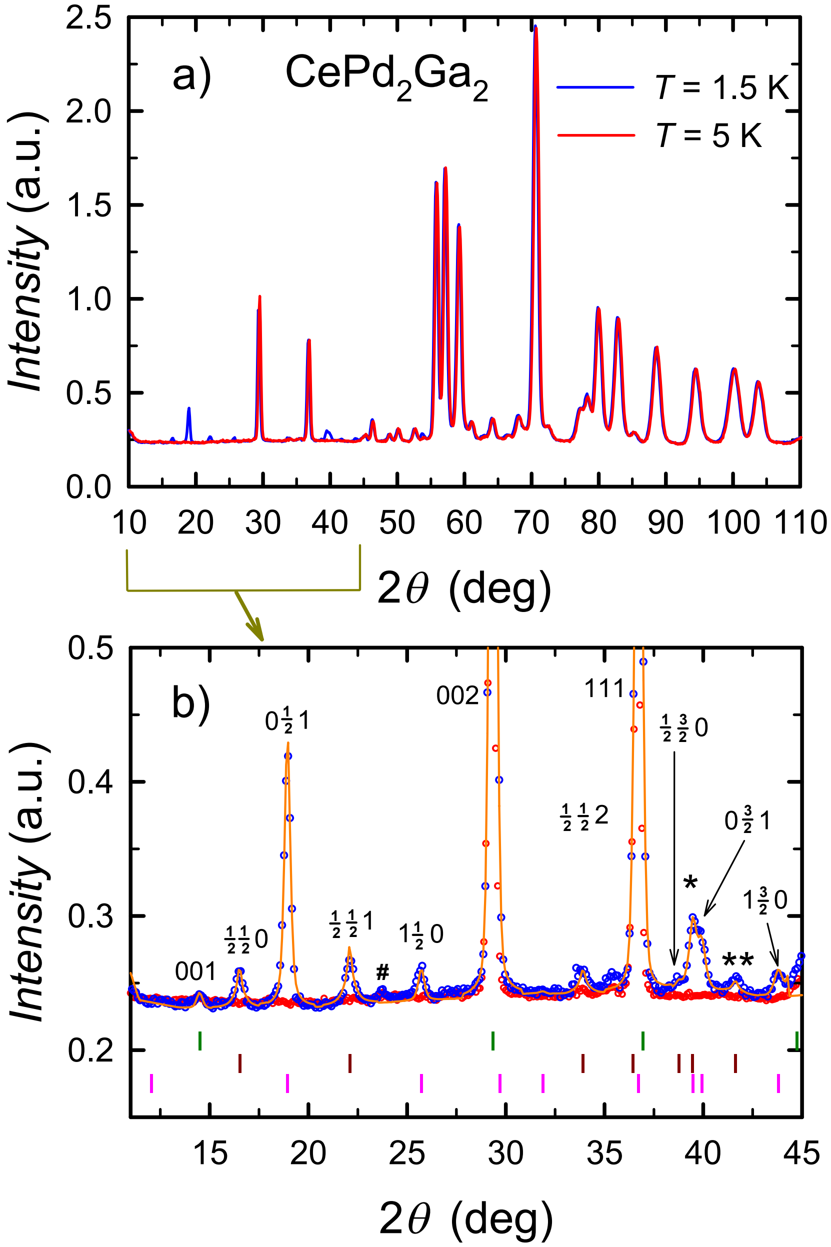

Figure 4.46: The powder neutron diffraction patterns of $CePd_2Ga_2$ taken at 1.5 K and 5 K using D1B diffractometer at ILL, Grenoble. Panel (b) shows zoomed low-angle region. The full orange line represents the fit done using Fullprof program [11]. Vertical bars under plot mark the positions of nuclear (green) and magnetic Bragg reflections (dark red for $\vec{k_1} = (\frac{1}{2}, \frac{1}{2}, 0)$ and pink for $\vec{k_2} = (0, \frac{1}{2}, 0)$). The symbol # labels the peak of foreign phase, which is not of magnetic origin. All pronounced reflections are labelled; symbol '*' corresponds to the peak bounded with magnetic reflections $(\frac{3}{2}\ \frac{1}{2}\ 1)$ and $(1\ \frac{1}{2}\ 2)$; symbol '**' stays for the magnetic reflection $(\frac{1}{2}\ \frac{3}{2}\ 1)$.

the a-axis and with zero moments, respectively. The two same atomic sites are found also in subgroups P_cbcm (57) and P_amna (53), but the magnetic moments point along the c-axis and along the b-axis, respectively. Third class consists from subgroups P_acca (54) and P_aban (50) with magnetic moments arranged in the bc-plane. The subgroups P_cmna (53) and P_accm (49) then allow the magnetic moments aligned along the a-axis.

We utilized the calculated magnetic structures in the fitting process of measured diffraction patterns leading to a determination of magnetic structures in both $CePd_2Al_2$ (for the fit, we used maximal magnetic subgroups obtained for $\vec{k_2} = (0, \frac{1}{2}, 0)$) and $CePd_2Ga_2$, although the number of observed magnetic peaks leaves a certain freedom in the absolute magnetic moments direction.

The magnetic moments in $CePd_2Al_2$ are described by a propagation vector $\vec{k} = (0.06, 0.54, 0)$ and form an incommensurate amplitude modulated magnetic structure. The maximum magnetic moment size approaches 2.05(4) μ_B/Ce^{3+}, still slightly lower value than the magnetic moment of Ce^{3+} free ion. The magnetic moments are aligned along one direction which is close to orthorhombic a-axis. The agreement factor $R_m = 19.0\%$ for pure a-axis direction of magnetic moments (maximal magnetic subgroups P_cmna (53) and P_accm (49)) is improved ($R_m = 13.9\%$) considering 4° and 24° tilt towards b- and c-axis, respectively. Such a tilt out of [100] is not forbidden by symmetry as the magnetic structure of $CePd_2Al_2$ is described by $\vec{k} = (0.06, 0.54, 0)$. The fit of determined magnetic structure to the measured data is presented in Figure 4.45.

The magnetic moments belonging to each (of two) component in $CePd_2Ga_2$ are aligned along one direction and order antiferromagneticaly within planes stacked along c-axis. The moments direction is close to the orthorhombic a-axis for both components, similarly as in $CePd_2Al_2$. Pure a-axis direction of magnetic moments leads to the agreement factors $R_{m1} = 16.3\%$ and $R_{m2} = 7.4\%$ for components of magnetic moment described by $\vec{k_1}$ and $\vec{k_2}$, respectively. The best agreement was obtained for magnetic moments direction 4° and 14° away from the a-axis to the b- and c-axis directions, respectively ($R_{m1} = 13.0\%$ and $R_{m2} = 6.5\%$). Such a magnetic structure supposses the identical direction of magnetic moments for both components. Allowing a slightly different moment direction for each of the two magnetic moment components leads to a negligible improvement of the fit.

The value of magnetic moment for component described by propagation vector $\vec{k_1}$ is 0.8 μ_B/Ce^{3+}. The maximum value of magnetic moment for second component ($\vec{k_2}$ propagation vector) is then 1.5 μ_B/Ce^{3+}. While the first component is fully determined ($\vec{k_1} \equiv -\vec{k_1}$), the magnetic phase of second component remains ambiguous ($\vec{k_2} \in$ 1BZ). Here, we need to mention a significant limitation of neutron scattering for determination of magnetic structures. In the case of multi-$\vec{k}$ magnetic structure, it is not possible to determine the magnetic moments configuration unambiguously, unless a strong magneto-elastic coupling is present. The phase between the different Fourier components of magnetic moments cannot be determined by diffraction methods. There exist infinitely many structures able to explain the measured diffraction patterns and diffraction alone is unable to provide a unique solution. Symmetry constrains and, more importantly, restrictions on the amplitude of the magnetic moments can reduce the number of solutions. [118] The magnetic structure of $CePd_2Ga_2$ described by two commensurate propagation vectors thus cannot be determined unambiguously. The maximal value of total magnetic moment on Ce atom, which is the sum of the two components, is restricted by magnetic moment value of Ce^{3+} free ion (2.14 μ_B). Such a limitation plays an important role in a choice of the magnetic phase of the second component of magnetic moment, as the magnetic moments of first component have a constant value of 0.8 μ_B/Ce^{3+}.

We took into account such a restriction and calculated the total magnetic moment on Ce sites first for the most intuitive phase shifts. A total magnetic moment reaches the value of 2.31 μ_B/Ce^{3+} for magnetic phase shifts 0°, 90° and 180°, which is in a conflict with the maximal moment value on Ce atom. The shift of 45° leads to a smaller value of 1.87 μ_B/Ce^{3+} allowing us to define the phase interval from 30° to 60° (and equivalently from 120° to 150°), where the maximal total magnetic moment reaches the value lower than 2.14 μ_B/Ce^{3+}. On the basis of powder neutron diffraction data cannot be determined the unique solution. Nevertheless, a very tempting option seems to be the phase shift of 45°, as such an arrangement leads to only two values - 1.87 and 0.26 μ_B/Ce^{3+} - between which the total magnetic moment oscillates coming from one Ce crystallographic site to neighboring one.

Let us briefly discuss the magnetic structures and their propagation vectors in other CeT_2X_2 compounds, although the magnetic structure is known only in a handful of them, and although most of these compounds crystallize in tetragonal $ThCr_2Si_2$-type structure (space group I4/mmm, 139), see Figure 4.27. The magnetic structure in $CePd_2X_2$ with X = Si [119], Ge [120, 121] consists of magnetic moments arranged along [110] tetragonal direction and is described by propagation vector $(\frac{1}{2}, \frac{1}{2}, 0)$. The same $\vec{k}$ describes the magnetic structure in $CeRh_2Si_2$, but the magnetic moments direct along the c-axis and moreover, there is a second component of magnetic moment with $(\frac{1}{2}, \frac{1}{2}, \frac{1}{2})$ propagation vector [122]. Both components point along [001] leading to a stacking of AFM planes with total magnetic moment on Ce oscillating between the sum and difference values of these two components [122], similarly to the recent case of $CePd_2Ga_2$. The ferromagnetic planes stacked antiferromagnetically along the c-axis with magnetic moments aligned also along the c-axis are found in $CeAu_2Si_2$ [122]. $CeRu_2Ge_2$ [123] and $CeAg_2Si_2$ [122] exhibit magnetic moments parallel to the tetragonal a-axis described by $\vec{k} = (k_x \neq 0,\ 0,\ 0)$. $CeCu_2Ge_2$ with $\vec{k} = (0.28,\ 0.28,\ 0.54)$ and a spiral magnetic structure concludes our short list [115]. The magnetic structures in $CePd_2Al_2$ and $CePd_2Ga_2$ could be compared to the previous ones only after transformation from orthorhombic to tetragonal description (see Figure 4.27 for illustration), i.e. $\vec{k_1} = (\frac{1}{2}, \frac{1}{2}, 0) \rightarrow (\approx 0, \approx\frac{1}{2}, 0)^{\text{tetragonal}}$ and second propagation vector $\vec{k_2} = (0, \frac{1}{2}, 0) \rightarrow (\approx\frac{1}{4}, \approx\frac{1}{4}, 0)^{\text{tetragonal}}$, and crystallographic direction $[100]^{\text{orthorhombic}} \rightarrow \approx[110]^{\text{tetragonal}}$. By comparison of recently determined magnetic structures to other CeT_2X_2, we can conclude, that all Pd-based compounds (X = Al, Ga, Si [119] and Ge [120, 121]) reveal the magnetic structure described by $\vec{k}^{\text{tetragonal}} = (k_x \neq 0, k_y \approx k_x, 0)$ and with magnetic moments aligned along $[110]^{\text{tetragonal}}$ or very close to this direction. Nevertheless, the magnetic structure of $CePd_2Ga_2$ is described by two propagation vectors and the propagation vector of $CePd_2Al_2$ is incommensurate. The systematics in the propagation of magnetic moments in these compounds is not obvious so far. Nevertheless, the lattice parameters (i.e. the Ce-Ce interatomic distances) would play an important role in the magnetic structure formation. The c/a ratio seems to be a certain driving parameter as $c/a^{\text{tetragonal}} < 2.35$ for $CePd_2X_2$ [119, 120, 121], while $c/a^{\text{tetragonal}} > 2.35$ for other CeT_2X_2 compounds with different type of propagation and/or arrangement of magnetic moments.

4.2.4 Vibron states in $(\mathrm{Ce,La})\mathrm{Pd}_2(\mathrm{Al,Ga})_2$

Vibron state in $\mathrm{CePd}_2\mathrm{Al}_2$

To study magnetic excitations in $\mathrm{CePd}_2\mathrm{Al}_2$, inelastic neutron scattering experiments on IN6 (low-energy region) and IN4 (high energy region) spectrometers were performed. These experiments revealed three clear magnetic excitations in the energy spectrum of $\mathrm{CePd}_2\mathrm{Al}_2$ at 1.4 (3.7), 7.8 and 16 meV for tetragonal (orthorhombic) structure of $\mathrm{CePd}_2\mathrm{Al}_2$ (Figure 4.47). The magnetic origin of observed peaks is proven by comparison to $\mathrm{LaPd}_2\mathrm{Al}_2$ data and by their temperature evolution. The data presented in Figures 4.47b and 4.47d were obtained by subtracting La analogue data from $\mathrm{CePd}_2\mathrm{Al}_2$ via relation:

$$S_{\mathrm{M}}(\vec{Q},\omega) = S^{\mathrm{CePd_2Al_2}}(\vec{Q},\omega) - \alpha . S^{\mathrm{LaPd_2Al_2}}(\vec{Q},\omega), \tag{4.3}$$

where $\alpha = 0.689$ is the ratio of total-scattering cross sections for $R\mathrm{Pd}_2\mathrm{Al}_2$ with R = Ce and La, i.e. purely magnetic excitations are shown. The electronic origin of the peak at around 1.4 meV energy transfer at 20 K in Figure 4.47c is then verified by a comparison to measured 10 K spectrum in Figure 4.47a (where is no peak at low-energy region) as well as by an observation of the same excitation in the vicinity of an elastic peak on IN4 data (Figure 4.47d). A strong influence of structural phase transition from tetragonal (P4/nmm, 129) to orthorhombic (Cmma, 67) structure, see Figure 4.27 for illustration, on energy schema of $\mathrm{CePd}_2\mathrm{Al}_2$ is also demonstrated. The first CF excitation at 1.4 meV is observed in spectra measured at 20 K, where $\mathrm{CePd}_2\mathrm{Al}_2$ adopts tetragonal structure ($T_{\mathrm{struc}}^{\mathrm{CePd_2Al_2}} = 13$ K), while for $T = 10$ K spectrum the first peak appears at 3.7 meV. The other two excitations at around 7.8 and 16 meV are almost untouched by the structural transition. The measurement at 12 K (not shown), i.e. in the vicinity of $T_{\mathrm{struc}}^{\mathrm{CePd_2Al_2}}$, demonstrates the intermediate stage of first CF excitation development, as the CF peak is observed at around 3.4 meV.

The energy excitations observed directly by INS measurements are clearly reflected in the specific heat data. The magnetic part of specific heat in the paramagnetic region well above the magnetic phase transition temperature is generally described by Schottky formula (see equation 2.7) and the crystal field splitting of the multiplet ground state. According to the Kramer's theorem the ground state multiplet of the Ce^{3+} ions ($J = \frac{5}{2}$) splits into maximum three doublets (into doublet and quartet in the case of cubic CF symmetry as discussed e.g. for CeAl_2 [37, 1]) leading to the maximum two inelastic transitions from the ground state to first and second excited state. The measured magnetic contribution to specific heat is compared with the Schottky contribution calculated using the energies of CF levels as obtained by INS for compound adopting tetragonal ($T > 13$ K) and orthorhombic ($T < 13$ K) structure, see Figure 4.48a. The calculation clearly fails to describe the experimental data when only three double-degenerated levels with energies 0, 7.8 and 16 meV or 0, 1.4 (3.7) and 7.8 meV are taken into account, even considering somewhat enhanced error of the determined magnetic specific heat. The calculation with CF levels at energies 0, 1.4 and 16 meV leads to a very good agreement with the measured data, see also section 4.2.1. Far best agreement is then obtained assuming another energy level at 7.8 meV, see Figure 4.48a. The degeneracy of individual levels might be a matter of debate. A very good agreement is obtained taking double degeneracy of ground state level and

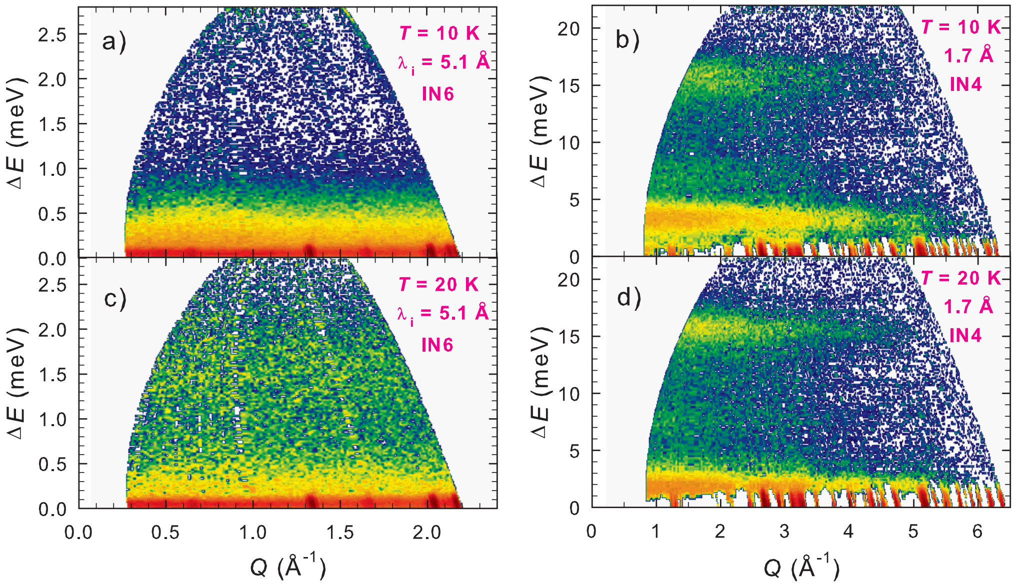

Figure 4.47: The inelastic neutron scattering data measured on $CePd_2Al_2$. Panels a) and b) contain the measurements at 10 K (i.e. in orthorhombic structure), panels c) and d) then at 20 K (i.e. in tetragonal structure). Figures in panels b) and d) represent the magnetic scattering in $CePd_2Al_2$ estimated by subtracting the data of non-magnetic $LaPd_2Al_2$. IN6 and IN4 spectrometers and incident neutrons wavelengths 5.1 and 1.7 Å were used for measurements, respectively.

level at 1.4 meV (3.7 meV), while other two levels at 7.8 and 16 meV are singlets. The total number of energy levels is 6 as expected for Ce-based compound. Taking all levels with a degeneracy of 2 leads to a strong disagreement between calculated curve and the data.

Figure 4.49 contains the low- and high-momentum transfer cuts in both analogues $CePd_2Al_2$ and $LaPd_2Al_2$. The magnetic excitations in Ce counterpart can be clearly distinguished from phonon contributions to the spectrum. The peaks of phonon origin at around 5, 9, 12 and 16.5 meV in high-$\vec{Q}$ region (Figure 4.49b) are similar for both analogues considering the differences in scattering function. Both compounds adopt the orthorhombic crystal structure at $T = 10$ K. [3, 111] The energy spectrum of $CePd_2Al_2$ adopting tetragonal structure differs negligibly at $E > 5$ meV. The low-$\vec{Q}$ cuts then demonstrate a relatively strong magnetic scattering in $CePd_2Al_2$. In summary, the comparison of low- and high-$\vec{Q}$ cuts in Figure 4.49 leads to several important observations:

- The excitations at 3.7, 7.8 and 16 meV in $CePd_2Al_2$ are all of magnetic origin, as demonstrated also by plots in Figure 4.47 and Schottky specific heat calculations in Figure 4.48.
- The phonon peaks at around 5, 9 and 16.5 meV, present in both analogues, are found at energies very close to those of CF excitations, i.e. observed peaks in low-$\vec{Q}$ spectrum of $CePd_2Al_2$ contain both magnetic and phonon contributions.
- The phonon peak at 12 meV takes place in between other two CF exciton-phonon peaks at 7.8 and 16 meV energy transfer. This phonon density of states peak was previously observed at around 11 meV by Chapon et al. [3] showing a good consistency of both studies. We note pure phonon nature of this peak, no

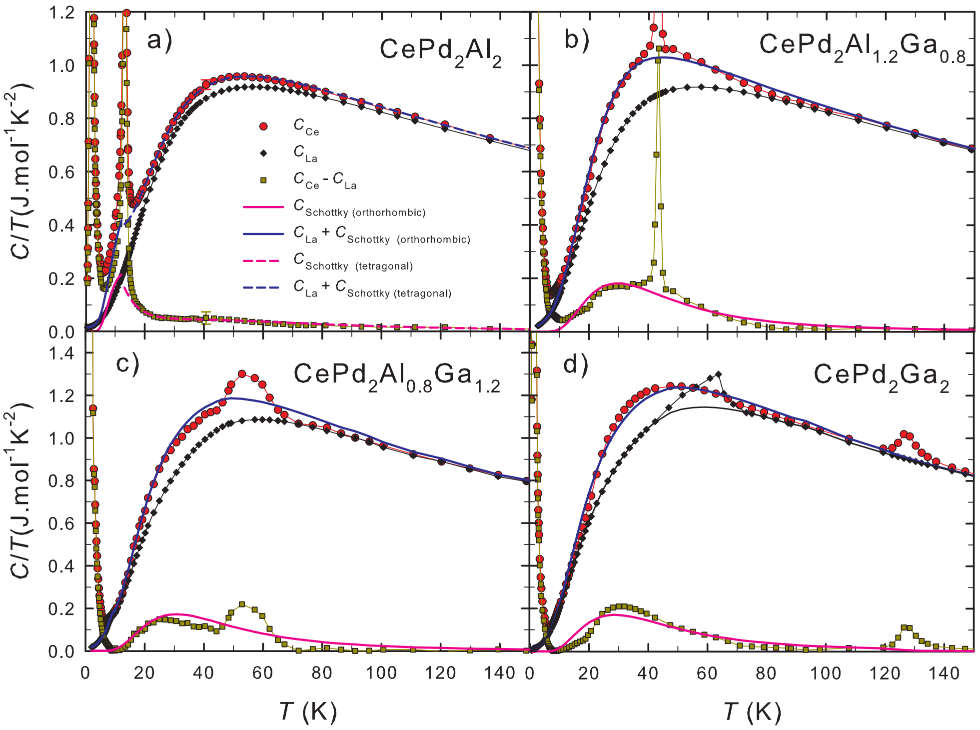

Figure 4.48: The temperature development of specific heat in CePd$_2$Al$_{2-x}$Ga$_x$, nonmagnetic analogues LaPd$_2$Al$_{2-x}$Ga$_x$, their difference and Schottky contribution to specific heat calculated from energies determined by INS experiments. Schottky contributions were calculated based on double degenerated levels with energies listed in Table 4.9; Schottky contribution for CePd$_2$Al$_2$ was calculated taking into account all three magnetic excitations and both sets of CF levels (for orthorhombic and tetragonal structure). The structural phase transitions in CePd$_2$Al$_{2-x}$Ga$_x$ and LaPd$_2$Ga$_2$ are clearly pronounced in the specific heat data. The structural phase transition from orthorhombic to tetragonal structure has great impact on energy scheme of CePd$_2$Al$_2$; the Schottky contribution for each point symmetry was calculated (full and dashed lines, respectively). The anomaly on LaPd$_2$Ga$_2$ data makes it difficult to estimate the magnetic contribution to specific heat of Ce analogue, therefore, we used a smooth (black) curve displayed in the panel d) for the subtraction of electron and phonon contributions from the total specific heat of CePd$_2$Ga$_2$. For illustration, the error bar at ≈ 40 K in panel a) corresponds to 2% error of the specific heat measurement.

magnetic contribution is present as seen from comparison of Ce and La counterparts spectra (Figure 4.49).
The inset of Figure 4.49 shows the temperature evolution of 1.4 meV peak in CePd$_2$Al$_2$ adopting tetragonal structure. The intensity decreases with increasing temperature as expected for peak related to the CF excitation. The empty CF excitation level at low-T is populated with increasing temperature leading to decrease of number of excitations due to inelastic interactions with neutrons.

The observation of an additional non-purely-phononic peak in energy spectrum of CePd$_2$Al$_2$ tends to a comparison with other Ce-based compounds revealing similar phenomenon. The energy spectrum of cubic CeAl$_2$ contains two inelastic lines in paramagnetic regime, while only single line is expected for cu-

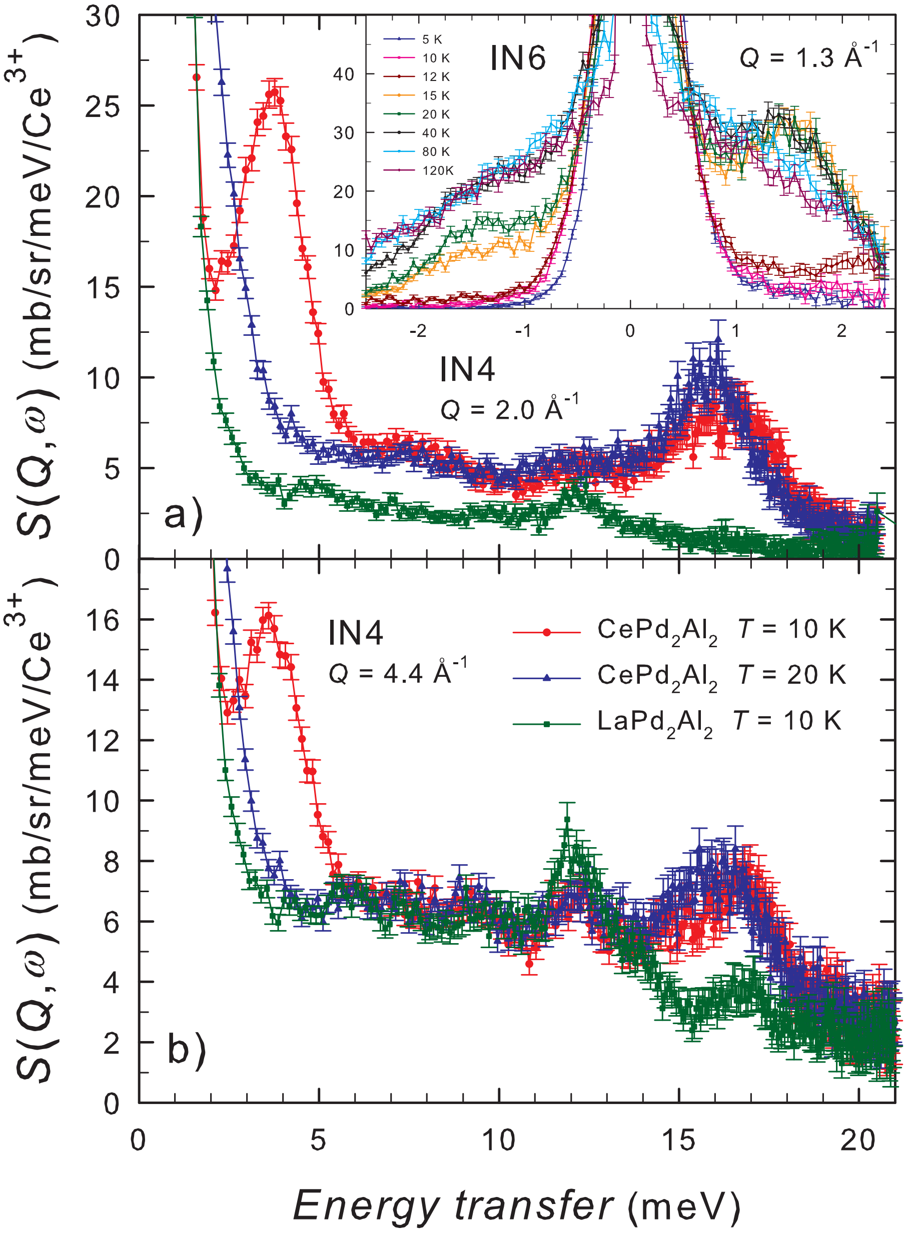

Figure 4.49: The energy transfer dependence of scattering function in $CePd_2Al_2$ and $LaPd_2Al_2$ at low (a) and high (b) momentum transfer $\vec{Q}$. The orthorhombic (10 K) and tetragonal (20 K) data for $CePd_2Al_2$ are shown; $LaPd_2Al_2$ adopts the orthorhombic structure at temperatures lower than 91.5 K. [3] The inset contains the temperature evolution of peak at 1.4 meV measured on $CePd_2Al_2$ by IN6 spectrometer.

bic symmetry of crystal field [37]. $CeCuAl_3$ crystallizing in tetragonal structure (tetragonal symmetry of crystal field) reveals three inelastic lines in energy spectrum [4], similarly to $CePd_2Al_2$. $CeCuAl_3$ and $CePd_2Al_2$ represent the only two compounds with non-cubic symmetry of crystal field revealing an additional inelastic non-purely-phononic peak in an energy spectrum, so far. The comparison of physical properties of these two compounds leads to several common characteristics:

- The tetragonal crystal structures of $CaBe_2Ge_2$-type for $CePd_2Al_2$ [3, 111, 112] and $BaNiSn_3$-type for $CeCuAl_3$ [74] belong to the maximum subgroups of tetragonal space group I4/mmm (space group 139), see Figure 4.27 for illustration. Cerium atoms occupy equivalent sites in both structures. Moreover, the volume of elementary unit cell is almost the same for both compounds (192.5 and 194.0 Å^3, respectively) [113, 74].
- A competition between a long-range RKKY interaction and Kondo screening takes place in both compounds leading to a low ordering temperature and to the exhaustion of a part of the magnetic entropy above the ordering temperature. The estimated Kondo temperature is close to 4 K in both compounds [64, 114].
- Both compounds order antiferromagnetically below 2.7 K revealing the incommensurate amplitude modulated magnetic structures, see sections 4.2.3 and 4.1.4.
- The INS spectra contain additional CF exciton-phonon peak. All three CF-like excitations reveal itself as the peaks of an intensity of similar mutual ratio in both compounds and at not significantly different energies (in $CeCuAl_3$ these excitations take place at 1.3, 9.8 and 20.5 meV [4]). A pure phonon peak in between two higher energy CF-like peaks is present in spectra of both compounds (in $CeCuAl_3$ at around 13.5 meV [4]).

The comparison of physical properties of $CePd_2Al_2$ and $CeCuAl_3$ suggests a similar mechanism behind the presence of an additional peak in energy spectra of both compounds.

Table 4.9: The parameters and eigen-values of crystal field Hamiltonian describing the CF excitations in $CePd_2Al_{2-x}Ga_x$ compounds adopting the orthorhombic structure. Only two crystal field excitations are taken into account in $CePd_2Al_2$. See text and Figure 4.50 for more details.

x	0.0	0.8	1.2	2.0
T (K)	10	10	10	10
Δ_1 (meV)	3.7(1)	8.0(2)	7.5(2)	7.2(2)
Δ_2 (meV)	16.2(2)	11.5(4)	11.5(4)	12.1(2)
B_2^0 (meV)	0.597(6)	0.350(7)	0.382(5)	0.332(5)
B_2^2 (meV)	0.491(4)	0.100(6)	0.253(4)	0.472(4)
B_4^0 (meV)	0.0133(2)	-0.0090(4)	-0.0086(4)	-0.0088(3)
B_4^2 (meV)	-0.0020(3)	0.114(1)	0.110(1)	0.111(1)
B_4^4 (meV)	0.207(3)	0.040(4)	0.060(3)	0.055(3)

The observed three crystal field-phonon excitations in $CePd_2Al_2$ cannot be described on the basis of pure CF model considering the tetragonal (orthorhombic) point symmetry of crystal field, see equations 1.7 and 1.8. The fit of measured data considering only two CF excitations at energies 1.4 and 16 meV leads to following tetragonal CF parameters: $B_2^0 = 0.99(2)$ meV, $B_4^0 = 0.016(2)$ meV and $|B_4^4| = 0.02(1)$ meV. The fit of the orthorhombic peaks at 3.7 and 16.2 meV leads to CF parameters listed in Table 4.9, the fit is shown in Figure 4.50. However, the peak at around 7.8 meV cannot be taken into account. To explain present results, we followed the procedure already used by Chapon et al. [3] and Adroja et al. [4] in the case of $CeCuAl_3$. CF exciton-phonon interaction based Thalmeier-Fulde

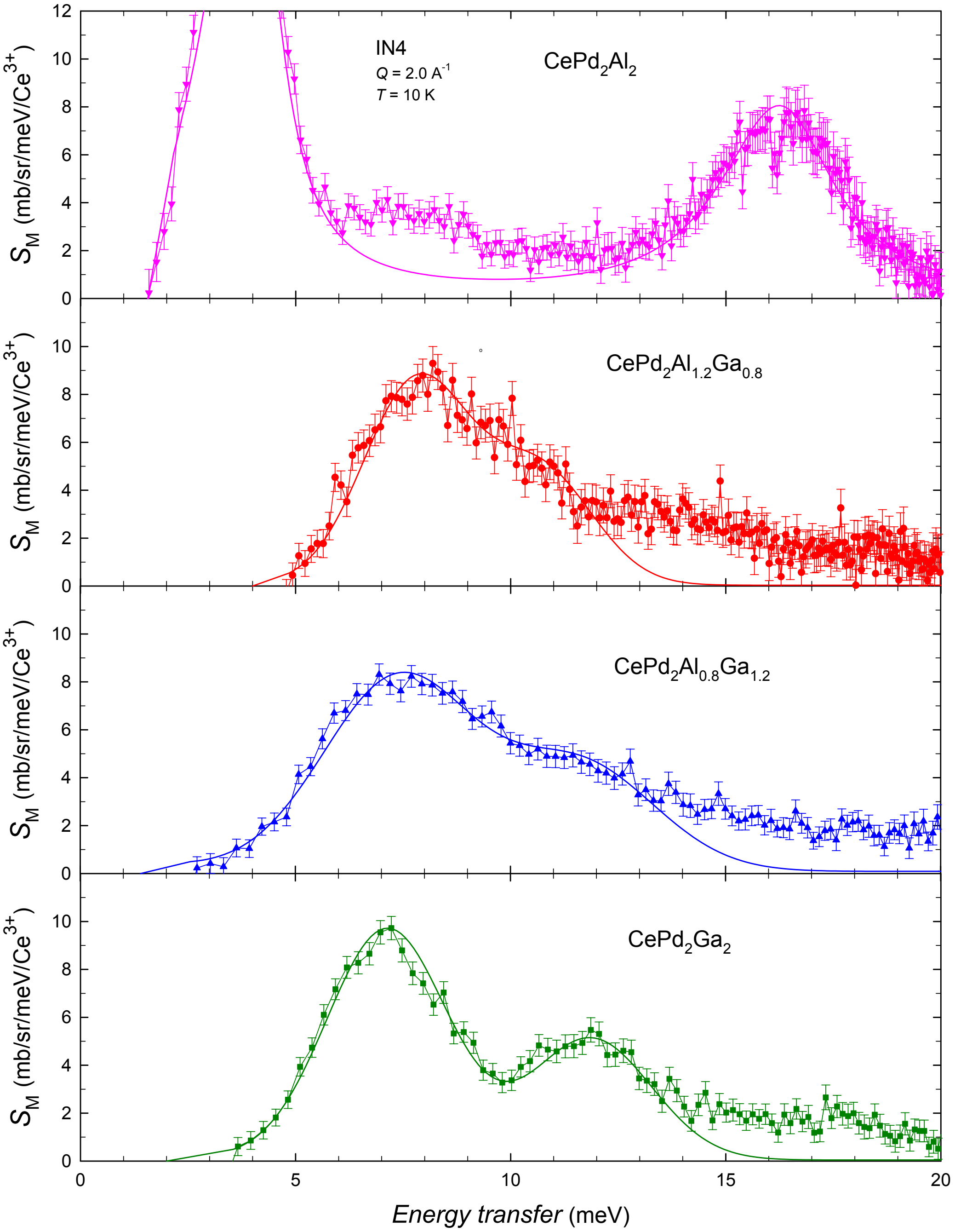

Figure 4.50: The low-$\vec{Q}$ cuts of energy spectra measured on CePd$_2$Al$_{2-x}$Ga$_x$ compounds crystallizing in orthorhombic structure. The presented magnetic parts of inelastic neutron scattering data were obtained by subtraction the LaPd$_2$(AL,Ga)$_2$ data from Ce counterpart (equation 4.3). The full lines represent the fit to equation 1.8 revealing CF parameters listed in Table 4.9. The peak at around 7.8 meV in CePd$_2$Al$_2$ is not taken into account. The scale of both x- and y-axis is the same for all compounds allowing direct observation of INS spectra development with Al-Ga substitution.

model developed for cubic CeAl$_2$ [1] and generalized for tetragonal point group symmetry (equation 3.2) was used for the fit of measured INS data.

In analogy with the data analysis of previously investigated tetragonal $\mathrm{CeCuAl_3}$ [4], we estimated the CF parameters taking into account only two CF excitations: the low-energy one at 1.4 meV and a high-energy hypothetical one close to the high phonon density of states near 12 meV. Here, we took into account the calculation of Schottky specific heat, where the best agreement between the data and calculations was obtained for levels at 7.8 and 16 meV with the single degeneracy. We fixed the CF parameters (in meV: $B_2^0 = 0.7$, $B_4^0 = 0.019$, $|B_4^4| = 0.02$) and phonon energy $\hbar\omega_0 = 12$ meV and started to vary the magneto-elastic parameter g_0 in small steps of 0.05 meV in the interval $\langle 0.05, 2.00\rangle$ meV. When $g_0 \in (0.55, 0.8)$, the peak at around 12 meV was splitted into two peaks with the second peak shifted to higher energy. The low-energy peak (1.4 meV) was shifted to higher energy only slightly. We varied in turns the phonon energy $\hbar\omega_0$ as well as the CF parameters to gradually improve the agreement between INS data and calculated curve. The final fit of the data is presented in Figure 4.51 and refined parameters are: $B_2^0 = 0.85(2)$ meV, $B_4^0 = 0.023(2)$ meV, $|B_4^4| = 0.02(1)$ meV, $\hbar\omega_0 = 9.5(5)$ meV and $g_0 = 0.35(3)$ meV. The value of $|B_4^4|$ was determined with a quite high uncertainty as the excitation energies depend on it less significantly than on other two parameters. Here, we should mention the presence of the peak at -1.4 meV in Figure 4.51b. This peak is the consequence of the principle of detailed balance and clearly documents that the excitation annihilation has lower probability than excitation creation in the material, which is mirroring in the mutual intensity of peaks at -1.4 and 1.4 meV.

The whole fitting process was done also taking the starting excitation energies 7.8 and 12 meV supposing that the hypothetical excitation at 12 meV was splitted into excitations at 1.4 and 16 meV under the influence of phonons. We note, that such a scenario is not in agreement with the specific heat analysis, where the best conformity of data and Schottky specific heat calculation was obtained for double degenerated level at 1.4 meV and singlets at 7.8 and 16 meV. Indeed, we were not able to reproduce the data in calculated spectrum: the starting CF parameters (in meV: $B_2^0 = 0.3$, $B_4^0 = 0.03$, $|B_4^4| = 0.03$) and $\hbar\omega_0 = 12$ meV were fixed, while the parameter g_0 was varied by 0.05 meV like in the previous case. Around $g_0 = 0.45$ meV, the peak at around 12 meV started to split into two peaks, whereas the lower energy peak was shifted to lower energy without any sign of splitting. Both processes the shift and splitting continued with increasing g_0 leading to relatively good description of peaks at 1.4 and 16 meV. However, the peak at 7.8 meV was not fitted at all, instead the peak at 12 meV remained almost untouched by variation of g_0. In conclusion, the fitting process proved the former scenario, which is also in agreement with specific heat analysis, i.e. the CF exciton-phonon interaction leads to the splitting of hypothetical energy level at 12 meV into two levels at around 7.8 and 16 meV.

We investigated also the energy spectrum of orthorhombic $\mathrm{CePd_2Al_2}$. The direct analysis was not possible as we used the model based on the Thalmeier-Fulde model generalized for the tetragonal symmetry of crystal field (not orthorhombic symmetry). We tried to fit the energy spectrum of orthorhombic compound with tetragonal CF parameters. First, we fitted only the peaks at 3.7 and 16 meV obtaining the values: $B_2^0 = 0.8$ meV, $B_4^0 = 0.028$ meV and $|B_4^4| = 0.03$ meV. Afterwards, we undertake the whole fitting process starting with energy levels at 3.7 and 12 meV. The refined parameters describing the measured data (see

Figure 4.51) were in meV: $B_2^0 = 0.77(2)$, $B_4^0 = 0.029(2)$, $|B_4^4| = 0.01(1)$ meV, $\hbar\omega_0 = 9.0(5)$ and $g_0 = 0.3(3)$. We are fully aware, that we fitted actually the orthorhombic structure INS data with tetragonal CF parameters, nevertheless, such a fit could serve as the first estimation of magneto-elastic parameter g_0 in the compound. The generalization of Thalmeier-Fulde model to describe also the orthorhombic symmetry of crystal field is essential for the correct treatment of the data.

Crystal field excitations in $CePd_2Ga_2$ and Al-Ga substitutions

To follow the evolution of the crystal field excitations (and a possible presence of an additional magnetic excitation) in the $CePd_2(Al,Ga)_2$ system, inelastic neutron scattering experiments on IN6 and IN4 spectrometers were performed also for several compounds with different Ga content. The measurements in paramagnetic state on IN6 instrument did not reveal any excitation in the low-energy region for any of Al-Ga substituted compounds. The measurements were done at several temperatures for both tetragonal and orthorhombic crystal structures. The inelastic spectra measured employing IN4 spectrometer at low-temperature (orthorhombic) structure exhibit two broad peaks in the energy interval 5 - 15 meV for all Al-Ga substitutions, see Figure 4.50. $CePd_2Ga_2$ reveals two clear CF peaks around 7.2 and 12.1 meV, while the Al-Ga substituted compounds exhibit at least two peaks very close in energy. The vicinity of CF peaks at around 8 and 11.5 meV in $CePd_2Al_{1.2}Ga_{0.8}$ resembles the case of $CeCu_2Ge_2$, [115] where only one quasi-quartet in excitation spectrum was speculated about [115]. Nevertheless, later study [116] showed two doublets close in energy. A possible presence of third CF-phonon excitation in both Al-Ga substituted compounds cannot be excluded on the basis of powder data, especially then in $CePd_2Al_{1.2}Ga_{0.8}$. In contrast with $CePd_2Al_2$, where the three CF-like peaks are well separated (see Figure 4.51), the vicinity of peaks in substituted compounds do not allow to properly investigate a prospective presence of an additional excitation.

Here, we should mention the differences in the inelastic neutron scattering spectra for $CePd_2(Al,Ga)_2$ compounds adopting orthorhombic and tetragonal structure. The change in energy scheme is not clearly demonstrated, except $CePd_2Al_2$, as shown above. There are two factors complicating the investigation of energy scheme in $CePd_2(Al,Ga)_2$ adopting tetragonal structure: (i) the broadness and mutual vicinity of peaks in energy spectra and (ii) the structural transition temperatures for compounds with higher Ga content are quite high [113], i.e. the low-lying energy levels are fully populated at temperatures at which the compounds adopt the tetragonal structure. A reasonable fit of tetragonal CF parameters can be done only for $CePd_2Al_{1.2}Ga_{0.8}$ leading to values: $B_2^0 = 0.240(5)$ meV, $B_4^0 = 0.030(1)$ meV and $|B_4^4| = 0.029(2)$ meV, while the excitation energies are 7.8 and 10.9 meV (not much different from energies for orthorhombic structure). The CF parameters of all compounds adopting the orthorhombic structure are listed in Table 4.9 and corresponding fits are shown as full lines in Figure 4.50. The CF parameters in $CePd_2Al_2$ differ significantly from those of Al-Ga substituted compounds; only a negligible difference is then observed within $CePd_2(Al,Ga)_2$ (see Table 4.9) as anticipated from not too much different energy spectra in Figure 4.50.

The measurement of specific heat documents the energy scheme in stud-

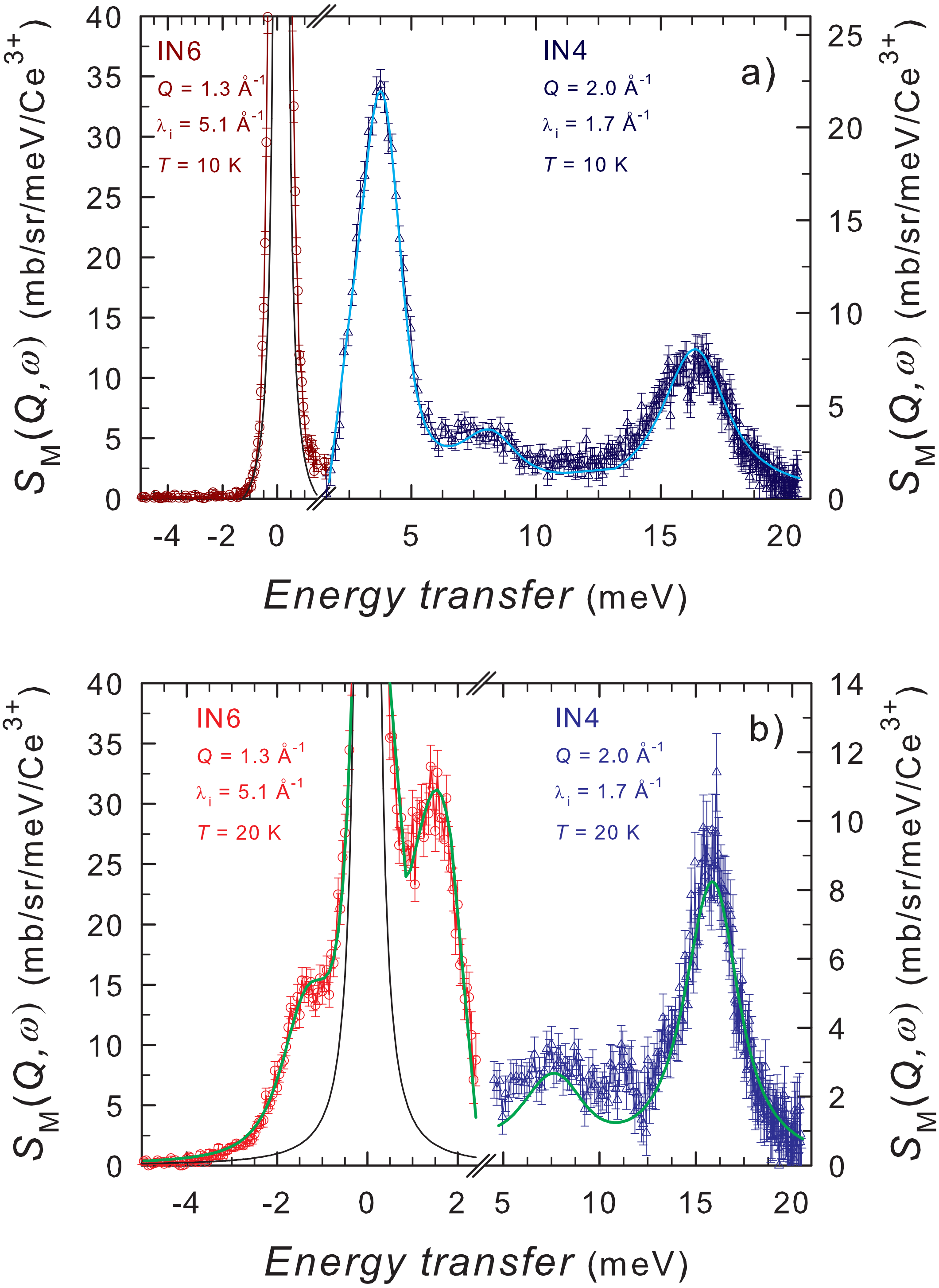

Figure 4.51: The low-$\vec{Q}$ cuts of $CePd_2Al_2$ energy spectra measured using IN6 and IN4 spectrometers. The $LaPd_2Al_2$ data were subtracted from Ce analogue IN4 data, i.e. only magnetic contributions to the spectra are presented. The energy spectra of $CePd_2Al_2$ adopting (a) orthorhombic (10 K) and (b) tetragonal (20 K) structures are presented. The full lines represent the fits to relation 3.2 as discussed in text.

ied substituted compounds as determined by INS. The magnetic specific heat is compared to Schottky contribution calculated using (orthorhombic) energies listed in Table 4.9. The agreement between the data and calculations is quite remarkable for all the compounds, see Figure 4.48. As the excitation energies in $CePd_2Al_{2-x},Ga_x$ with $x \geq 0.8$ are almost the same regardless the crystal structure, the agreement is very good also at higher temperatures. The presence of an additional energy levels in compounds with $x = 0.8$ and 1.2 cannot be excluded as a further improvement of the agreement between data and calculations can be achieved assuming certain broadening of excited levels. Nevertheless, a presence of an additional magnetic excitation at energies lower than 6 meV is clearly excluded. The structural and magnetic phase transitions reveal them selfs as anomalies in the specific heat at temperatures well corresponding to the ones determined by ours magnetization and electrical resistivity studies [113, 111].

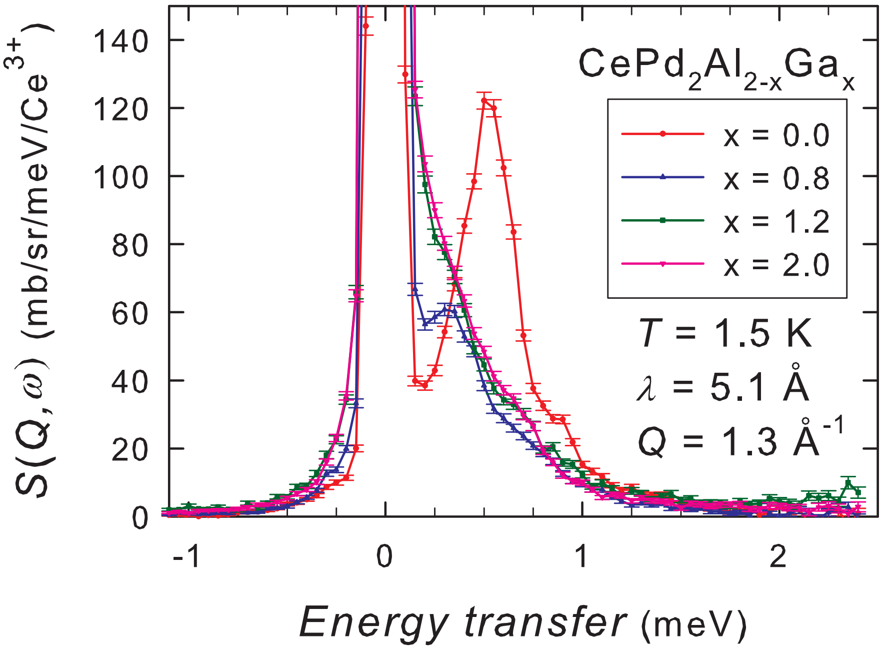

Figure 4.52: The momentum transfer cuts of low-energy part of spectra in $CePd_2Al_{2-x}Ga_x$ measured using IN6 spectrometer at temperatures $< T_N$. The shift of low-energy excitation (the splitting of doublet ground state) with the Ga content to lower energies.

The hypothesis about the influence of CF exciton-phonon interaction on crystal structure in studied compounds seems to be accurate. $CePd_2Al_2$ with transition temperature $T_{\text{struc}}^{\text{CePd}_2\text{Al}_2} << T_{\text{struc}}^{\text{LaPd}_2\text{Al}_2}$ reveals the presence of an additional magneto-phononic peak in both tetragonal and orthorhombic structures. The structural transition influences the energy scheme of the compound significantly, namely the first excitation is shifted in the energy. $CePd_2Ga_2$ on the other side of investigated series does not exhibit any sign of an additional peak in energy spectrum, while undergoing the structural transition at $T_{\text{struc}}^{\text{CePd}_2\text{Ga}_2} >> T_{\text{struc}}^{\text{LaPd}_2\text{Ga}_2}$. $CePd_2Al_{1.2}Ga_{0.8}$ and $CePd_2Al_{0.8}Ga_{1.2}$ then exhibit energy spectra revealing properties on the border between those two cases, nevertheless, resembling more pure Ga compound (which is documented also by specific heat measurement).

We also investigated the energy spectra of studied compounds below Néel temperature T_N leading to an observation of the splitting of doublet ground state as presented in Figure 4.52. The low-energy peak is clearly visible at around 0.5 meV in $CePd_2Al_2$ and around 0.3 meV in $CePd_2Al_{1.2}Ga_{0.8}$. For compounds with higher Ga content, the splitting shifts to lower excitation energies which might be related to the change of electronic properties and magnetic structure with Al-Ga substitution in $CePd_2(Al,Ga)_2$ series. Indeed, the bulk studies show rather different magnetic behavior [113] and finally our diffraction experiments revealed quite different magnetic structures in parent compounds.

Conclusions

We investigated the crystal structures and electronic properties, including magnetic structures and crystal field and magnetic excitations, in $\mathrm{CeCuAl_3}$ and $\mathrm{CePd_2Al_2}$ compounds and in substituted systems: $\mathrm{Ce(Cu,Al)_4}$, $\mathrm{Ce(Cu,Au)Al_3}$ (not part of the thesis), $\mathrm{CeCu(Al,Ga)_3}$ (not part of the thesis), $\mathrm{CePd_2(Al,Ga)_2}$ and their La analogues. The compounds were studied by means of magnetization, specific heat, electrical resistivity, electrical resistivity under hydrostatic pressure and by X-ray, electron and mainly by neutron scattering techniques.

$\mathrm{CeCuAl_3}$ was confirmed to crystallize in the ordered non-centrosymmetric $\mathrm{BaNiSn_3}$-type of tetragonal structure and undergo the isostructural phase transition at around 300°C. $\mathrm{CeCuAl_3}$ orders antiferromagnetically below $T_\mathrm{N} = 2.7(1)$ K without any further phase transition down to 0.4 K. The amplitude modulated magnetic structure in $\mathrm{CeCuAl_3}$ is described by propagation vector $\vec{k} = (0.4, 0.6, 0)$. The magnetic moments are arranged within the basal plane along the [110] crystallographic direction with a maximum value of 0.28 $\mu_\mathrm{B}/\mathrm{Ce}^{3+}$. The magnetic structure of $\mathrm{CeCuAl_3}$ was put into the context of other $\mathrm{Ce}TX_3$ compounds and the overall mechanism of the magnetic structure formation was proposed. The inelastic neutron scattering confirmed the presence of low-energy crystal field excitation at around 1.5 meV. The investigation of higher-energy part of spectrum is highly desirable and will be performed in near future.

The crystal field excitations (and possible presence of vibron states) were investigated in $\mathrm{Ce(Cu,Al)_4}$ compounds. The refined CF parameters and eigenenergies do not differ significantly among the substituted compounds revealing no magnetic excitation at low-energy part of spectra, in strong contrast with parent $\mathrm{CeCuAl_3}$. $\mathrm{CeCu_{0.9}Al_{3.1}}$ reveals the macroscopic and microscopic properties close to the ones of parent compound, while $\mathrm{CeCu_{0.75}Al_{3.25}}$ and $\mathrm{CeCu_{1.1}Al_{2.9}}$ differ significantly.

$\mathrm{CePd_2Al_2}$ crystallizes in the tetragonal $\mathrm{CaBe_2Ge_2}$-type structure and undergoes the structural phase transition to orthorhombic structure at 13 K. The antiferromagnetic ground state below $T_\mathrm{N} = 2.7$ K with the easy magnetization plane perpendicular to the c-axis was observed. The magnetic structure of $\mathrm{CePd_2Al_2}$ is described by an incommensurate propagation vector $\vec{k} = (0.06, 0.54, 0)$. The magnetic moments on Ce atoms are arranged antiferromagnetically within the basal plane and point along the direction close to the orthorhombic [100] (or equivalently close to tetragonal basal plane diagonal). The maximum value of magnetic moment reaches 2.05 $\mu_\mathrm{B}/\mathrm{Ce}^{3+}$. $\mathrm{CePd_2Al_2}$ reveals three magnetic excitations, while only the two crystal field excitations in energy spectrum are expected for cerium-based compound. The presence of additional magnetic peak is described within Thalmeier-Fulde CF exciton-phonon model generalized for non-cubic point symmetry. The additional peak is observed in both tetragonal and orthorhombic structures. The first CF excitation shifts from 1.4 meV for tetragonal structure to 3.7 meV for orthorhombic structure, while the energies of other two CF-like excitations remain almost unaffected by structural transition.

The vibron state in the rest of the $\mathrm{CePd_2(Al,Ga)_2}$ series is not observed, nevertheless, it cannot be excluded conclusively for $\mathrm{CePd_2Al_{1.2}Ga_{0.8}}$. The crystal field parameters were determined for all studied compounds as well as energies of crystal field excitations. The hypothesis about the influence of CF exciton-phonons interaction on crystal structure in studied compounds seems to be accurate. $\mathrm{CePd_2Al_2}$ with $T_{\mathrm{struc}}^{\mathrm{CePd_2Al_2}} << T_{\mathrm{struc}}^{\mathrm{LaPd_2Al_2}}$ reveals the presence of an additional magneto-phononic peak in both tetragonal and orthorhombic structures. The structural transition influences the energy scheme of the compound significantly, the first excitation is shifted in the energy. $\mathrm{CePd_2Ga_2}$ on the other side of investigated series does not exhibit any sign of an additional peak in inelastic spectrum, while undergoing the structural transition at $T_{\mathrm{struc}}^{\mathrm{CePd_2Ga_2}} >> T_{\mathrm{struc}}^{\mathrm{LaPd_2Ga_2}}$. $\mathrm{CePd_2Al_{1.2}Ga_{0.8}}$ and $\mathrm{CePd_2Al_{0.8}Ga_{1.2}}$ then exhibit properties on the border between those two cases, nevertheless, the energy spectra resemble more pure Ga compound.

$\mathrm{CePd_2Ga_2}$ reveals the magnetic structure composed from two components. First of them is described by the propagation vector $\vec{k_1} = (\frac{1}{2}, \frac{1}{2}, 0)$, while the second one propagates with $\vec{k_2} = (0, \frac{1}{2}, 0)$. The magnetic moments (of both components) are aligned along the identical direction close to the orthorhombic [100] (or equivalently to tetragonal basal plane diagonal) and the total magnetic moment varies depending on the mutual phase of moments components on each Ce site.

In conclusion, we investigated the physical properties of $\mathrm{CeCuAl_3}$ and $\mathrm{CePd_2Al_2}$ compounds in detail including their behaviour under hydrostatic and chemical pressure. We plan to continue with further studies on these compounds; a great importance will be dedicated to the inelastic neutron scattering studies on single crystals - the experiment already planned and partly done on $\mathrm{CeCuAl_3}$. Also the investigation of $\mathrm{Ce(Cu,Au)Al_3}$ and $\mathrm{CeCu(Al,Ga)_3}$ series by inelastic neutron scattering techniques is desirable and we intend to continue with it in near future. Another important part of future work will be to find more Ce-based intermetallics exhibiting a strong magneto-elastic coupling auspiciously leading to the vibron quasi-bound state and investigate them employing the inelastic neutron scattering experiments.

Bibliography

[1] Thalmeier, P., Fulde, P., *Phys. Rev. Lett.* **49**, 1588 (1982).

[2] Goremychkin, E.A., Natkaniec, I., Mhle, E., Chistyakov, O.D., *J. Magn.Magn. Mater.* **81**, 6371 (1989).

[3] Chapon, L.C., Goremychkin, E.A., Osborn, R., Rainford, B.D., Short, S., *Physica B* **378380**, 819 (2006).

[4] Adroja, D.T., Moral, A. del, Fuente, C. de la, Fraile, A., Goremychkin, E.A., Taylor, J.W., Hillier, A.D., Fernandez-Alonso, F., *Phys. Rev. Lett.* **108**, 216402 (2012).

[5] Chatterji, T., Neutron Scattering from Magnetic Materials, *Elsevier* ISNB: 978-0-444-51050-1 (2005).

[6] Kondo, J., *Prog. Theor. Phys.* **32**, 37-49 (1964).

[7] Anderson, P.W., *Phys. Rev.* **124**, 41-53 (1961).

[8] Doniach, S., *Physica B* **91**, 231-234 (1977).

[9] Garratt-Reed, A.J., Bell, D.C., Energy-dispersive x-ray analysis in the electron microscope, Microscopy Handbooks (M. Rainforth, ed.), Oxford, UK (2003).

[10] Agarwal, B.K., X-ray Spectroscopy, Springer-verlag, Berlin (1991).

[11] Rodriguez-Carvajal, J., *Physica B* **192**, 55 (1993).

[12] Ouladdiaf, B., Archer, J., Allibon, J.R., Decarpentrie, P., Lemée-Cailleau, M.H., Rodriguez-Carvajal, J., Hewat, A.W., A.W. Hewat, York, S., Brau, D., McIntyre, G.J., *J. Appl. Crystall.* **44**, 392-397 (2011).

[13] Tumanski, S., Handbook of Magnetic Measurements, Danver, US (2011), ISBN: 978-1-4398-2951-6.

[14] Schwartz, B.B., Foner, S., Superconductor Applications: SQUIDs and Machines, New York, US (1977).

[15] Solivérez, C.E., *IEEE Transactions on Magnetics* **17**, 1363–4 (1981).

[16] Martin, C.A., *J. Phys.: Condens. Matter* **3**, 5967 (1991).

[17] Hwang, J.S., Lin, K.J., Tien, C., *Rev. Sci. Instrum.* **68**, 94-101 (1997).

[18] Elliot, R.J., Wedgwood, F.A., *Proc. Phys. Soc.* **81**, 864 (1963).

[19] Noziéres, P., *J. Low Temp. Phys.* **12**, 31-42 (1974).

[20] Fujiwara, N., Matsumoto, T., Koyama-Nakazawa, K., Hisada, A., Uwatoko, Y., *Rev. Scient. Instrum.* **78**, 073905 (2007).

[21] Yokogawa, K., Murata, K., Yoshino, H., Aoyama, S., *Jpn. J. App. Phys.* **46**, No. 6A, 3636-3639 (2007).

[22] Waseda, Y., Matsubara, E., Shinoda, K., X-Ray Diffraction Crystallography: Introduction, Examples and Solved Problems ISBN 9783642166358, (2011).

[23] Squires, G.L., Introduction to the Theory of Thermal Neutron Scattering, Dover Publications, inc., Mineola, New York, (1978).

[24] Shirane, G., Shapiro, S.M., Tranquada, J.M., Neutron Scattering with a Triple-Axis Spectrometer, Dover Publications, inc., Cambridge University Press, UK, ISBN 0-511-03732-5, (2002).

[25] McIntyre, G.J., Stansfield, R.F.D., *Acta Cryst.* **44**, 257-262 (1988).

[26] Zachariasen, W.H., *Acta Cryst.* **16**, 1139-1144 (1963).

[27] Marshall, W., Lowde, R.D., *Rept. Progr. Phys.* **31**, 705 (1968).

[28] Lovesey, S.W., *Theory of Neutron Scattering from Condensed Matter*, Clarendon Press, Oxford, (1984).

[29] Steglich, F., Bredl, C.D., Loewenhaupt, M., Schotte, K.D., *J. Physique, Colloque C5* **40**, 301 (1979).

[30] Loewenhaupt, M., Witte, U., *J. Phys.: Condens. Matter* **15**, S519-S536 (2003).

[31] Murani, A.P., Eccleston, R.S., *Physica B* **234-236**, 888-890 (1997).

[32] Park, J.-G., Murani, A.P., *J. Phys.: Condens. Matter* **15**, 6835-6844 (2003).

[33] Reichardt, W., Nücker, N., *J. Phys. F: Met. Phys.* **14**, L135-L140 (1984).

[34] Barbara, B., Boucherle, J.X., Buevoz, J.L., Rossignol, M.F., Schweizer, J., *J. Physique, Colloque C5* **40**, 321 (1979).

[35] Schweizer, J., Givord, F., Boucherle, J.X., Bourdarot, F., Ressouche, E., *J. Phys.: Condens. Matter* **20**, 135204 (2008).

[36] Thalmeier, P., *J. Phys. C: Solid State Phys.* **17**, 4153-4177 (1984).

[37] Loewenhaupt, M., Rainford, F., Steglich, F., *Phys. Rev. Lett.* **25**, 1709 (1979).

[38] Lipiński, S., *J. Magn. Magn. Matter.* **192**, 553-563 (1999).

[39] Hillier, A.D., Adroja, D.T., Manuel, P., Anand, V.K., Taylor, J.W., McEwen, K.A., Rainford, B.D., Koza, M.M., *Phys. Rev. B* **85**, 134405 (2012).

[40] Pashen, S., Felder, E., Ott, H.R., *Eur. Phys. J. B* **2**, 169 (1998).

[41] Smidman, M., Adroja, D.T., Hillier, A.D., Chapon, L.C., Taylor, J.W., Anand, V.K., Singh, R.P., Lees, M.R., Goremychkin, E.A., Koza, M.M., Krishnamurthy, V.V., Paul, D.M., Balakrishnan, G., *Phys. Rev. B* **88**, 134416 (2013).

[42] Muranaka, T., Akimitsu, J., *Physica C* **460–462**, 688–690 (2007).

[43] Joshi, D.A., Burger, P., Adelmann, P., Ernst, D., Wolf, T., Sparta, K., Roth, G., Grube, K., Meingast, C., Löhneysen, H.v., *Phys. Rev. B* **86**, 035144 (2012).

[44] Haen, P., Lejay, P., Chevalier, B., Lloret, B., Etourneau, J., Sera, M., *J. Less-Common Met.* **110**, 321 (1985).

[45] Mock, S., Pfleiderer, C., Lohneysen, H.v., *J. Low Temp. Phys.* **115**, 1 (1999).

[46] Martin, J.M., Paul, D.M., Lees, M.R., Werner, D., Bauer, E., *J. Magn. Magn. Mater.* **159**, 223-226 (1996).

[47] Martin, J.M., Lees, M.R., Paul, D.M., Dai, P., Ritter, C., Bi, Y.J., *Phys. Rev. B* **57**, 7419 (1998).

[48] Nimura, N., Ito, K., Saitoh, K., Umeda, Y., Aoki, H., Terashima, T., *Phys. Rev. B* **95**, 247004 (2005).

[49] Sugitani, I., Okuda, Y., Shishido, H., Yamada, T., Thamhavel, A., Yamamoto, E., Matsuda, T.D., Haga, Y., Takeuchi, T., Settai, R., Ōnuki, Y., *J. Phys. Soc. Japan* **75**, 043703 (2006).

[50] Bauer, E., Pillmayr, N., Gratz, E., Hilscher, G., Gignoux, D., Schmitt, D., *Z. Phys. B* **67**, 205 (1987).

[51] Kontani, M., Ido, H., Ando, H., Nishioka, T., Yamaguchi, Y., *J. Phys. Soc. Japan* **63**, 1652 (1994).

[52] Nishioka, T., Kawamura, Y., Kato, H., Matsumura, M., Kodama, K., Sato, N.K., *J. Magn. Magn. Mater.* **310**, e12-e14 (2007).

[53] Mentink, S.A.M., Bos, N.M., Rossum, F.J. van, Nieuwenhuys, G.J., Mydosh, J.A., Buschow, K.H.J., *J. Appl. Phys.* **73**, 6625 (1993).

[54] Kontani, M., Motoyama, G., Nishioka, T., Murase, K., *Physica B* **259-261**, 24 (1999).

[55] Oohara, Y., Motoyama, G., Nishioka, T., Kontani, M., *Technical Report of ISSP, Ser. A*, 3526 (1999).

[56] Zarechnyuk, O.S., Kripyakevic, P.L., Gladyshevskii, E.L., *Sov. Phys. Crystallogr.* **9**, 706 (1965).

[57] Moze, O., Buschow, K.H.J., *J. Alloys Comp.* **245**, 112 (1996).

[58] Hu, X.D., Zhou, H.Y., Li, J.B., Pan, S.K., Wang, T., Yao, Q.R., Duan, L.B., Wang, Y.C., Chen, X.J., Rao, G.H., *Intermetallics* **17**, 775 (2009).

[59] Adroja, D.T., *private communication.*

[60] Klicpera, M., Javorský, P., *J. Magn. Magn. Mater.* **363**, 88-94 (2014).

[61] Klicpera, M., Javorský, P., *J. Alloys Comp.* **621**, 78-85 (2015).

[62] Doležal, P., *Master thesis*, Charles university in Prague, Faculty of Mathamtics and Physics (2015), in czech language.

[63] Doležal, P., Klicpera, M., Prchal, J., Javorský, P., *Phys. Polonica A* **127**, 219-221 (2015).

[64] Klicpera, M., Doležal, P., Prokleška, J., Prchal, J., Javorský, P., *J. Alloys Comp.* **639**, 51-59 (2015).

[65] Klicpera, M., Javorský, P., Pasztorová, J., *Supercond. Scien. Technol.* **27**, 085001 (2014).

[66] Eisenmann, B., Schäfer, J., *J. Less-Common Metals* **123**, 89-94 (1986).

[67] Anand, V.K., Adroja, D.T., Hillier, A.D., Kockelmann, W., Fraile, A., Strydom, A.M., *J. Phys.: Cond. Matter* **23**, 276001 (2011).

[68] Seropegin, Yu.D., Shapiev, B.I., Gribanov, A.V., Bodak, O.I., *J. Alloys Comp.* **288**, 155-158 (1999).

[69] Pikul, A.P., Kaczorowski, D., Plackowski, T., Czopnik, A., Michor, H., Bauer, E., Hilscher, G., Rogl, P., Grin, Yu., *Phys. Rev. B* **67**, 224417 (2003).

[70] Franz, Ch., *Ph.D. thesis*, Untersuchung von Quantenphasenübergängen bei fehlender Inversionssymmetrie, Technische Universität München, (2014).

[71] Kim, J.W., Kwon, Y.S., *Physica B* **378–380**, 833–834 (2006).

[72] Grin, Yu.N., Rogl, P., Hiebl, K., *J. Less-Common Metals* **136**, 329-338 (1988).

[73] Hulliger, F., *J. Alloys Comp.* **218**, 255-258 (1995).

[74] Klicpera, M., Javorský, P., Čermák, P., Rudajevová, A., Daniš, S., Brunátová, T., Císařová, I., *Intermeral.* **46**, 126-130 (2014).

[75] Yamamoto, H., Sawa, H., Ishikawa, M., *Phys. Lett. A* **196**, 83-86 (1994).

[76] Seropegin, Yu.D., Shapiev, B.I., Gribanov, A.V., Bodak, O.I., *J. Alloys Comp.* **288**, 147-150 (1999).

[77] Hong, J.B., Kim, J.W., Lee, K.E., Lee, N.A., Jang, K.H., Park, J.-G., Kwon, Y.S., *J. Magn. Magn. Mater.* **310**, 292–294 (2007).

[78] Aso, N., Miyano, H., Yoshizawa, H., Kimura, N., Komatsubara, T., Aoki, H., *J. Magn. Magn. Mater.* **310**, 602-604 (2007).

[79] Aso, N., Takahashi, M., Yoshizawa, H., Iida, H., Kimura, N., Aoki, H., *J. Phys.: Conf. Series* **400**, 022003 (2012).

[80] Kawai, T., Muranaka, H., Measson, M.-A., Shimoda, T., Doi, Y., Matsuda, T.D., Haga, Y., Knebel, G., Lapertot, G., Aoki, D., Flouquet, J., Takeuchi, T., Settai, R., Onuki, Y., *J. Phys. Soc. Japan* **77**, 064716 (2008).

[81] Cava, R.J., Ramirez, A.P., Takagi, H., Krajewski, J.J., Peck, W.F. Jr., *J. Magn. Magn. Mater.* **128**, 124-128 (1993).

[82] Seropegin, Yu.D., Gribanov, A.V., Kubarev, O.L., Tursina, A.I., Bodak, O.I., *J. Alloys Comp.* **317-318**, 320-323 (2001).

[83] Kawai, T., Okuda, Y., Shishido, H., Thamizhavel, A., Matsuda, T.D., Haga, Y., Nakashima, M., Takeuchi, T., Hedo, M., Uwatoko, Y., Settai, R., Onuki, Y., *J. Phys. Soc. Japan* **76**, 014710 (2007).

[84] Adroja, D.T., Fuente, C. de la, Fraile, A., Hillier, A.D., Daoud-Aladine, A., Kockelmann, W., Taylor, J.W., Murani, A.P., Koza, M.M., Burzurí, E., Luis, F., Arnaudas, J.I., Moral, A. del, http://arxiv.org/, arXiv: 1501.00286.

[85] Rojas, D.P., Rodríguez Fernandez, J., Espeso, J.I., Gómez Sal, J.C., *J. Alloys Comp.* **502**, 275-278 (2010).

[86] Werner, D., Bauer, E., Martin, J.M., Lees, M.R., *Physica B* **259-261**, 10-11 (1999).

[87] Schlottmann, P., *Z. Phys. B - Condens. Matt.* **51**, 223-235 (1983).

[88] Pietri, R., Andraka, B., Kaczorowski, D., Leithe-Jasper, A., Rogl, P., *Phys. Rev. B* **61**, 12169 (2000).

[89] Ouladdiaf, B., Archer, J., Allibon, J.R., Decarpentrie, P., Lemée-Cailleau, M.H., Rodriguez-Carvajal, J., Hewat, A.W., York, S., Brau, D., McIntyre, J., *Appl. Crystall.* **44**, 392-397 (2011).

[90] Rodriguez-Carvajal, J., Fuentes-Montero, L., Čermák, P., *to be published.* See the web page http://lauesuite.com/

[91] Brush, G.S., *Rev. Mod. Phys.* **39**, 883 (1967).

[92] Matsumura, M., Kawamura, Y., Yoshina, M., Nishioka, T., Kato, H., *J. Phys.: Confer. Series* **150**, 042122 (2009).

[93] Vonlanthen, P., Gavilano, J.L., Ambrosini, B., Ott, H.R., *Eur. Phys. J. B* **7**, 9-17 (1999).

[94] Knafo, W., Raymond, S., *J. Phys.: Cond. Matter***15**, 3741-3749 (2003).

[95] Oe, K., Kobayashi, R., Nishioka, T., Kato, H., Matsumura, M., Kodama, K., *J. Phys. Conf. Ser.* **150**, 042146 (2009).

[96] Čermák, P., Uhlířová, K., Javorský, P., *Physica B: Conden. Matt.* **405**, 2294 (2010).

[97] Yao, Q.R., Hu, X.D., Chen, X.J., Pan, S.K., Zou, W., Wang, H.L., Wang, Y.C., Wang, P.P., Liu, F., Wang, Z.M., Zhou, H.Y., Tang, C.Y., *J. Alloys Comp.* **484**, 86 (2009).

[98] Andersen, N.H., Smith, H., *Phys. Rev. B* **19**, 384 (1979).

[99] Blanco, J.A., Podesta, M. de, Espeso, J.I., Gómez Sal, J.C., Lester, C., McEwan, K.A., Patrikios, N., Rodriguez Fernandez, J., *Phys. Rev. B* **49**, 15126 (1994).

[100] Fernandez-Baca, J.A., Hill, P., Chakoumalos, B.C., Ali, N., *J. Appl. Phys.* **79**, 5398 (1996).

[101] Lalić, M.V., Mestnik-Filho, J., Carbonari, A.W., Saxena, R.N., *J. Magn. Magn. Mater.* **272-276**, 633-634 (2004).

[102] Toliński, T., Synoradzki, K., Koterlyn, M., Koterlyn, G., Yasnitskii, R., *J. Alloys Comp.* **580**, 512-516 (2013).

[103] Steglich, F., Aarts, J., Bredl, C.D., Lieke, W., Meshede, D., Franz, W., Schäfer, H., *Phys. Rev. Lett.* **43**, 1892 (1979).

[104] Groshe, F.M., Julian, S.R., Mather, N.D., Lonzarich, G.G., *Physica B* **223-224**, 50 (1996).

[105] Yamaoka, H., Zekko, Y., Kotani, A., Jarrige, I., Tsujii, N., Lin, J., Mizuki, J., Abe, H., Kitazawa, H., Ishii, H., Tsuei, K., *Phys. Rev. B* **86**, 235131 (2012).

[106] Movshovich, R., Graf, T., Mandrus, D., Hundley, M.F., Thompson, J.D., Fisher, R.A., Smith, J.L., *Physica B* **223-224**, 126 (1996).

[107] Jaccard, D., Behnia, K., Sierro, J., *Phys. Lett. A* **163**, 475 (1992).

[108] Beyermann, W.P., Hundley, M.F., Canfield, P.C.,Godart, C., Selsane, M., Fisk, Z., Smith, J.L., Thompson, J.D., *Physica B* **171**, 373 (1991).

[109] Kitagawa, J., Ishikawa, M., *J. Phys. Soc. Japan* **68**, 2380-2383 (1999).

[110] Takabatake, T., Tanaka, T., Bando, Y.,Fujii, H., Takeda, N., Ishikawa, M., Oguro, I., *Physica B* **230-232**, 223-225 (1997).

[111] Doležal, P., Klicpera, M., et al. *will be published.*

[112] Tursina, A., Khamitcaeva, E., Gribanov, A., Gnida, D., Kaczorowski, D., *Inorg. Chem.*, DOI: 10.1021/ic503110c

[113] Klicpera, M., Javorský, P., Hoser, A., *J. Alloys Comp.* **596**, 167-172 (2014).

[114] Javorský, P., Klicpera, M., *J. Magn. Magn. Mater.* **342**, 152-155 (2013).

[115] Knopp, G., Loidl, A., Knorr, K., Pawlak, L., Duczmal, M., Caspary, R., Gottwick, U., Spille, H., Steglich, F., Murani, A.P., *Z. Phys. B - Conden. Matter* **77**, 95-104 (1989).

[116] Loewenhaupt, M., Faulhaber, E., Schneidewind, A., Deppe, M., Hradil, K., *J. Applied Phys.* **111**, 07E124 (2012).

[117] Perez-Mato, J.M., Gallego, S.V., Tasci, E.S., Elcoro, L., Flor, G. de la, Aroyo, M.I., *Annu. Rev. Mater. Res.* **45**, 13.1-13.32 (2015).

[118] Rodríguez-Carvajal, J., Bourée, F., *EPJ Web of Conferences* **22**, 00010-p.24 (2012), DOI: 10.1051/epjconf/20122200010

[119] Steeman, R.A., Frikkee, E., Helmholdt, R.B., Menovsky, A.A., Berg, J. van den, Nieuwenhuys, G.J., Mydosh, J.A., *Solid State Comm.* **66**, 103-107 (1988).

[120] Feyerherm, R., Becker, B., Collins, M.F., Mydosh, J., Nieuwenhuys, G.J., Ramakrishnan, S., *Physica B* **241-243**, 643-645 (1998).

[121] Fåk, B., Ressouche, E., Knebel, G., Flouquet, J., Lejay, P., *Solid State Comm.* **115**, 407-410 (2000).

[122] Grier, B.H., Lawrence, J.M., Murgai, V., Parks, R.D., *Phys. Rev. B* **29**, 2664 (1984).

[123] Raymond, S., Haen, P., Calemczuk, R., Kambe, S., Fåk, B., Lejay, P., Fukuhara, T., Flouquet, J., *J. Phys.: Condens. Matter* **11**, 5547-5560 (1999).

List of Tables

List of Abbreviations

a	lattice parameter of tetragonal structure (if not stated otherwise)
A	absorption
Å	Angstroem
ac-	alternate current (susceptiblity)
AFM	antiferromagnetic state of material
b_j	scattering length
B_m^n	crystal electric field parameter
BSE	back-scattered electrons
c	lattice parameter of tetragonal structure (if not stated otherwise)
C_{el}	electronic contribution to the specific heat
C_{mag}	magnetic contribution to the specific heat
C_{p}	total specific heat
C_{ph}	phonon contribution to the specific heat
C_{Schottky}	Schottky contribution to the specific heat
CEF (CF)	crystalline electric field (crystal field)
CYCLOPS	CYlindrical Ccd Laue Octagonal Photo Scintillator
DSC	differential scanning calorimetry
DTA	differential thermal analysis
E	energy
E_x	extinction
EDX	Energy Dispersive X-ray (diffraction)
$f_j(\vec{Q})$	magnetic formfactor
F	structure factor
F_{N}	nuclear structure factor
F_{M}	magnetic structure factor
FC	field cooled (regime of magnetization measurement)
g_{J}	Landé g-factor
$\vec{G}$	reciprocal space vector
$\hbar$	reduced Planck constant ($= \frac{h}{2\pi} = 6.58211928(15)\ .10^{-16}$ eV.s)
H	magnetic field
$\widehat{H}$	Hamiltonian
$\widehat{H}_{\mathrm{CEF}}$	Hamiltonian of crystal electric field
HZB	Helmholz Zentrum Berlin, Germany
I	intensity (of radiation)
ILL	Institute Laue-Langevin, Grenoble, France

INS	inelastic neutron scattering
ISIS	pulsed neutron and muon source at the Rutherford Appleton Laboratory, Oxfordshire, Great Britain
j, j_{el}	electrical current
J	total angular momentum
J_{ex}	exchange constant (of RKKY and Kondo interaction)
$\vec{k}$	propagation vector of magnetic structure
$\vec{k}_1$, $\vec{k}_2$	wave vectors of incident and scattered neutron, respectively
k_{B}	Boltzmann constant (= 8.6173324(78) .10^{-5} eV.K^{-1})
K	Kelvin (unit of temperature and energy)
L	orbital momentum
L_{f}	Lorentz factor
m	neutron mass (= 1.674927351(74) .10^{-27} kg)
M	magnetization
meV	milielectronvolt (energy unit; 1 eV = 1.602176565(35) .10^{-19} J)
MLTL	Magnetism and Low Temperatures Laboratories, Prague, Czech Republic (http://mltl.eu/)
MPMS	Magnetic Property Measurement System (Quantum Design)
MR	magneto-resistance, magnetoresistance
$n(E_{\mathrm{F}})$	density of states at Fermi level
N_{A}	Avogadro constant (= 6.02214129(27) .10^{23} mol^{-1})
nFL	non-Fermi-liquid
$\widehat{O}_m^n$	Steven's operator
P	preferential orientation
PPMS	Physical Property Measurement System (Quantum Design)
q	latent heat
$\vec{q}$	relative momentum ($\vec{Q} = \vec{G} + \vec{q}$)
$\vec{Q}$	scattering vector (vector from reciprocal space)
R	gas constant (= 8.3144621(75) J.K^{-1}.mol^{-1})
$R(T), R(H)$	electrical resistivity (measured in dependence on temperature/magnetic field)
R_0	residual electrical resistivity
R_{el}	electron-electron part of electrical resistivity
$\vec{R}_j$	lattice vector (vector from real space), position of j^{th} atom
R_{ph}	electron-phonon part of electrical resistivity
RKKY	Ruderman-Kittel-Kasuya-Yosida indirect interaction

S	spin momentum
S_{mag}	magnetic entropy
$S_{\mathrm{mag_{ord}}}$, $S_{T_{\mathrm{N}}}$	magnetic entropy at ordering (Néel) temperature
SC	superconductivity, superconducting state
T_{C}	Curie temperature
T_{K}	strength of Kondo interaction, Kondo temperature
T_{N}	Néel temperature
T_{RKKY}	strength of RKKY interaction
T_{SC}	temperature of superconducting state transition
$v^{(1)}$, $v^{(2)}$	molar volume before and after transition, respectively
v_{F}	Fermi velocity
V	volume of elementary unit cell
W_j	temperature factor (exponent in Debye-Waller factor)
$z_{\ldots}$	fraction atomic coordinate of tetragonal structure (along tetragonal c-axis)
ZFC	zero field cooled (regime of magnetization measurement)
α	ratio of total-scattering cross sections of Ce- and La-based compounds analogues
β	specific heat coefficient related to energy of acoustic phonons
γ_{el}	Sommerfeld coefficient of electronic contribution to specific heat
Δ_1, Δ_2	excitation energies in compound due to the influence of crystal field
ΔC_{el}	size of the specific heat jump at superconducting transition
λ	wavelength of radiation
μ_0	magnetic permeability of vacuum ($= 4\pi\ .10^{-7}\ \frac{\mathrm{W}}{\mathrm{A.m}}$)
μ_{B}	Bohr magneton ($= \frac{e\hbar}{2m} = 5.7883818066(38)\ .10^{-5}\ \mathrm{eV.T^{-1}}$)
μ_{eff}	effective magnetic moment
μ_j	magnetic moment on j^{th} atom
$\mu_{j\perp}$	perpendicular component of magnetic moment (component of magnetic moment perpendicular to the scattering vector $\vec{Q}$)
μ_{ord}	ordered magnetic moment
θ_{D}	Debye temperature
$\theta_{\mathrm{D}}^{\mathrm{R}}$	Debye temperature determined from electrical resistivity
θ_{E}	Einstein temperature

The results presented in this thesis have been published in peer reviewed journals cited below:

Neutron scattering study of magnetic order in $\mathrm{CeCuAl_3}$ single crystal
Klicpera, M., Javorský, P., Čermák, P., Schneidewind, A., Ouladdiaf, B., Diviš, M.
Phys. Rev. B **91**, 224419 (2015)
DOI: 10.1103/PhysRevB.91.224419

Structural phase transition in $\mathrm{CePd_2Ga_2}$ under hydrostatic pressure
Doležal, P., Klicpera, M., Prchal, J., Javorský, P.
Acta Phys. Pol. A **127**, 219-221 (2015)
DOI: 10.12693/APhysPolA.127.219

Magnetic and transport properties of $\mathrm{CePd_2Al_2}$ single crystal
Klicpera, M., Doležal, P., Prokleška, J., Prchal, J., Javorský, P.
J. Alloys Comp. **639**, 51-59 (2015)
DOI: 10.1016/j.jallcom.2015.03.095

Magnetization and electrical resistivity measurements on $\mathrm{CeCuAl_3}$ single crystal
Klicpera, M., Javorský, P., Diviš, M.
J. Phys.: Conf. Ser. **592**, 012014 (2015)
DOI: 10.1088/1742-6596/592/1/012014

Development of crystal structure and magnetism in $R\mathrm{CuAl}_{3-x}\mathrm{Ga}_x$ solid solutions
Klicpera, M., Javorský, P.
J. Alloys Comp. **621**, 78-85 (2015)
DOI: 10.1016/j.jallcom.2014.09.188

Specific heat study in $(\mathrm{Ce,La})\mathrm{Pd}_2X_2$ compounds (X = Al, Ga)
Klicpera, M., Pastzorová, J., Javorský, P.
J. Supercond. Nov. Magn. **28**, 859-862 (2015)
DOI: 10.1007/s10948-014-2692-z

Superconductivity in $\mathrm{LaPd_2Al}_{2-x}\mathrm{Ga}_x$ compounds
Klicpera, M., Javorský, P., Pastzorová, J.
Supercond. Scien. Techno. **27**, 085001 (2014).
DOI: 10.1088/0953-2048/27/8/085001

Structural phase transition in $\mathrm{CeCuAl_3}$ single crystal
Klicpera, M., Javor-ský, P., Daniš, S., Brunátová, T.
Acta Phys. Pol. A **126**, 290 (2014)
DOI: 10.12693/APhysPolA.126.290

Study of electronic properties in $R\mathrm{Cu}_{1-x}\mathrm{Au}_x\mathrm{Al}_3$ compounds, where R = Ce, La
Klicpera, M., Javorský, P.
J. Magn. Magn. Mater. **363**, 88-94 (2014)
DOI: 10.1016/j.jmmm.2014.03.071

Structural and electronic properties of $R\mathrm{Pd}_2\mathrm{Al}_{2-x}\mathrm{Ga}_x$ (R = Ce and La) compounds
Klicpera, M., Javorský, P., Hoser, A.
J. Alloys Comp. **596**, 167-172 (2014)
DOI: 10.1016/j.jallcom.2014.01.039

Crystal structure and its stability in CeCuAl_3 single crystal
Klicpera, M., Javorský, P., Čermák, P., Rudajevová, A., Daniš, S., Brunátová, T., Císařová, I.
Intermetall. **46**, 126-130 (2014)
DOI: 10.1016/j.intermet.2013.11.004

Specific-heat study of $\mathrm{Ce(Cu,Al)}_4$ compounds
Javorský, P., Klicpera, M.
J. Magn. Magn. Mater. **342**, 152-155 (2013)
DOI: 10.1016/j.jmmm.2013.04.043